CHALMERS
UNIVERSITY OF TECHNOLOGY

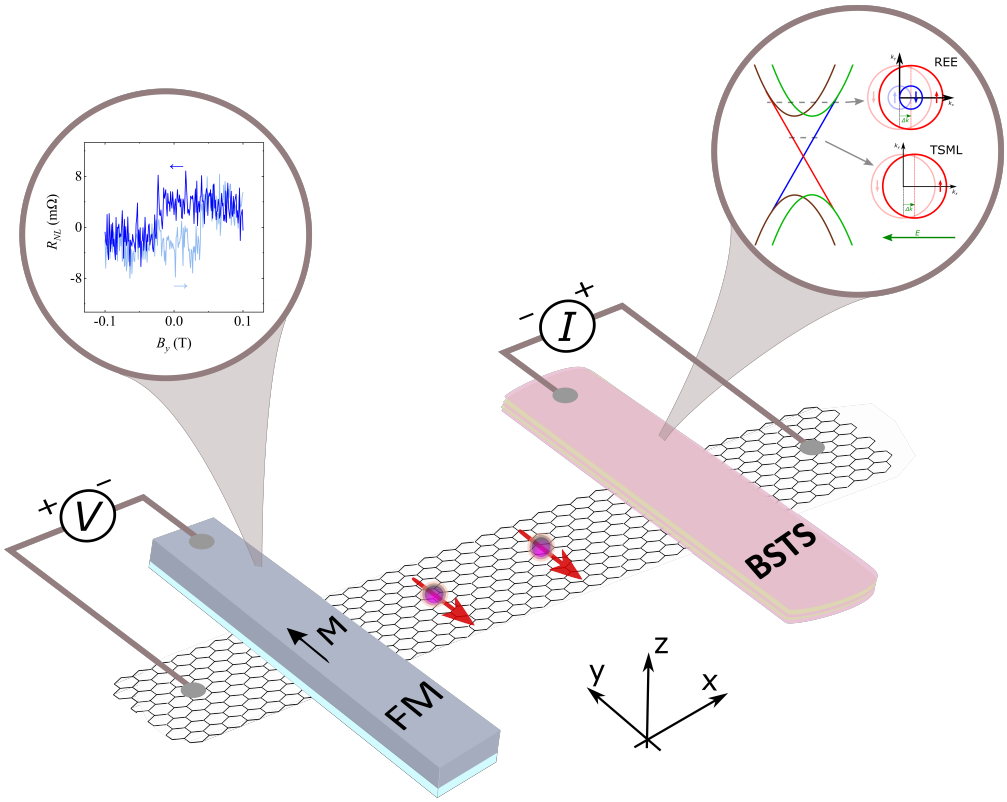

Room Temperature Charge-Spin Interconversion in a Topological Insulator and Graphene Heterostructure

Non-local electrical detection of charge-to-spin and spin-to-charge conversion in a van der Waals heterostructure of $Bi_{1.5}Sb_{0.5}Te_{1.7}Se_{1.3}$ and graphene

Master's thesis in Nanotechnology

LARS SJÖSTRÖM

DEPARTMENT OF MICROTECHNOLOGY AND NANOSCIENCE
CHALMERS UNIVERSITY OF TECHNOLOGY
Gothenburg, Sweden 2021
www.chalmers.se

Master's thesis 2021

Room Temperature Charge-Spin Interconversion in a Topological Insulator and Graphene Heterostructure

Non-local electrical detection of charge-to-spin and spin-to-charge conversion in a van der Waals heterostructure of $Bi_{1.5}Sb_{0.5}Te_{1.7}Se_{1.3}$ and graphene

LARS SJÖSTRÖM

CHALMERS
UNIVERSITY OF TECHNOLOGY

Department of Microtechnology and Nanoscience
Division of Quantum Device Physics
Spintronics Group
Chalmers University of Technology
Gothenburg, Sweden 2021

Room Temperature Charge-Spin Interconversion in a Topological Insulator and Graphene Heterostructure
Non-local electrical detection of charge-to-spin and spin-to-charge conversion in a van der Waals heterostructure of $Bi_{1.5}Sb_{0.5}Te_{1.7}Se_{1.3}$ and graphene
LARS SJÖSTRÖM

© LARS SJÖSTRÖM, 2021.

Supervisor and examiner:
Prof. Saroj Prasad Dash, Department of Microtechnology and Nanoscience, Chalmers University of Technology
Assistant supervisor:
Anamul Md Hoque, Department of Microtechnology and Nanoscience, Chalmers University of Technology

Master's Thesis 2021
Department of Microtechnology and Nanoscience
Division of Quantum Device Physics
Spintronics Group
Chalmers University of Technology
SE-412 96 Gothenburg
Telephone +46 31 772 1000

Cover: Schematic of a van der Waals heterostructure spin valve device with spin injection from a $Bi_{1.5}Sb_{0.5}Te_{1.7}Se_{1.3}$ flake and non-local spin detection with a ferromagnetic contact. The left inset shows a spin switch signal. The right inset shows a schematic of the electronic band structure of the topological insulator and the resulting charge-to-spin conversion mechanisms.

Typeset in LaTeX
Printed by Chalmers Reproservice
Gothenburg, Sweden 2021

Room Temperature Charge-Spin Interconversion in a Topological Insulator and Graphene Heterostructure
Non-local electrical detection of charge-to-spin and spin-to-charge conversion in a van der Waals heterostructure of $Bi_{1.5}Sb_{0.5}Te_{1.7}Se_{1.3}$ and graphene
LARS SJÖSTRÖM
Department of Microtechnology and nanoscience
Chalmers University of Technology

Abstract

The main goal of spintronics is to utilise the spin degree of freedom beyond conventional charge-based technologies and make faster and less energy-consuming non-volatile information technology. To realise this, efficient generation, transport and detection of polarised spin are necessary. Topological insulators are emerging materials for spin generation and detection in all-electrical spintronics applications, thanks to their strong spin-orbit coupling and the non-trivial spin-momentum locking of their unique topological surface states. Due to the efficient charge-to-spin conversion process, applying a bias current to induce a net carrier momentum should spontaneously generate a net spin polarisation in such a system. However, while charge-spin interconversion in topological insulators has previously been reported, reliable non-local measurements have so far been limited to cryogenic temperatures.

In this master's thesis, charge-to-spin and spin-to-charge conversion in the topological insulator $Bi_{1.5}Sb_{0.5}Te_{1.7}Se_{1.3}$ are detected in a non-local measurement method at room temperature, using a van der Waals heterostructure with a graphene spin valve device. These heterostructures make it possible to combine the spin polarisation of the topological insulator with the excellent spin transport properties of graphene. The observation of both spin switch and Hanle spin precession signals in the non-local geometry and detailed bias- and gate-dependent measurements prove the robustness of the charge-spin interconversion effects in topological insulators at room temperature. These findings demonstrate the possibility of using topological insulators to make all-electrical room-temperature spintronics devices.

Keywords: spintronics, topological insulator, $Bi_{1.5}Sb_{0.5}Te_{1.7}Se_{1.3}$, charge-spin interconversion, room temperature, van der Waals heterostructure, graphene, spin valve, spin switch, Hanle spin precession

List of publications

The following article is based on the work in this thesis. The manuscript is, at the time of writing, still in preparation.

[I] A. M. Hoque*, L. Sjöström*, D. Khokhriakov, B. Zhao and S. P. Dash. "Room temperature non-local detection of charge-spin interconversion in topological insulator using a heterostructure with graphene spin-valve device". *Manuscript in preparation* (2021).

* These authors contributed equally.

"The important thing is not to stop questioning. Curiosity has its own reason for existence."

— Albert Einstein

Acknowledgements

This master's thesis work has been a fantastic experience and I have learned a lot about nanotechnology, physics and otherwise. I would like to take this opportunity to express my sincere thanks to a number of people who have made this project possible as well as enjoyable.

First and foremost, I want to thank my supervisor Professor Saroj Prasad Dash. Your knowledge, guidance, ideas and feedback were a great help to me and were deeply appreciated.

Second, I want to thank my assistant supervisor Anamul Md. Hoque for helping me with fabrication, measurements and analysis. This work would have taken twice as long without your patient instructions.

Thank you also to the rest of the spintronics group: Dr Dmitrii Khokhriakov, Dr Bing Zhao and Dr Bogdan Karpiak, for your suggestions, help and enlightening discussions.

Xièxiè and *salamat* to Erdi Wang and Roselle Ngaloy for always being willing to discuss any issues that came up, and for the countless cups of tea.

This work was performed in part at Myfab Chalmers, and I want to thank the staff there for being helpful and letting me use their tools for my device fabrication.

Lastly, a very special thanks to my friends and family for their endless love, support and encouragement. None of this would have been possible without you. *Tack!*

Lars Sjöström

Gothenburg, September 2021

Contents

List of Figures **xv**

1 Introduction **1**

2 Theoretical Background and State of the Art **3**
2.1 Topological insulators 3
2.2 Charge-to-spin and spin-to-charge conversion 6
2.2.1 The spin Hall effect 7
2.2.2 The Rashba-Edelstein effect 10
2.2.3 Spin-momentum locking in topological surface states 13

3 Experimental **17**
3.1 Device fabrication 17
3.2 Measurement techniques 18
3.2.1 Spin valve 18
3.2.2 Spin switch 20
3.2.3 Hanle spin precession 22

4 Non-Local Electronic Detection of Spin Transport in Graphene at Room Temperature **27**
4.1 Spin valve measurements and bias current dependence 27
4.2 Hanle spin precession measurements and gate voltage dependence . . 31
4.3 Spin lifetime anisotropy 33

5 Non-Local Electronic Detection of Charge-Spin Interconversion in a Topological Insulator at Room Temperature **37**
5.1 Charge-to-spin conversion 37
5.2 Spin-to-charge conversion 45

6 Summary and Conclusions **49**

A Fabrication **I**
A.1 Fabrication process for the van der Waals heterostructure devices . . I
A.1.1 Chip preparation I
A.1.2 Electron beam lithography for graphene stripes I

A.1.3 Exfoliation of BSTS II
A.1.4 Mask design in AutoCAD II
A.1.5 Electron beam lithography, evaporation deposition and lift-off for nonmagnetic contacts III
A.1.6 Electron beam lithography, evaporation deposition and lift-off for magnetic contacts III

B MATLAB simulations **V**

C Supplementary results **VII**
C.1 Supplementary graphene results VII
C.2 Supplementary topological insulator results XII

List of Figures

2.1 Topological insulator 4
2.2 The TI $Bi_{2-x}Sb_xTe_{3-y}Se_y$ 6
2.3 The spin Hall effect 9
2.4 Origin of the Rashba-Edelstein effect 10
2.5 The Rashba-Edelstein effect 12
2.6 Topological spin-momentum locking 14

3.1 Coloured SEM image of a finished device 18
3.2 Spin valve measurement 19
3.3 Spin switch measurement 21
3.4 Hanle spin precession measurement 22
3.5 Asymmetry in signals from Hanle spin precession measurements . . . 24

4.1 Spin valve measurements 29
4.2 Hanle spin precession measurements 32
4.3 Spin lifetime anisotropy measurements 34

5.1 Graphene/TI heterostructure device for non-local detection of CSC in the TI 39
5.2 Measurement geometry dependence of the CSC signal 41
5.3 Bias current dependence of the CSC signal 43
5.4 Gate voltage dependence of the CSC signal 44
5.5 Spin-to-charge conversion in the TI 46

A.1 The device fabrication process II

B.1 Simulated Hanle spin precession signals plotted in MATLAB VI

C.1 Gate voltage dependence of spin valve signals in pristine graphene . . VII
C.2 Bias current dependence of the spin transport in a second device . . . VIII
C.3 Gate voltage dependence of the spin transport in a second device . . X
C.4 Bias current dependence of the spin transport in a third device XI
C.5 Gate voltage dependence of the spin transport in a third device . . . XII
C.6 Supplementary results from the CSC experiments XIII
C.7 Bias current dependence of the SCC signal XV
C.8 Gate voltage dependence of the SCC signal XVI
C.9 Local measurements of a TI flake XVII

1

Introduction

The tremendous advancements in condensed matter physics and fabrication methods of the last several decades have made possible a truly amazing development in electronics: computing power that previously would have taken up a whole room full of expensive equipment now handily and affordably fits in our pockets. These events have revolutionised and irreversibly changed most parts of society, and continue to do so as data processing and storage grow ever faster and ever more efficient.

The constant down-scaling in size of electrical components has been described by Moore's law, where the number of transistors per area on a chip doubles every two years [1]. However, as transistors are reaching the nanometre scale, new obstacles are encountered. At these length scales, quantum mechanical effects, such as quantum tunneling, become more dominant and give rise to increased leakage currents, causing more heat dissipation and larger energy losses as a result [2]. This is a serious problem, considering that information and communications technology already requires very large amounts of energy: it is predicted to stand for over 20% of the global electricity demand by 2030 [3].

One way of combating these energy dissipation issues is utilising the spin degree of freedom. In this approach, known as spintronics, information is encoded in spin-up and spin-down, instead of the positive and negative charges of conventional electronics. A great advantage with this is that switching between spin-up and spin-down requires orders of magnitude less energy than switching between different charge states [4]. Another benefit of spintronics is that spin-based processing requires only a polarised spin current and the net charge current can thus be zero, which eliminates heat dissipation from Joule heating [5].

While the main goal of spintronics is to utilise the spin degree of freedom for faster and less energy-consuming processing and storage of data [6, 7], there are several different branches that are striving towards this overarching goal: spin logic for data processing [8–10], spin qubits for spin-based quantum computing [11] and brain-inspired spin computing [12] as well as spin-transfer toque [13] and spin-orbit torque [14, 15] techniques for non-volatile magnetic memory applications. What all of these applications have in common is their need for efficient generation, transport and detection of polarised spins [16, 17].

Graphene is a widely used material with excellent spin transport properties. Its high charge carrier mobility and weak spin-orbit coupling (SOC) give rise to long spin lifetimes and spin diffusion lengths [6, 18]. However, the weak SOC of graphene also makes it practically impossible to use the material for spin generation and detection [19].

Topological insulators (TIs), on the other hand, have a very strong SOC and topological surface states with a unique electronic band structure that gives rise to spin-momentum locking (SML), where the charge carriers' spin polarisation and momentum are locked perpendicularly to each other [20]. By utilising this, efficient spin generation and detection can be achieved through charge-spin interconversion. While there are other ways to do this, such as optical and thermal spin generation and detection, electrical charge-spin interconversion has the advantage of easier implementation into conventional electronics [2, 17]. And while ferromagnetic (FM) contacts are a popular alternative for electrical charge-spin interconversion, they also cause complications such as stray field effects [21–23]. Because of this, TIs are a strong contestant for the best spin generation and detection method.

Because both graphene and TIs are layered materials, they can be stacked in van der Waals (vdW) heterostructures. This type of heterostructure, where the materials are held together by intermolecular vdW forces, makes it possible to combine the spin transport properties of graphene with the SML of TIs. Due to proximity effects, properties can also be induced between the materials, such as strong SOC being induced in graphene from the TI [24, 25], which further increases the usefulness and tunability of this kind of structure.

In this master's thesis work, devices of vdW heterostructures of graphene and a TI ($Bi_{1.5}Sb_{0.5}Te_{1.7}Se_{1.3}$) with both FM and nonmagnetic contacts are fabricated and then used for charge-spin interconversion experiments. The main goal is to achieve efficient charge-to-spin conversion (CSC) and spin-to-charge conversion (SCC) at room temperature, and then detect it electrically using a non-local geometry. This has never before been done with a TI with non-local measurements at room temperature, so successful results would be an excellent contribution towards room temperature spintronics.

The thesis is structured as follows. In Chapter 2, a theoretical background and the state of the art are introduced, and concepts such as TI, SOC, SML, the spin Hall effect and the Rashba-Edelstein effect are explained. Chapter 3 briefly presents the fabrication process of the vdW heterostructure devices and explains the different non-local measurement techniques that are used in this work. The obtained results are then shown in Chapters 4 and 5. In the former, the results from control experiments with spin transport in graphene are presented and discussed. Chapter 5 is the main chapter of this thesis, with results from the charge-spin interconversion experiments as well as an analysis of said results. This is followed by a summary and conclusions in Chapter 6. Finally, a more detailed description of the device fabrication process is given in Appendix A, the results of a few spin signal simulations are presented in Appendix B and supplementary results are shown in Appendix C.

2

Theoretical Background and State of the Art

The aim of this chapter is to give a theoretical background of topological insulators (TIs) and how they can be utilised for conversion between charge and spin currents, as well as to present an overview of the current state of the art. In the first section, TIs are introduced and their unique band structure and spin texture are explained, followed by a brief mentioning of the search for these materials and the methods for identifying them. In the second section, charge-to-spin and spin-to-charge conversion is discussed. Its three main origins: the spin Hall effect, the Rashba-Edelstein effect and the spin-momentum locking of TI surface states, are presented and their respective mechanisms are explained in detail. Historical and recent research achievements regarding each of the phenomena are also outlined.

2.1 Topological insulators

Topological insulators (TIs) are a subclass of topological quantum materials which lie somewhere in between trivial insulators (otherwise known as normal insulators) and metals, having both a bulk bandgap and metallic edge or surface states (for two-dimensional [2D] and three-dimensional [3D] TIs, respectively) [26]. The origin of this peculiar type of band structure (shown in Figure 2.1a) is a relativistic effect known as the inert pair effect. Due to the high speeds of the 1s electrons of heavy elements, the energy of the outermost s electrons is lowered [27]. For heavy element materials with s-type conduction bands, this means that the energy of the conduction band will be lowered and, if the band gap initially is small enough, an overlap with the valence band will occur [27]. However, since band crossing is forbidden by symmetry, the band crossing points will open up, resulting in band inversion and a bulk band gap [27]. The forming of the inverted band structure is summarised schematically in Figure 2.1b.

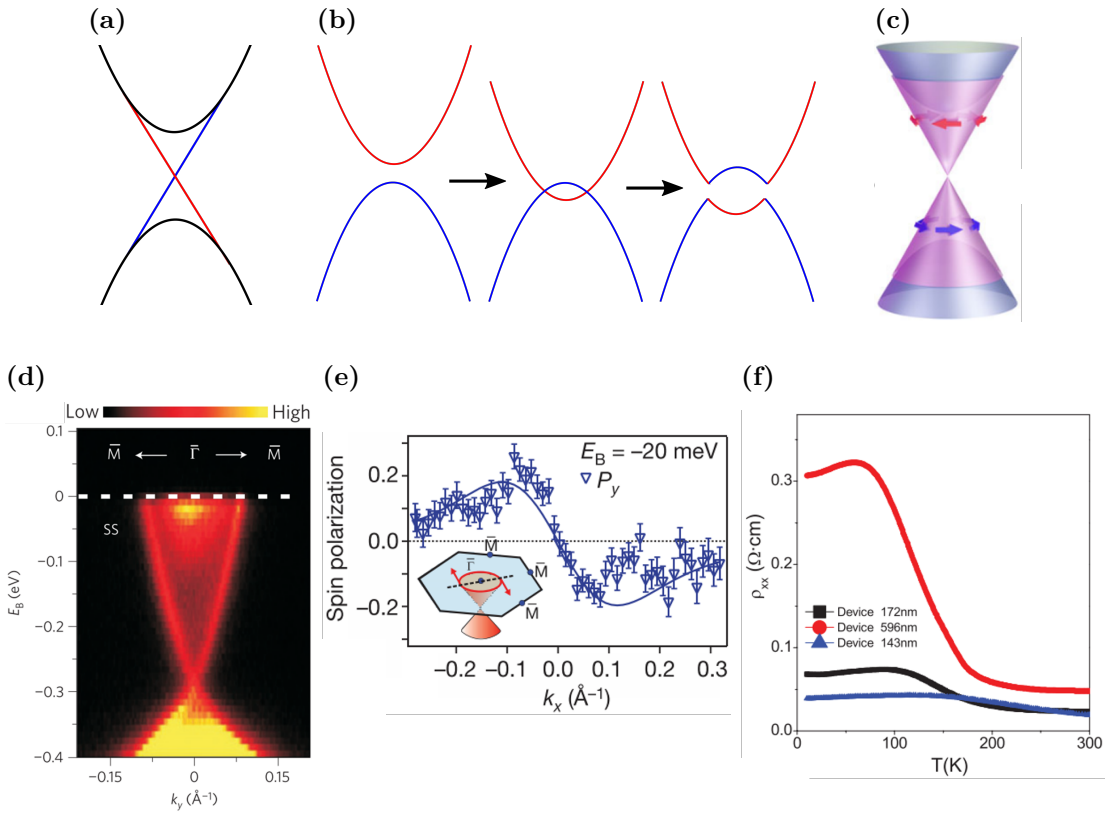

Figure 2.1: *Topological insulator.* **(a)** *2D schematic of the band structure of a topological insulator. While there is a band gap in the bulk of the material, there are also metallic surface states due to band inversion.* **(b)** *2D schematic explanation of the origin of the band inversion of a TI. The inert pair effect will lower the energy of the conduction band, causing an overlap with the valence band. Due to symmetry reasons, the crossing points open up and band inversion is formed.* **(c)** *3D schematic of the band structure of a topological insulator. The helicity of the spin-momentum locking of the surface states is shown by red and blue arrows above and below the Dirac point, respectively. Adapted from [28].* **(d)** *The surface states of Bi_2Se_3, detected with ARPES measurements. Adapted from [29].* **(e)** *The y component of the spin polarisation of the surface states of Bi_2Te_3, measured with spin-resolved ARPES. The measurement path is shown in the inset. Adapted from [30].* **(f)** *Temperature dependence of the resistivity for three $Bi_{1.5}Sb_{0.5}Te_{1.8}Se_{1.2}$ flakes of different thickness. The conductivity has a semiconducting behaviour down to about* 100 K*, after which the metallic surface conductivity dominates. The semiconducting behaviour is smaller for thinner flakes, where the bulk contributes less. Adapted from [31].*

At the surface of the TI, where there is an interface between the TI and a trivial insulator (which could be vacuum), there is no band crossing opening due to continuity reasons, and metallic surface states without a band gap are thus maintained [10, 32]. These linear surface states are highly interesting due to their spin-momentum locking (SML), which is caused by the strong spin-orbit coupling (SOC) of the surface states and locks the electron (or hole) spin polarisation perpendicularly to their momentum [2] (see Figure 2.1c). Since electrons (or holes) in the surface states can only change their momentum direction by flipping their spin (which is prevented

by time reversal symmetry), the surface states can be considered protected by time reversal symmetry and enable dissipationless spin transport that is insensitive to disorder [32]. The SML of the TI surface states is also promising for conversion between charge and spin currents, which will be further elaborated upon in Section 2.2.

The first TI was theoretically predicted by Kane and Mele for the case of graphene [32], but due to the very weak intrinsic SOC of the carbon atom and the subsequently very small band gap, the topological edge states of graphene remain restricted to experimentally inaccessibly low temperatures [18]. The first experimentally observed TI was 2D HgTe/CdTe quantum wells [33], and since then, other 2D TIs, such as InAs/GaSb/AlSb quantum wells [34], as well as 3D TIs, such as Bi_2Se_3 [35], Bi_2Te_3 [36], Sb_2Te_3 [36], $Bi_{2-x}Sb_xTe_{3-y}Se_y$ [37] and $Bi_{2-x}Sb_xTe_{3-y}S_y$ [38], have been discovered, totalling well over 300 different TIs [39].

Topological surface states were first observed in Bi_2Se_3 by Xia *et al.* [29] by using angle resolved photoemission spectroscopy (ARPES), shown in Figure 2.1d. Subsequent measurements with spin-resolved ARPES for Bi_2Te_3 [30] (see Figure 2.1e) confirmed the SML of the states. The latter has also been done electrically through spin potentiometric measurements [22, 40], which will be discussed further in Section 2.2.3. It has also been shown for TIs that the surface state conductance is independent from the bulk conductance [31, 38]. This was made through measurements of the resistivity through a TI flake for varying temperature, as shown for $Bi_{1.5}Sb_{0.5}Te_{1.8}Se_{1.2}$ in Figure 2.1f. The sharp increase in resistivity for temperatures below about 200 K happens because the bulk conductivity decreases due to freeze-out [38]. However, since the surface states are metallic, their conductivity increases at low temperatures due to the decreasing amount of phonon scattering [38], and this makes the surface state conductivity dominate below 100 K [31]. It can also be seen in Figure 2.1f that the semiconducting behaviour decreases for thinner TI flakes, which agrees with the reasoning above [31].

The TI that is investigated in this master's thesis project work: $Bi_{1.5}Sb_{0.5}Te_{1.7}Se_{1.3}$, is a 3D TI of the $Bi_{2-x}Sb_xTe_{3-y}Se_y$ group. It consists of stacks of quintuple layers which in turn consists of two layers of bismuth/antimony and three layers of tellurium/selenium, as illustrated in Figure 2.2a. The atoms in each layer are covalently bonded to each other and the layers are held together by van der Waals forces, similar to the layered structure of graphite. The composition of bismuth, antimony, tellurium and selenium in the TI can significantly affect properties such as bulk and surface conductivity, magnetoconductance, carrier concentration and carrier mobility [37, 41, 42]. It has been found by Ren *et al.* [37] that $x = 0.5$ and $y = 1.3$ gives a minimum bulk contribution to the conductivity of the TI (*i.e.* a more semiconducting bulk), and this is the composition that is used in this master thesis project work. However, subsequent studies in greater detail performed by Pan *et al.* [41] have shown that $x = 0.54$ and $y = 1.3$ give even lower bulk contribution (as shown in Figure 2.2b) and this could be an advantageous choice for future studies.

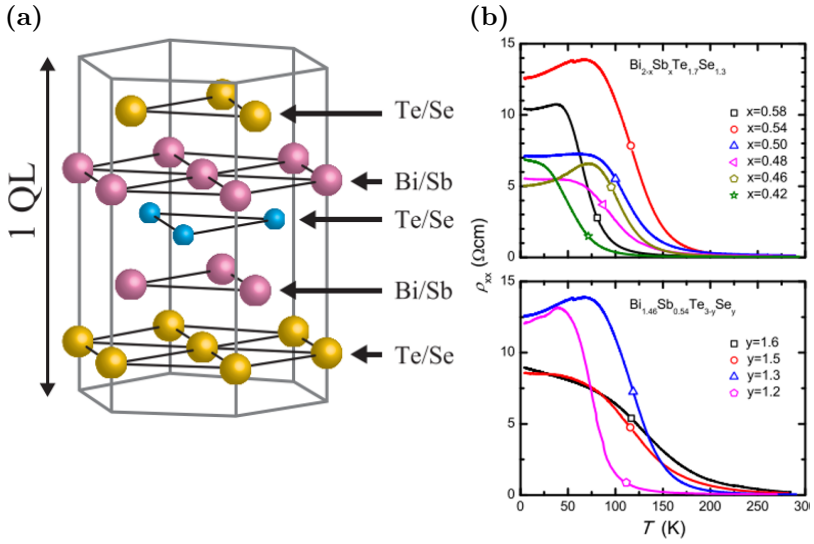

Figure 2.2: *The TI $Bi_{2-x}Sb_xTe_{3-y}Se_y$.* **(a)** *Crystal structure of a single quintuple layer (QL) of $Bi_{2-x}Sb_xTe_{3-y}Se_y$. Adapted from [43].* **(b)** *Temperature dependence of the resistivity of $Bi_{2-x}Sb_xTe_{3-y}Se_y$ for varying values of x (top) and y (bottom). The bulk contribution to the conductivity is found to be at a minimum for $x = 0.54$ and $y = 1.3$. Adapted from [41].*

2.2 Charge-to-spin and spin-to-charge conversion

Two essential phenomena in the field of spintronics are charge-to-spin conversion (CSC) and its inverse: spin-to-charge conversion (SCC). Through a range of different effects, an applied charge current can give rise to a spin polarised current or accumulation (or *vice versa*). Since these kinds of conversions are obviously extremely useful for manipulating and utilising spins, it is important to understand the possible origins of CSC and SCC, and this section will therefore explain the spin Hall effect, the Rashba-Edelstein effect and the spin-momentum locking of TI surface states.

For all of the aforementioned origins of CSC, spin-orbit coupling (SOC) is a central concept. This is the interaction between an electron's (or a hole's) spin and its movement, due to the effective magnetic field that is caused by the movement of a charge carrier through an electric field through the Lorentz effect [44]. The electric field in question can be the microscopic electric field of an atomic nucleus (intrinsic SOC) [45], but for spintronics applications in solids, macroscopic electric fields from *e.g.* semiconductor doping or band structure modulation (extrinsic SOC) are dominating due to electron screening of the atomic nuclei [44].

Although the extrinsic SOC is less dependent of the atomic number of the element than the intrinsic SOC (which has a Z^4 dependence, with Z as the atomic number [44]) due to electron screening, it still has a Z^2 dependence [18]. This means that, while heavy metals such as platinum and heavy element compounds like

$Bi_{2-x}Sb_xTe_{3-y}Se_y$ TIs have strong SOCs, graphene has a very weak SOC. The weak SOC of graphene is what gives the material its excellent spin transport properties with long spin lifetimes and diffusion lengths, but it also makes spin manipulation through CSC and similar effects in graphene practically impossible [19]. It is therefore desirable to combine strong SOC with the weak SOC of pristine graphene. One route for this is to use materials with strong SOC (such as TIs) for spin manipulation and use graphene for spin transport. An alternative path is to artificially enhance the SOC of graphene, which would make it possible to transport and manipulate spins in a single material.

Some of the first attempts to increase the SOC of graphene used functionalised graphene through chemisorbed adatoms [19, 46]. However, while this approach succeeded in enhancing the SOC, it also disturbed the sp^2 hybridisation of the graphene orbitals and thus impaired the material's transport properties [6]. A more successful strategy has been to instead utilise proximity effects by stacking graphene and high-SOC materials on top of each other in van der Waals (vdW) heterostructures [25, 47–49]. Similarly, proximity effects have also been used to induce other new properties into graphene, such as magnetism [23, 50] and superconductivity [51], although this will not be discussed further here.

2.2.1 The spin Hall effect

The spin Hall effect (SHE) is a CSC mechanism that gives rise to a spin polarised current in nonmagnetic materials with a strong SOC when a charge current is passed through it [16]. Depending on its origin, the SHE is referred to either as extrinsic or intrinsic.

In the extrinsic SHE (also known as the skew-scattering SHE), the spin current is generated through scattering [52]. When an unpolarised charge current flows through the nonmagnetic material, the charge carriers will mainly scatter in opposite directions depending on their spins, due to the SOC [16]. In this way, charge carriers of opposite spin polarisation will be pulled towards opposite edges of the material by an effective spin-orbit force and a transverse spin current is generated. This mechanism of the SHE was originally proposed by D'yakonov and Perel' [53], based on previous experiments in vacuum by Mott [54], and was first detected experimentally by Kato *et al.* [55].

However, the SHE can exist even in the absence of scattering through the intrinsic SHE. Here, the origin of the effect is strong SOC, similarly to the anomalous Hall effect [56], and the spin-orbit force comes from the movement of charge carriers travelling through the spin-orbit field of a perfect crystal [16]. This was first predicted by Murakami *et al.* [57] and Sinova *et al.* [56], and was first shown experimentally by Wunderlich *et al.* [58].

The inverse SHE (ISHE) is the Onsager reciprocal of the SHE and the corresponding SCC mechanism [10]. When a polarised spin current is passed through the material, the charge carriers are deflected in the same way as described above. However, since

up and down spins in a spin current already move in opposite directions, both types of spin are deflected in the same direction and a transverse charge current is thereby formed.

Normally, the SHE and the ISHE are observed in the bulk of 3D materials since the effect requires a right-handed orthogonality between the spin current direction, the charge current direction and the spin polarisation [10]. It has been shown that for layered materials, such as MoS_2, an in-plane charge current in the y direction will give rise to a spin current in the out-of-plane z direction with in-plane spins in the x direction through the SHE (see Figure 2.3b) [25]. If the material is placed on top of graphene in a vdW heterostructure, the polarised spin current can be injected into the graphene channel and cause a spin current along the x direction [25]. However, this kind of heterostructure can also give rise to a SHE in the graphene itself due to proximity-induced SOC. Since the 2D character of graphene restricts the charge and spin currents to be in the xy plane, the proximity-induced SHE in graphene will only allow out-of-plane spins (see Figure 2.3a). Because of this, bulk SHE of the 3D material and proximity-induced SHE in graphene can be distinguished from each other through observation of the spin polarisation direction. Following this reasoning, bulk SHE has been detected in the TI $Bi_{1-x}Sb_x$ [59, 60] and proximity-induced SHE has been detected in graphene/MoS_2 [25], graphene/WS_2 [47] and graphene/WSe_2 [48] vdW heterostructures, up to room temperature.

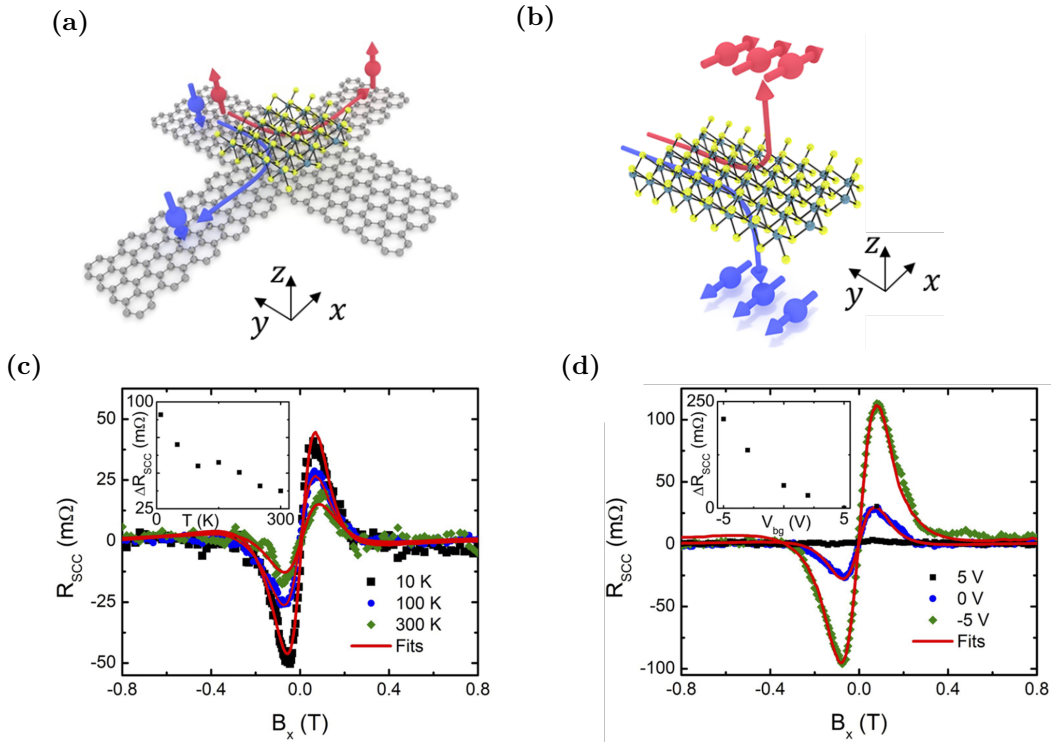

Figure 2.3: *The spin Hall effect.* **(a)** *Schematic of the proximity-induced SHE in a graphene/MoS_2 vdW heterostructure. When an in-plane charge current is applied along the y direction across the proximitised graphene, the SHE deflects out-of-plane spins and thereby causes an in-plane spin current along the x direction.* **(b)** *Schematic of the SHE in the bulk of MoS_2 with its layers in the xy plane. A charge current along the y direction gives rise to a spin current in the z direction with spins polarised along the x direction. Adapted from [25].* **(c)** *Hanle spin precession signals measured for a graphene/WSe_2 device at different temperatures and $V_g = 0\,\mathrm{V}$, showing a large temperature dependence for the proximity-induced SHE.* **(d)** *Hanle spin precession signals measured for a graphene/WSe_2 device at different gate voltages and $T = 100\,\mathrm{K}$, showing a large gate dependence for the proximity-induced SHE. Adapted from [48].*

The conventional figure of merit for the efficiency of the SHE is the spin Hall angle θ_{SHE}, which is the ratio of spin current density to charge current density [10]. The previously mentioned bulk SHE experiments in TIs have yielded controversial results with spin Hall angles well above 100% [59]. For proximity-induced SHE, experiments have measured $\theta_{SHE} = -0.33\%$ for graphene/MoS_2 [25], $\theta_{SHE} = 0.3\%$ for graphene/WS_2 [47] and $\theta_{SHE} = 1.7\%$ for graphene/WSe_2 [48], at room temperature. The efficiency can, however, be further increased, as the proximity-induced SHE has been shown to be strongly dependent both on temperature and on gate voltage [25, 47, 48] as exemplified by Figures 2.3c and 2.3d. These spin Hall angles are still orders of magnitude lower than those of bulk materials with strong SOC, such as platinum, but it has been argued that this is an unfair comparison. This is because the spin Hall angle fails to consider the losses of spin current that will arise from the necessary spin transport from the heavy metal to the spin transport material, whereas the proximity-induced SHE avoids such losses by using graphene

both for CSC and for spin transport [10]. Instead, an effective spin Hall resistance, which is the ratio between the output voltage and input spin current that enters the conversion region, has been proposed [48]. Using this alternative figure of merit, the efficiency of the proximity-induced SHE for a graphene/WSe_2 heterostructure is orders of magnitude larger than that of a comparable graphene/Pt device [48], clearly showing the great potential of the former.

2.2.2 The Rashba-Edelstein effect

The Rashba-Edelstein effect (REE) is a CSC mechanism that is based on Rashba SOC. Rashba SOC itself originates from the electric field that is caused by a broken structural inversion symmetry in a material [10]. When electrons move through this electric field, they experience an effective magnetic field which locks their spins and momenta perpendicular to each other and an in-plane SML spin texture is thus generated perpendicular to the electric field [61]. The spin texture can also be seen as a consequence of the spin-up and spin-down sub-bands shifting in momentum space as the Rashba SOC lifts their spin degeneracy [62]. Both the shifted sub-bands and the SML of the Fermi surface are shown in Figure 2.4b and as the faded circles in Figure 2.4a, respectively.

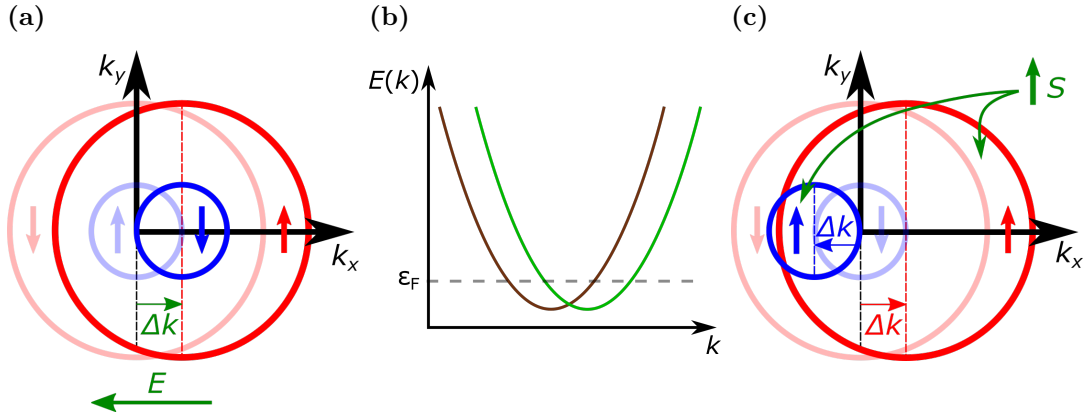

Figure 2.4: *Origin of the Rashba-Edelstein effect.* **(a)** *Schematic of the Fermi surface spin texture of a Rashba SOC material during CSC. The spin-split sub-bands give rise to two spin windings with opposite helicity. When a charge current is applied in the $-x$ direction, the spin texture is shifted by Δk in the $+x$ direction and a net $+y$ accumulation occurs.* **(b)** *Schematic of the spin-up and spin-down sub-bands being shifted in k space due to Rashba SOC. The Fermi level that is depicted in* (a) *is shown.* **(c)** *Schematic of the Fermi surface spin texture of a Rashba SOC material during SCC. A $+y$ spin accumulation shifts the two circles an equal amount in opposite directions in k space, giving rise to a net charge current in the $+x$ direction.*

As opposed to the SHE, the REE is a 2D effect and converts a charge current into a uniform spin density rather than a spin current [10, 16]. If a charge current is passed in the $-x$ direction through a material with Rashba SOC, the average electron $+x$ momentum increases by Δk and the equilibrium spin texture is therefore shifted to

the right [63], as shown in Figure 2.4a. Because of the winding spin texture of the outer circle, this will cause a higher occupation of electronic states with spins in the $+y$ direction and a lower occupation of states with $-y$ spins, *i.e.* an accumulation of spins with $+y$ spin polarisation is formed [47]. The inner circle of the Fermi surface does have an opposite spin winding and will to some extent cancel the effect of the outer one, but since the inner circle is smaller, it will have a smaller impact, and the net polarisation is therefore nonzero [64]. The polarised spin density will then diffuse in both directions along the y axis, unlike the spin current of the SHE [25].

The Onsager reciprocal of the REE is known as the inverse REE (IREE). Here, a $+y$ spin accumulation causes the spin textures of the Fermi surface to shift along the k_x axis, as visualised in Figure 2.4c [65]. Because of the opposite helicity of the outer and the inner circle, they will to an extent cancel the effect of each other. Nevertheless, there will be a nonzero net momentum increase in the $+x$ direction, which translates to a charge current in the $-x$ direction [66].

In vdW heterostructures, the broken inversion symmetry comes from the asymmetric potential of the interface between the two materials [63] and the Rashba SOC will therefore appear parallel to the interface. The geometry of the REE, as explained above, is visualised for the case of a graphene vdW heterostructure in Figure 2.5a. Since the polarised spins from the REE are in-plane, the REE can be differentiated from the proximity-induced SHE (which causes out-of-plane spin polarisation; see Section 2.2.1). It is, however, not possible to recognise the REE from the bulk SHE in this way, since both effects give in-plane-polarised spins.

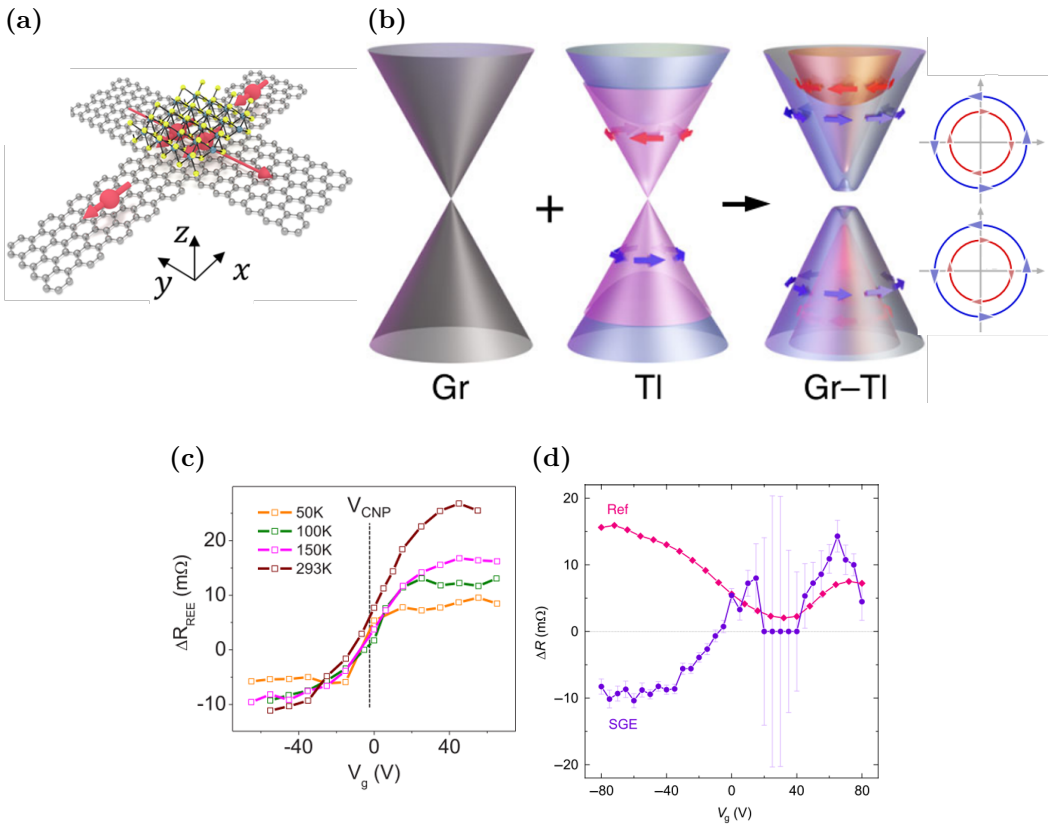

Figure 2.5: *The Rashba-Edelstein effect.* **(a)** *Schematic of the REE from proximity-induced SOC in a graphene/MoS_2 vdW heterostructure. When an in-plane charge current is applied along the y direction across the proximitised graphene, the REE generates an in-plane spin polarisation along the x direction and the polarised spins then diffuse along the x direction. Adapted from [25].* **(b)** *Schematics of the band structures of pristine graphene, a TI and graphene with Rashba spin-split bands due to proximity-induced SOC. The helicity of the winding spin texture of the proximitised graphene is shown by arrows and further visualised by cross sections of the graphene conduction and valence bands. Note that the spin texture has the same helicity above and below the Dirac point of the proximitised graphene, as opposed to the TI. Adapted from [28].* **(c)** *The magnitude of REE in a graphene/2H-TaS_2 vdW heterostructure, measured through xHanle, as a function of gate voltage for different temperatures, showing both gate and temperature dependence of the REE. Adapted from [63].* **(d)** *The magnitude of the IREE in a graphene/$(Bi_{0.05}Sb_{0.85})_2Te_3$ vdW (purple), measured through Hanle spin precession, as a function of gate voltage at room temperature, showing a large gate dependence of the IREE. Also shown is the corresponding Hanle spin precession signal for pristine graphene in the same device (pink), as a reference. Adapted from [28].*

Instead, the REE (more specifically, the proximity-induced REE) and the bulk SHE can be differentiated by their gate voltage dependence. Graphene with Rashba spin-split bands, caused by proximity-induced SOC, has a winding spin texture with the same helicity above and below the Dirac point [28], as illustrated in Figure 2.5b. Because of this, electrons and holes with the same spin will gain the same momentum from the SML. However, since they have opposite charge, the charge current that

is generated by a certain spin polarisation will have opposite sign depending on whether the Fermi surface is above or below the Dirac point (or equivalently for the CSC case) [28]. In other words, the SCC and CSC that come from proximity-induced REE are odd with gate voltage around the graphene Dirac point. The bulk REE and the bulk SHE do have a similar odd gate dependences, but the Fermi level needs to be shifted between the TI conduction and valence bands for this to happen, which requires very large applied gate voltages [28, 67].

The Rashba SOC and its resulting SML were originally proposed by Bychkov and Rashba [68], which explained experimental results in GaAs/AlGaAs structures by Störmer *et al.* [69] and Stein *et al.* [70]. The full REE with its CSC was predicted by Edelstein [71] and later experimentally demonstrated by Rojas Sánchez *et al.* [72]. In recent years, the REE and/or its inverse have been experimentally observed in graphene with proximity-induced Rashba SOC in vdW heterostructures with the TMDCs WS_2 [47, 64], 2H-TaS_2 [63] and 1T'-$MoTe_2$ [67] as well as the TIs Bi_2Se_3 [73], $Bi_{1.5}Sb_{0.5}Te_{1.7}Se_{1.3}$ [73] and $(Bi_{0.05}Sb_{0.85})_2Te_3$ [28].

The conversion efficiency parameter γ, which is the ratio between charge current density and spin accumulation of the SCC, is often used as a figure of merit for the IREE, but the unitless figure of merit α has also been proposed [25], where the spin accumulation is assumed to convert into a spin current through diffusion and α is obtained as the ratio of 2D charge current to 2D spin current [10]. The advantage of the latter is that it can be compared directly to the spin Hall angle [25]. The conversion efficiencies of the aforementioned proximitised graphene structures were $\alpha = 0.1\%$ for WS_2 [47], up to $\alpha = 4.3\%$ for 2H-TaS_2 [63], $\alpha = 7.6\%$ for 1T'-$MoTe_2$ [67] and up to $\alpha = 4.8\%$ for $(Bi_{0.05}Sb_{0.85})_2Te_3$ [28] at room temperature. Similarly to the proximity-induced SHE, the REE has been shown to be strongly tunable with temperature and gate voltage [10], as exemplified in Figures 2.5c and 2.5d. This type of tunability, especially through the use of gate voltage, seems promising for applications in versatile CSC and SCC.

2.2.3 Spin-momentum locking in topological surface states

Similarly to the REE, CSC can also happen due to the SML of the topological surface states (TSS) in a TI. The linear dispersion relation (shown *versus* k in Figure 2.6b) becomes spin-polarised Dirac cones when plotted against k_x and k_y, and the Fermi surface has a spin texture with a single SML circle [74]. When a charge current is applied in the $-x$ direction, the average electron momentum increases by Δk in the $+x$ direction and the spin texture is shifted to the right in k space, as shown in Figure 2.6a. The SML of the TSS will then give rise to an increased spin polarisation in the $+y$ direction [75]. This CSC mechanism is often simply referred to as SML, but it is also known as the Edelstein effect. However, since the REE is also based on SML, and due to the similar names of the Edelstein effect (EE) and the REE, the CSC that comes from the SML of TSS will henceforth be referred to as the topological SML (TSML), to avoid confusion. The mechanical similarity between the TSML and the REE is evident, but the difference is the origin of the winding SML spin texture: in the REE, Rashba SOC results in spin-split bulk bands and a

Fermi surface with two spin windings of opposite helicity [61], while, in the TSML, a Fermi surface with a single spin winding is caused by the TSS of a TI [22].

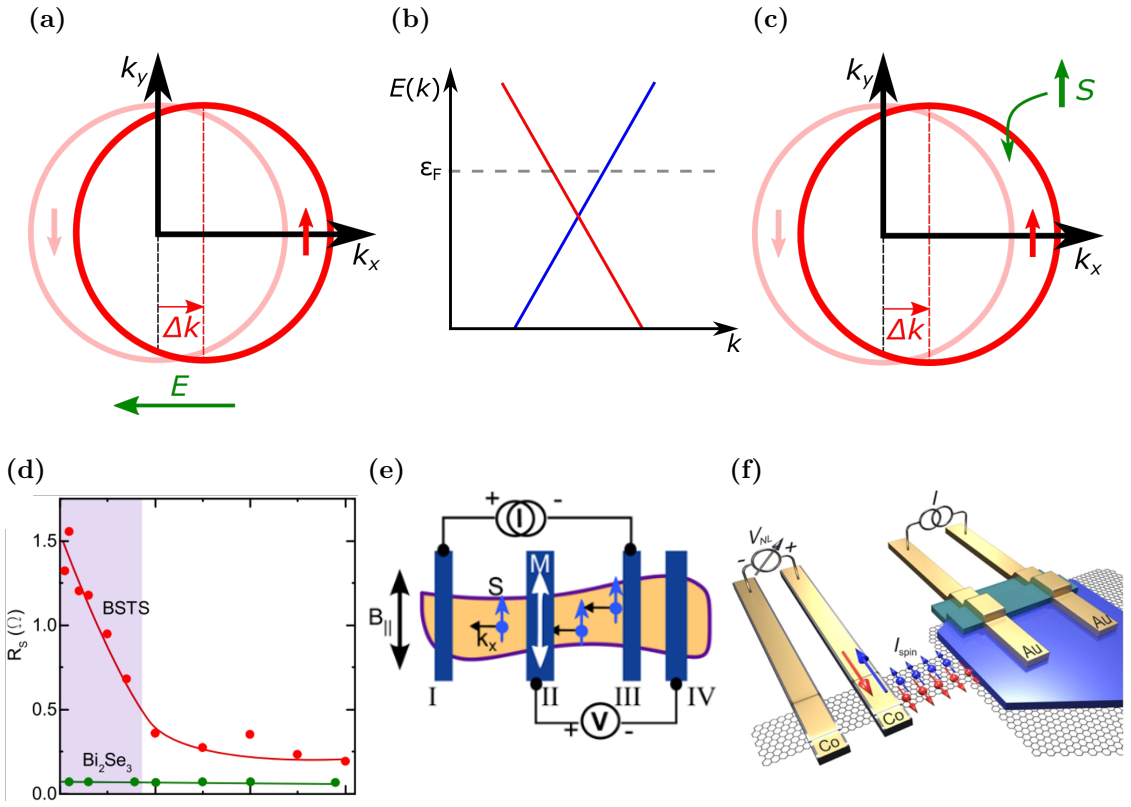

Figure 2.6: *Topological spin-momentum locking.* **(a)** *Schematic of the Fermi surface spin texture of TSS during CSC. The linear dispersion relation of the TSS gives rise to a single spin winding, as opposed to the case for the spin-split bulk bands in the REE (see Figure 2.4a). When a charge current is applied in the $-x$ direction, the spin texture is shifted by Δk in the $+x$ direction and a $+y$ spin accumulation occurs.* **(b)** *Schematic of the metallic TSS of a TI. The Fermi level that is depicted in* (a) *is shown.* **(c)** *Schematic of the Fermi surface spin texture of TSS during SCC. A $+y$ spin accumulation shifts the spin texture in k space and gives rise to a charge current in the $-x$ direction.* **(d)** *The magnitude of the TSML in $Bi_{1.5}Sb_{0.5}Te_{1.7}Se_{1.3}$ and Bi_2Se_3, respectively, from spin switch measurements, as a function of temperature. The coloured background represents the temperature range where surface conductance is dominating in $Bi_{1.5}Sb_{0.5}Te_{1.7}Se_{1.3}$. There is a large temperature dependence of the CSC magnitude for $Bi_{1.5}Sb_{0.5}Te_{1.7}Se_{1.3}$ but not for Bi_2Se_3. Adapted from [22].* **(e)** *Measurement setup where a current is passed across the TI and the spin current is detected locally as a voltage between a contact inside the current loop and a contact outside of it. Adapted from [40].* **(f)** *Measurement setup where a current is passed across the TI and the spin current is injected into a graphene channel and detected non-locally between two contacts on the graphene. Adapted from [21].*

SCC through the TSML works as depicted in Figure 2.6c. An applied $+y$ spin accumulation shifts the Fermi surface spin texture from the equilibrium position, and the electrons gain an increase in their momentum by Δk in the $+x$ direction,

which is equivalent to a charge current in the $-x$ direction [74]. Analogously to its Onsager reciprocal, this SCC mechanism is also known as the inverse Edelstein effect. However, since both the CSC and the SCC result from SML (*i.e.* there is no such thing as an inverse SML), they will here both be referred to as the TSML, and the context will show which one is meant.

Just like the REE, the TSML is a 2D effect that produces an in-plane spin density from a charge current [76]. While this makes it easy to distinguish the TSML from the proximity-induced SHE, it makes it more difficult to differentiate between the bulk SHE, the REE and the TSML. The gate voltage dependence can, however, be used to distinguish between the TSML and the proximity-induced REE. As shown in Figure 2.1c, the winding spin texture of the TSS has opposite helicity above and below the TI Dirac point [22]. This means that both the momentum and the charge of the charge carriers change for a given spin polarisation when the Fermi level is moved across the TI Dirac point, which results in the charge current keeping its sign [28]. This is opposite to the proximity-induced REE in graphene (explained in Section 2.2.2), where the SML helicity is the same for holes and electrons and there is a sign change when the Fermi level is moved across the graphene Dirac point, and the two CSC effects can in this way be distinguished.

Although TIs were yet to be discovered at the time, the first theoretical prediction of the TSML is considered to be the same as the first theoretical prediction of the REE by Edelstein [71]. This is because the prediction of CSC is based on the existence of SML rather than on the origin of said SML. The first experimental demonstration of TSML was made in Bi_2Se_3 by Li *et al.* at cryogenic temperatures [77]. Since then, TSML has been detected in the TIs Bi_2Se_3 [40, 78, 79] and $(Bi_{1-x}Sb_x)_2Te_3$ [80] at room temperature and in the TIs Bi_2Te_2Se [21], $Bi_{1.5}Sb_{0.5}Te_{1.7}Se_{1.3}$ [22, 81] and $(Bi_{1-x}Sb_x)_2Te_3$ [75, 82] at cryogenic temperatures. A similar CSC effect has also been predicted in the TSS of Weyl semimetals [83].

Most of the experimental demonstrations of TSML were performed through local spin potentiometric measurements in setups similar to the one in Figure 2.6e. Here, ferromagnetic (FM) contacts are used for measuring the voltage between the contact inside the current loop and the contact outside of it. Due to the FM characteristics of the contacts, the measured voltage will change depending on the spin polarisation of the current across the TI (see Section 3.2 for a more detailed description). These local measurements have, however, the disadvantage that the detected signal can also be caused by stray field effects from the FM contacts [21, 22]. A way to circumvent this is to inject the polarised spin current into a graphene channel and detect it non-locally (see Figure 2.6f), which was accomplished by Vaklinova *et al.* [21] in Bi_2Te_2Se at cryogenic temperatures.

The conventional figure of merit for the efficiency of the TSML SCC is the TSML length λ_{TSML}, which is defined as the ratio of 2D surface charge current to 3D spin current and has the unit of length [47, 80]. Reported values from the aforementioned experiments include $\lambda_{TSML} = 35\,\text{pm}$ for Bi_2Se_3 [78] and $\lambda_{TSML} = 75\,\text{pm}$ for $(Bi_{1-x}Sb_x)_2Te_3$ [80]. Interestingly, TSML lengths as high as 280 pm have been ob-

tained in Bi_2Se_3 due to the greatly increased SOC of hybridised TSS-Rashba bands, where the TSML and the REE both contribute to SCC [74].

While some TIs show a strong temperature dependence of their TSML magnitude, others do not, as exemplified in Figure 2.6d. The increase in CSC (or SCC) at low temperatures most likely stems from the transition from bulk to surface dominated transport due to freeze-out, which both increases the fraction of charge carriers in the TSS and decreases the surface-bulk scattering [22]. That being said, this effect seems to be negligible for Bi_2Se_3, which has a temperature-independent TSML [40].

3

Experimental

The experimental part of this master's thesis project constituted of fabrication and measurements. In the fabrication part, microfabrication techniques were used to make devices based on van der Waals heterostructures of the topological insulator $Bi_{1.5}Sb_{0.5}Te_{1.7}Se_{1.3}$ and graphene. The measurement part aimed towards investigating charge-spin interconversion and spin transport in the devices through non-local electronic and magnetotransport measurements. In this chapter, this is explained further, giving a context and an introduction to the obtained results that are shown and analysed in Chapters 4 and 5.

3.1 Device fabrication

The central component of the devices were van der Waals (vdW) heterostructures of $Bi_{1.5}Sb_{0.5}Te_{1.7}Se_{1.3}$ (BSTS) and graphene. Graphene stripes were initially made with electron beam lithography from chemical vapour deposition (CVD) graphene on a Si/SiO_2 chip. BSTS flakes were then exfoliated mechanically from a bulk crystal using the Scotch tape method and transferred onto the chip to form a graphene/BSTS vdW heterostructures.

Non-magnetic gold contacts and ferromagnetic cobolt contacts were made through the lift-off method, using electron beam lithography for contact patterning and high vacuum evaporation deposition for metal deposition. The gold deposition was preceded by the deposition of a thin chromium layer for increased adhesion. The cobolt deposition was instead preceded by the deposition of a thin titanium layer, which was oxidised *in situ* to make TiO_2 tunnel barriers. One example of a finished device is shown in Figure 3.1.

The entire fabrication process is described in greater detail in Appendix A.

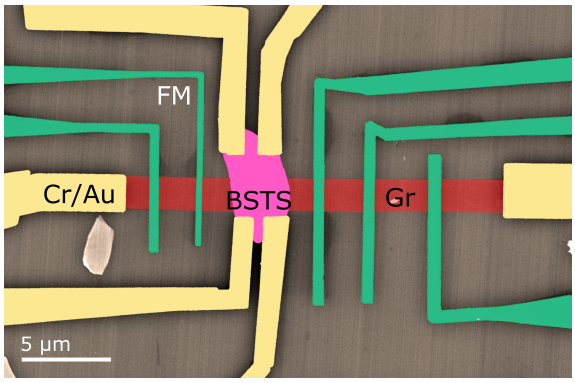

Figure 3.1: *Coloured SEM image of a finished device. The major component of the device is the graphene/BSTS heterostructure, and nonmagnetic and FM contacts are used for injection and detection of charge and spin currents.*

3.2 Measurement techniques

Three main measurement methods were used for detecting spin polarised currents: spin valve, spin switch and Hanle spin precession. All of these methods utilise the fact that electrons will enter a ferromagnetic (FM) contact only if the electrons' spin polarisation is aligned with the magnetisation of the contact [64]. The general setups for each of the measurement types are described in the following sections.

The measurements in this master's thesis projects are referred to as non-local, meaning that the voltage is measured outside of the charge current loop in a four-terminal configuration (see *e.g.* Figure 3.2a), as opposed to local measurements, where two contacts are used both for running a charge current and for measuring the voltage [6]. The advantage of non-local measurements is that a pure spin current is being measured without any interference from the charge current. This gives a higher signal-to-noise ratio due to the avoidance of the background that would otherwise have been caused by the charge current [6, 18].

The DC bias current and the gate voltage were applied using a Keithley 6221 current source and a Keithley 2400 source meter, respectively, and the non-local voltage was measured by a Keithley 2182A nanovoltmeter. The external magnetic field was applied using a GMW 5403 electromagnet.

3.2.1 Spin valve

A general non-local spin valve measurement setup for a graphene channel is shown in Figure 3.2a. As a charge current is passed through a portion of the graphene stripe, electrons are injected from the left FM contact into the graphene. Since the injection contact is FM, these injected electrons will have their spin polarisation aligned with the contact magnetisation direction and a spin current is thus injected into the graphene [17]. While the charge current will go directly to the nonmagnetic contact on the very left of the device, the spin current will diffuse in both directions

along the graphene channel [84] and can be detected as a non-local voltage between the right FM contact and the nonmagnetic reference contact on the very right.

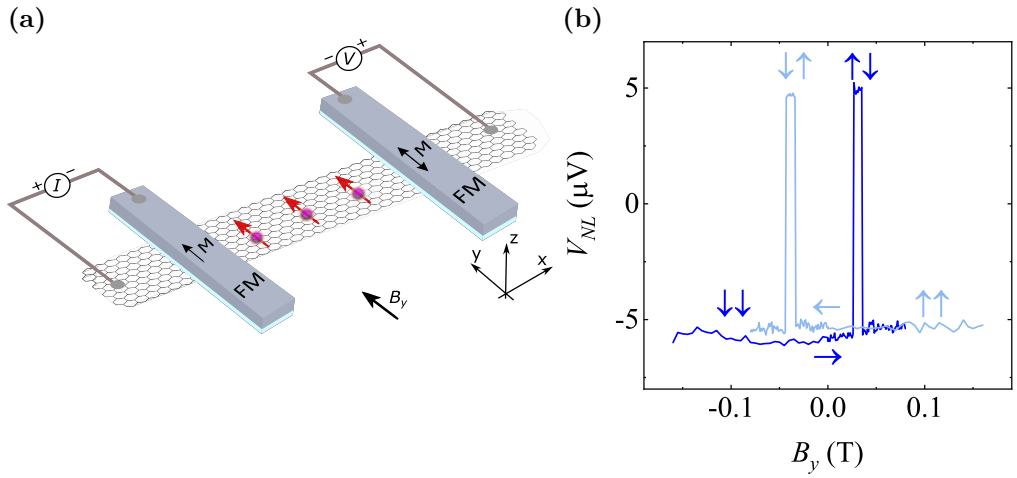

Figure 3.2: *Spin valve measurement.* **(a)** *Schematic of spin valve measurement setup.* **(b)** *An example of a signal from a spin valve measurement. The dark blue curve is for sweeping the external magnetic field from the $-y$ to the $+y$ direction and the light blue one is for sweeping from $+y$ to $-y$. The vertical arrows indicate the magnetisation direction of the injector and the detector electrodes.*

The FM contacts will have their magnetisation along their easy axis, which here is along the length of the contacts [64]. Both directions along the easy axis (parallel and antiparallel) are energetically equivalent, but energy must be supplied in order to reverse the magnetisation, since that requires rotation out of the easy axis direction [85]. By sweeping an external magnetic field in the y direction, B_y, from negative to positive (or *vice versa*), the magnetisation of each of the FM contacts can thus be switched. For a strong magnetisation in the $-y$ direction, the injector and the detector electrodes will both have their magnetisation along the $-y$ direction and the injected electron spins are therefore parallel to the detector's magnetisation. This will continue until the external field B_y is strong enough in the $+y$ direction to switch the magnetisation of one of the contacts, leading to the injected spins being antiparallel to the detector and consequently a sudden increase in detected voltage [6]. When the external magnetic field is increased further, the magnetisation of the other contact will switch and the voltage signal suddenly decreases again. An example of the obtained signal is shown in Figure 3.2b. Since a higher magnetic field is needed to switch the magnetisation of a thinner FM electrode (*i.e.* a thinner electrode has a higher coercivity than a wider one) [86, 87], contacts of different widths can be used to increase the range in B_y for which the contact magnetisations are in the antiparallel configuration.

The main thing that can be learned from spin valve measurements is the presence of spin transport between the injector and detector electrodes, since the signal amplitude corresponds to spin polarisation by the detector contact. The polarisation

of the FM contacts P_{FM} (*i.e.* the spin injection or detection efficiency) can also be determined. For tunnel contacts, it can be calculated from

$$\Delta R_{NL} = \frac{{P_{FM}}^2 R_{\square} \lambda_s}{W_{Gr}} \exp\left(\frac{-L}{\lambda_s}\right), \tag{3.1}$$

where ΔR_{NL} is the amplitude of the measured non-local resistance (the measured non-local voltage divided by the applied bias current), $R_{\square}$ and W_{Gr} are the sheet resistance and the width of the graphene channel, respectively, λ_s is the spin diffusion length and L is the distance between the FM electrodes [86, 88, 89]. Here, it is assumed that the contact-to-graphene interfaces for the contacts are similar, so that both contacts have identical polarisations.

3.2.2 Spin switch

Two versions of a general setup for non-local spin switch measurement of a topological insulator (TI) on a graphene channel are shown in Figures 3.3a and 3.3b. This kind of measurement is very similar to spin valve measurements. The difference is that one of the FM contacts in spin valve has been exchanged for a nonmagnetic contact on top of a TI flake.

In the setup in Figure 3.3a, a charge current is injected through a nonmagnetic contact into the TI. A part of the injected current will be polarised by the charge-to-spin conversion (CSC) of the TI and a spin current is thus injected from the TI to the graphene channel [21]. This spin current can then be detected non-locally by the FM contact in the same way as in spin valve measurements. An example of the obtained spin signal is presented in Figure 3.3c. Since the spin polarisation from the TI CSC is unaffected by the external magnetic field [16], there is only one jump in non-local voltage (which is caused by magnetisation switching of the FM contact).

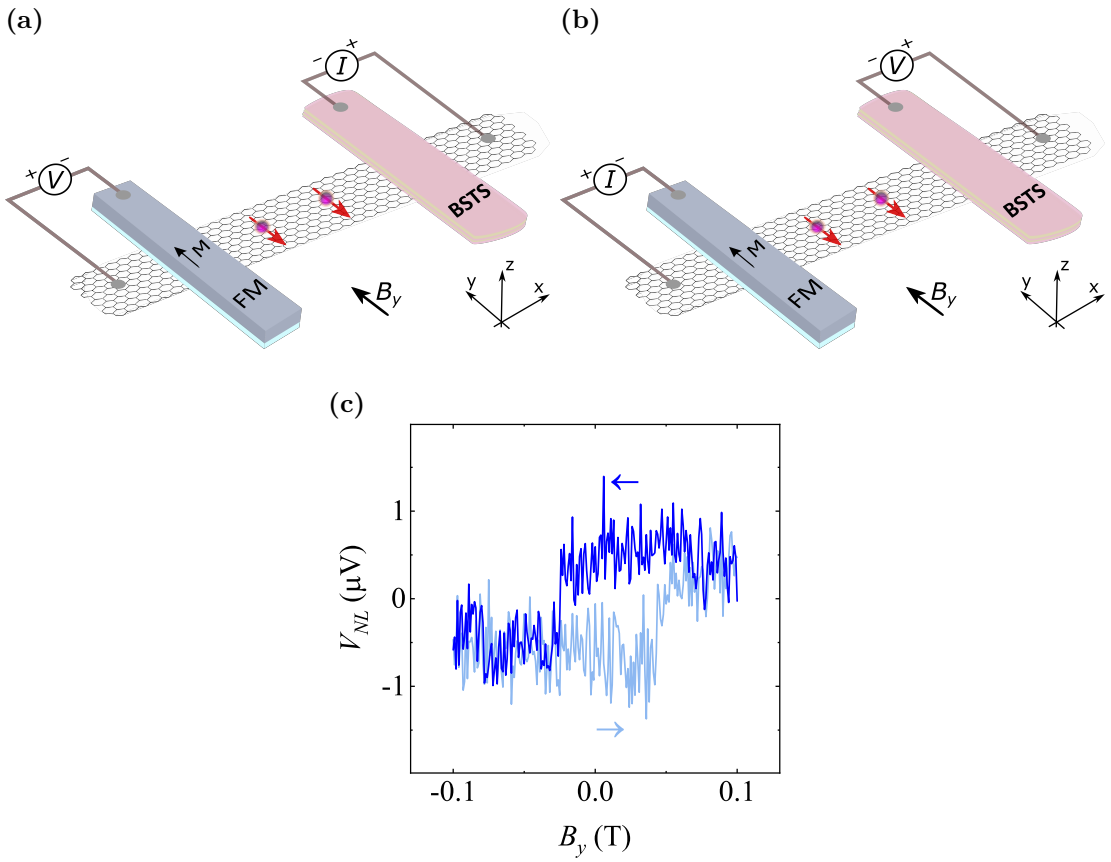

Figure 3.3: *Spin switch measurement.* **(a)** *Schematic of spin switch measurement with the TI as a spin injector.* **(b)** *Schematic of spin switch measurement with the TI as a spin detector.* **(c)** *An example of a signal from a spin switch measurement with the TI as a spin injector. The dark blue curve is for sweeping the external magnetic field from the $+y$ to the $-y$ direction and the light blue one is for sweeping from $-y$ to $+y$.*

Instead of using the TI as a spin current injector, it can also be used as a spin current detector. The setup for this type of measurement is viewed in Figure 3.3b. Here, a spin current is injected from the FM contact and subsequently absorbed by the TI, where it is converted into a charge current by the spin-to-charge conversion (SCC) of the TI and can then be detected as a non-local voltage between the nonmagnetic contact on top of the TI flake and the reference contact on the far right [28]. The obtained signal is an analogue to that of the measurement with the TI as a spin injector.

In addition to verifying the presence of spin transport between the injector and the detector, the obtained results from spin switch measurements also show that there is CSC and/or SCC in the TI flake (depending on whether the TI flake is used as a spin injector and/or a spin detector). The amplitude of the signal depends both on how much spin current that is transported between the electrodes and on the efficiency of the CSC or SCC. Furthermore, by adapting Equation (3.1), the polarisation of

the TI flake P_{TI} can be calculated from

$$\Delta R_{NL} = \frac{P_{FM} P_{TI} R_{\square} \lambda_s}{W_{Gr}} \exp\left(\frac{-L}{\lambda_s}\right). \tag{3.2}$$

3.2.3 Hanle spin precession

The electron spins in the spin valve and spin switch measurements do not precess since they are parallel or antiparallel to the external magnetic field, which is applied along the y axis [6]. In Hanle spin precession measurements, however, the external magnetic field is instead applied along the z axis, *i.e.* out of the graphene plane. This causes in-plane spin precession, *i.e.* the electron spins precess around the z axis as they propagate across the graphene channel [23]. Apart from the direction of the external magnetic field, the basic setup of a Hanle precession measurement is identical to that of a spin valve measurement, as seen in Figure 3.4a.

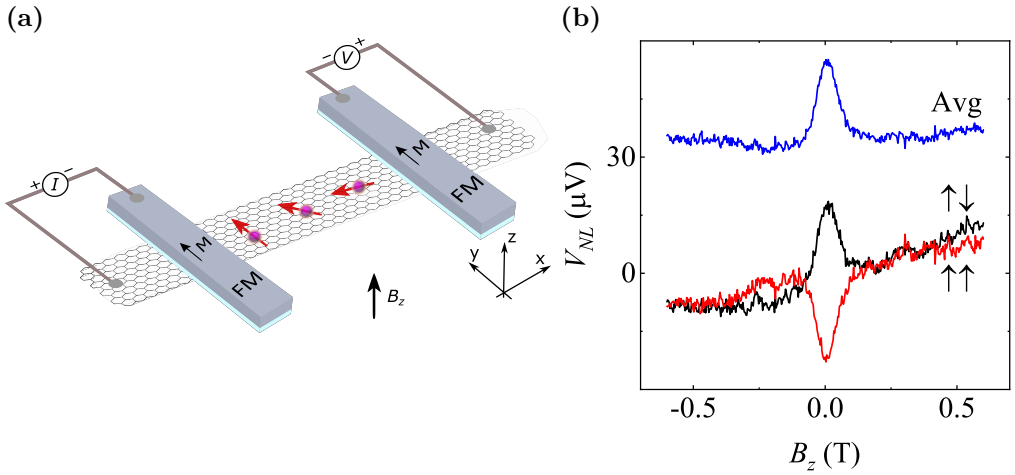

Figure 3.4: *Hanle spin precession measurement.* **(a)** *Hanle setup with two FM electrodes.* **(b)** *Non-local Hanle spin precession signals between two FM contacts with parallel (red curve) and antiparallel (black curve) electrode magnetisations. The blue curve is the averaged signal according to Equation* (3.3)*. The data are shifted vertically for clarity.*

As stated above, electrons can only enter a FM contact if their spins are aligned with the magnetisation of the contact. For Hanle spin precession measurements, this means that only the projection of the electrons' spin onto the detector electrode magnetisation direction will give rise to a measurement signal. At zero applied magnetic field, the obtained signal is typically the same for Hanle spin precession measurements as for spin valve: the spins travel between the contact without precessing and the non-local voltage is at a minimum [7] (see $B = 0$ for the red curve in Figure 3.4b, as compared to $B = 0$ in Figure 3.2b). However, when a nonzero magnetic field B_z is applied, precession causes the electron spins to arrive to the detector electrode with a finite angle to the contact magnetisation direction, resulting in a decreased signal amplitude [28]. Ideally, the non-local voltage signal would

oscillate for increased B_z as the spins precess around the z axis with increasing angular velocity. However, scattering causes the electrons to take different paths along the graphene channel and subsequently have different transit times, which in turn causes different electron spins to have different spin-to-contact angles when they reach the detector [18]. This dephasing, in addition to thermodynamical relaxation of the spin accumulation into the equilibrium state, results in a rapid decay of the Hanle spin precession signal for increasing magnetic field [18], as seen in Figure 3.4b.

In the discussion about Hanle spin precession so far, it has been assumed that the two FM contacts have parallel magnetisation directions. If the contacts instead have antiparallel magnetisation directions, the graph for the non-local voltage will be flipped upside down [6]. To exemplify: while the parallel configuration (red curve) has a minimum at $B = 0$ in Figure 3.4b, the antiparallel configuration (black curve) instead has a maximum at $B = 0$. Identically to the case of the plateaus in spin valve measurements, this happens because the spins' polarisation is antiparallel with the detector's magnetisation direction. Since any signal background that is caused by charge effects will be unaffected by the magnetisations of the electrodes, while there is a sign change for the spin signal, the signal background can be eliminated by subtracting the signals from the parallel and the antiparallel configurations from each other [87, 90], according to

$$V_{NL}{}^{average} = \frac{V_{NL}{}^{\uparrow\downarrow} - V_{NL}{}^{\uparrow\uparrow}}{2}, \tag{3.3}$$

where $V_{NL}{}^{\uparrow\downarrow}$ and $V_{NL}{}^{\uparrow\uparrow}$ are the obtained non-local voltage signals for the configurations with antiparallel and parallel contact magnetisation directions, respectively, and $V_{NL}{}^{average}$ is the average between the spin signals with eliminated background. This is examplified in Figure 3.4b, where the average (blue curve) has a much smaller signal background than the corresponding raw data (red and black curves).

Hanle spin precession measurements can also be made with one of the FM electrodes exchanged for a TI flake [73]. Just as in spin switch measurements, the CSC (or SCC) of the TI is utilised to inject (or detect) a spin current. Since the 'polarisation' of the CSC and the SCC is independent of the external magnetic field direction, the non-local voltage has a minimum or a maximum depending only on the magnetisation direction of the FM contact. Instead of denoting the configurations as parallel or antiparallel magnetisations, the configurations are therefore referred to as positive magnetisation ($M+$) or negative magnetisation ($M-$) for signals with a maximum or a minimum, respectively. Apart from this, Hanle spin precession for a setup with one FM contact and a TI flake works identically to for one with two FM contacts.

Something that is not inherent to Hanle spin precession with a TI spin injector or detector, but may be more commonly encountered for these setups, is more or less asymmetric non-local voltage signals. The reason for this is that the exfoliated TI flakes are harder to align than the lithographically patterned FM contacts. The asymmetry is namely caused by a misalignment between the injected spins and the detector [90]. If the polarisation of a spin current initially is parallel to the FM detector electrode and the external magnetic field causes precession by $\pi/2$, the

detected spin polarisation will be perpendicular to the detector and the resulting signal will be zero, no matter which direction the spins precess in. If, however, the polarisation of the spin current instead initially is perpendicular to the detector, the spins will precess to be either parallel or antiparallel with the detector magnetisation and the resulting signal will be positive or negative depending on the direction of the precession [90]. This dependence on the spin precession direction causes the obtained signal to be antisymmetric when the injected spins are polarised perpendicular to the detector, as opposed to the symmetric signal that is obtained when the injected spin polarisation is parallel with the detector [91]. Examples of symmetric and antisymmetric Hanle spin precession signals are presented in Figures 3.5a and 3.5b, respectively, as well as in Appendix B.

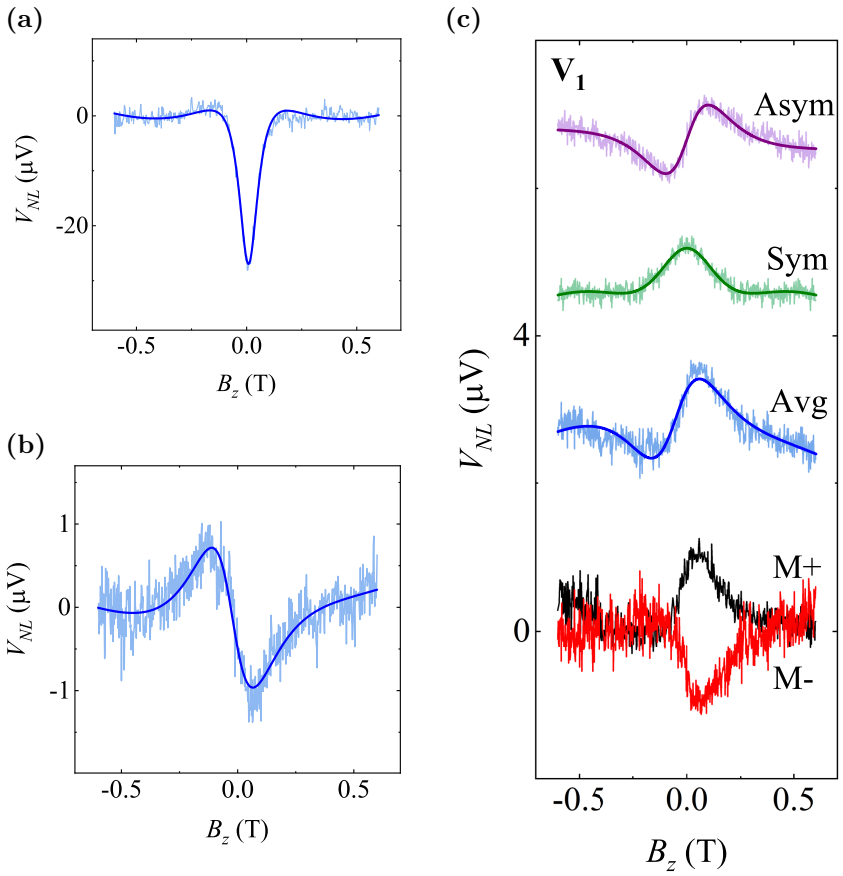

Figure 3.5: *Asymmetry in signals from Hanle spin precession measurements.* **(a)** *A symmetric signal from a measurement across pristine graphene between two FM contacts (light blue) and a corresponding symmetric fit (dark blue).* **(b)** *An antisymmetric signal from a measurement with a TI as spin injector and a FM contact as detector (light blue) and a corresponding antisymmetric fit (dark blue).* **(c)** *Asymmetric signals from a measurement with a TI as spin injector and a FM contact as detector (black and red) with the average signal (light blue) and the symmetric (light green) and antisymmetric (violet) components of the averaged signal. The dark blue, dark green and purple curves are symmetric and antisymmetric fits of the signals. Linear backgrounds have been subtracted from the measured data.*

When the polarisation of the injected spin current is neither parallel nor perpendicular to the detector, the non-local voltage signal has both symmetric and antisymmetric components [7]. These can be deconvoluted mathematically using

$$\begin{cases} {V_{NL}}^{\parallel}(B) = \dfrac{V_{NL}(B) + V_{NL}(-B)}{2} & \text{(3.4a)} \\ {V_{NL}}^{\perp}(B) = \dfrac{V_{NL}(B) - V_{NL}(-B)}{2}, & \text{(3.4b)} \end{cases}$$

where V_{NL} is the non-local voltage signal and ${V_{NL}}^{\parallel}$ and ${V_{NL}}^{\perp}$ are its symmetric and antisymmetric components, respectively [7, 90]. Figure 3.5c shows an example of two asymmetric Hanle spin precession signals with opposite magnetisation, the average signal (calculated from Equation (3.3)) and the symmetric and antisymmetric components of the average signal (calculated from Equations (3.4)). By comparing the relative contribution of the symmetric and antisymmetric components, the angle φ between the polarisation of the injected spin current and the detector contact magnetisation can be calculated according to

$$\varphi = \tan^{-1}\left(\frac{\Delta {V_{NL}}^{\perp}}{\Delta {V_{NL}}^{\parallel}}\right), \tag{3.5}$$

where $\Delta {V_{NL}}^{\parallel}$ and $\Delta {V_{NL}}^{\perp}$ are the amplitudes of the symmetric and the antisymmetric components, respectively [7].

The obtained non-local voltage signal from Hanle spin precession measurements can be fitted to the equations

$$\begin{cases} {V_{NL}}^{\parallel} \propto \displaystyle\int_0^{\infty} \frac{1}{\sqrt{4D_s t}} \exp\left(-\frac{L^2}{4D_s t}\right) \cos(\omega_L t) \exp\left(-\frac{t}{\tau_s}\right) \mathrm{d}t & \text{(3.6a)} \\ {V_{NL}}^{\perp} \propto \displaystyle\int_0^{\infty} \frac{1}{\sqrt{4D_s t}} \exp\left(-\frac{L^2}{4D_s t}\right) \sin(\omega_L t) \exp\left(-\frac{t}{\tau_s}\right) \mathrm{d}t & \text{(3.6b)} \end{cases}$$

for the symmetric and the antisymmetric components, respectively [6, 7, 21, 73, 88, 92, 93]. Here, D_s is the spin diffusion coefficient, τ_s is the spin lifetime, L is the channel length and $\omega_L = \frac{g\mu_B}{\hbar} B_z$ is the Larmor spin precession frequency, where g is the Landé g-factor (which is the ratio between the magnetic moment and the angular momentum of self-rotation of an electron [44]) and μ_B is the Bohr magneton [6, 7, 21, 73, 88, 92, 93]. The parts of Equations (3.6) that contain D_s represent spin diffusion, the part that contains τ_s represents spin relaxation and the part that contains ω_L represents spin precession [6]. The impact of the different parameters are investigated further in Appendix B. Finally, an integration is performed over all possible transit times between the injector and the detector electrodes [6]. By fitting Equations (3.6) to an obtained signal, values for the spin lifetime and the spin diffusion coefficient can be extracted. From these values, the spin diffusion length $\lambda_s = \sqrt{D_s \tau_s}$ can also be calculated [73]. Examples of fittings are shown for the averaged non-local voltage signal as well as its symmetric and antisymmetric components in Figure 3.5c. It should be pointed out that Equations (3.6a) and (3.6b) are purely symmetric and antisymmetric functions, respectively. This is why

the fittings for the symmetric and antisymmetric components are visibly better than the fitting of the averaged signal, which is fitted with the antisymmetric Equation (3.6b) even though it contains both symmetric and antisymmetric components.

By using Equations (3.6), two main assumptions are being made, which should be kept in mind. The first one is that the contact resistance is much larger than the spin resistance of the graphene, and if this is not fulfilled, a more complex analysis is required to take contact-induced spin relaxation into account [6]. This is experimentally confirmed to be true for the devices in this thesis work. The second assumption is that $g = 2$. This is generally true (and also in the case of this thesis work), but *e.g.* the presence of paramagnetic moments can increase the value of g, which would make analysis of Hanle spin precession measurements significantly more difficult [6]. Hence, the use of Equations (3.6) in this thesis work is justified.

4

Non-Local Electronic Detection of Spin Transport in Graphene at Room Temperature

Graphene is an excellent material for efficient and long-distance spin transport, thanks to its high carrier mobility and weak intrinsic spin-orbit coupling. This, combined with the possibility to induce properties in graphene through proximity effects, has made graphene the primary spin transport medium for spintronics applications. Here, the spin transport properties of graphene in a van der Waals heterostructure with the topological insulator $Bi_{1.5}Sb_{0.5}Te_{1.7}Se_{1.3}$ are examined at room temperature and compared to the spin transport properties of pristine graphene. Non-local spin valve and Hanle spin precession measurements show that the spin transport in graphene is sufficiently efficient and that the proximity-induced impact from the topological insulator is likely to be negligible. These findings will later be used in the analysis of the results from the charge-spin interconversion experiments in Chapter 5.

4.1 Spin valve measurements and bias current dependence

Since the discovery and characterisation of graphene by Geim and Novoselov *et al.* [94, 95], the material has attracted vast attention due to its unique and extraordinary properties, and even gained its discoverers a Nobel Prize in Physics [96]. In the field of spintronics, graphene is extremely useful for spin transport, thanks to the long spin lifetimes and spin diffusion lengths that arise from the material's weak spin-orbit coupling [6, 10, 18, 97]. Furthermore, the ability to tune the properties of graphene through proximity effects adds an extra layer of versatility [23, 98, 99]. In this thesis work, chemical vapour deposition (CVD) graphene and mechanically exfoliated $Bi_{1.5}Sb_{0.5}Te_{1.7}Se_{1.3}$ (BSTS) are stacked in van der Waals (vdW) heterostructures, in hope of combining the transport properties of graphene with the spin-momentum locking of the topological insulator BSTS.

The spin transport measurements in graphene were performed for two parts of the

device: heterostructure graphene, where a flake of BSTS was put on top of the graphene channel in a vdW heterostructure (see Figure 4.1a), and pristine graphene, outside of the vdW heterostructure (see Figure 4.1b). The first goal of the experiments was to simply detect spin transport through the graphene channel, both across the heterostructure and across pristine graphene. The second goal was to investigate if the vdW heterostructure made an impact on the spin transport and the transport properties of graphene, in order to better understand the results from the charge-spin interconversion experiments in Chapter 5.

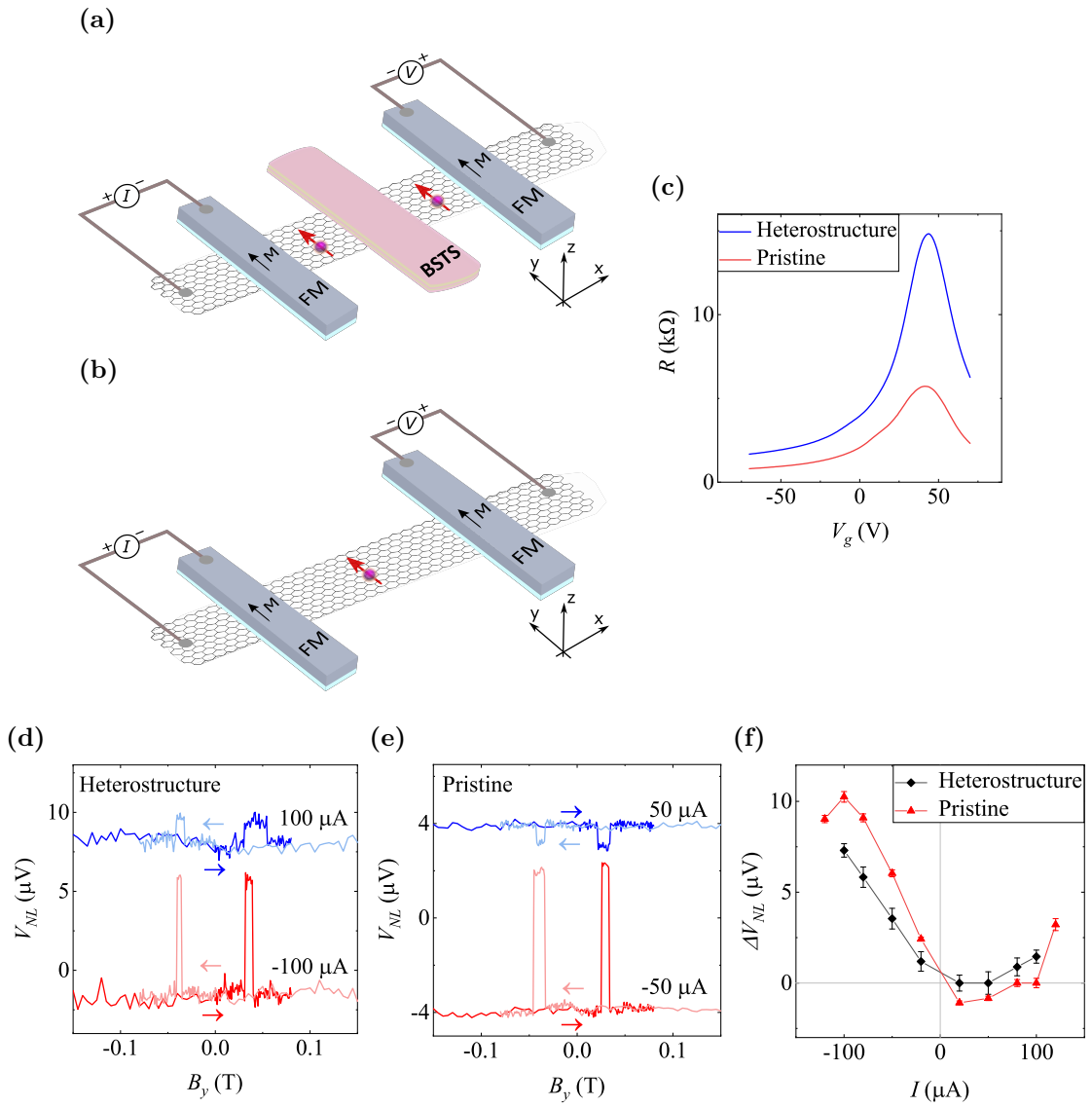

Figure 4.1: *Spin valve measurements.* **(a)** *Schematic of the measurement setup for the graphene channel in the vdW heterostructure.* **(b)** *Schematic of the measurement setup for the graphene channel with pristine graphene, outside of the vdW heterostructure.* **(c)** *Local resistance measured when passing a* $1\,\mu$A *current through the graphene channel for the heterostructure and pristine graphene, respectively, as a function of gate voltage. The resistance maxima at* $V_g = 43\,$V *corresponds to the graphene Dirac points.* **(d)** *Spin valve non-local signals across the heterostructure for positive and negative bias currents* ($I = \pm 100\,\mu$A)*. The measurements were performed for* $V_g = -60\,$V*. The data are shifted vertically for clarity.* **(e)** *Spin valve non-local signals across pristine graphene for positive and negative bias currents* ($I = \pm 50\,\mu$A)*. The measurements were performed for* $V_g = -70\,$V*. The data are shifted vertically for clarity.* **(f)** *The spin valve signal amplitude for the heterostructure and pristine graphene, respectively, as a function of bias current.*

First, the gate modulation of the local resistance across the graphene was investigated. This was done through measuring the local resistance $R = V/I$ while passing

a $1\,\mu$A current across the graphene channel. The obtained results are presented in Figure 4.1c. Both the heterostructure graphene and the pristine graphene show a maximum at approximately $V_g = 43\,\text{V}$, which corresponds to the graphene Dirac point. The requirement of a positive gate voltage for reaching the Dirac point means that the graphene is hole doped by the SiO_2 wafer [100, 101]. The very small shift in gate voltage between the heterostructure and the pristine graphene is within the error range of the equipment, and it can thus be concluded that the BSTS flake does not cause any additional doping of the graphene channel. The difference in amplitude between the two curves comes from the difference in channel length: $6.7\,\mu$m for the heterostructure graphene *vs* $2.5\,\mu$m for the pristine graphene. The significantly longer channel for the heterostructure graphene naturally gives rise to a higher resistance.

By extracting data from Figure 4.1c, the mobility of the charge carrier could be calculated [102] to $\mu_{HS} = 1.2 \cdot 10^3\,\text{cm}^2/\text{Vs}$ for the heterostructure graphene and $\mu_{pristine} = 1.0 \cdot 10^3\,\text{cm}^2/\text{Vs}$ for the pristine graphene. These values are similar to reported mobilities of graphene channels in similar heterostructure devices [28, 67, 73, 92].

Next, spin valve measurements were performed for different bias currents. The bias dependence of the signal amplitude is shown in Figure 4.1f, with illustrative examples of the spin valve signals in Figures 4.1d and 4.1e for heterostructure graphene and pristine graphene, respectively. It is expected that the amplitude will increase for larger bias currents, since a larger charge current enables the polarisation of a larger spin current. However, the V-shaped curves are shifted towards more positive bias currents, and the pristine graphene even shows negative spin valve amplitudes (as clearly seen in Figure 4.1e). This behaviour has been reported previously for similar devices, and is thought to happen because of local hot-electron effects across the FM contact tunnel junctions at higher positive bias currents and/or because of the complex electronic structure of the FM-graphene hybrid interfaces [103].

Using the amplitude of the spin valve signals and spin transport parameters that were extracted from Hanle spin precession signals (see below), the polarisation of the FM contacts was calculated from Equation (3.1) to be 3.9%. The calculation was performed for pristine graphene in order to avoid any influence of possible spin absorption of the TI flake in the heterostructure. The obtained value falls into the range of reported contact polarisations for FM contacts where the tunnel barrier towards graphene has pinholes ($2 - 18\%$) [86, 104, 105]. It is slightly higher than the reported polarisation of transparent contacts (1%) [106] and an order of magnitude lower than that of contacts with pinhole-free tunnel barriers ($26 - 30\%$) [88]. This indicates that the tunnel barriers in this thesis work have pinholes, which was already suspected from the device fabrication (see Appendix A). Tunnel barriers without pinholes would probably have enabled a higher contact polarisation and thus higher spin signal amplitudes, but the obtained contact polarisation is evidently high enough to give clear spin signals, which is sufficient for the scope of this work.

4.2 Hanle spin precession measurements and gate voltage dependence

Following the spin valve measurements, Hanle spin precession measurements were performed. The observed modulation of the spin signal with out-of-plane magnetic field strength (examples for heterostructure and pristine graphene are shown in Figures 4.2a and 4.2b, respectively) is, together with the spin valve signals, very strong evidence of spin transport across the graphene channels. It can be seen that the Hanle curve for pristine graphene is significantly broader than the one for heterostructure graphene. This happens because of the difference in channel length, since a longer channel typically results in a thinner Hanle spin precession curve.

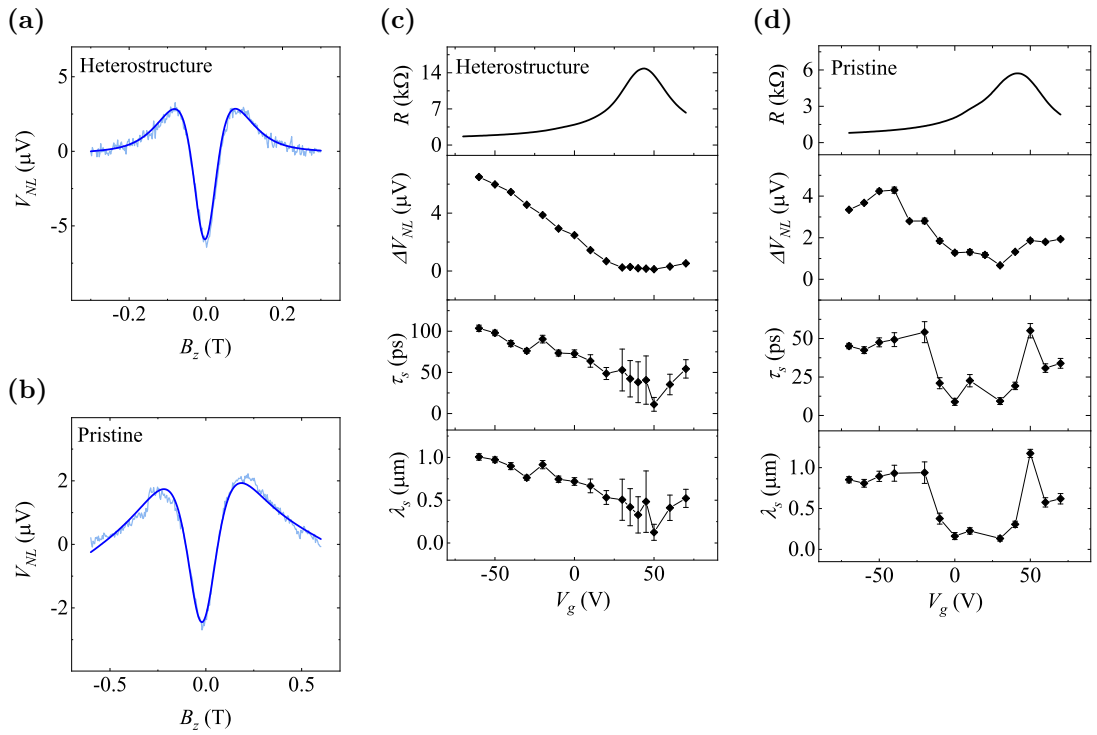

Figure 4.2: *Hanle spin precession measurements.* **(a)** *Hanle spin precession non-local signal (light blue) for the graphene channel across the heterostructure, as well as a symmetric fit (dark blue). The measurements were performed for* $I = 150\,\mu$A *and* $V_g = -60\,$V*. A linear background has been removed.* **(b)** *Hanle spin precession non-local signal (light blue) for the pristine graphene channel, as well as a symmetric fit (dark blue). The measurements were performed for* $I = -100\,\mu$A *and* $V_g = -70\,$V*. A linear background has been removed.* **(c)** *Top panel: Local voltage measured when passing a* $1\,\mu$A *current through the graphene channel across the heterostructure as a function of gate voltage. Three bottom panels: The peak-to-peak amplitude of the measured Hanle signals as well as spin lifetimes and spin diffusion lengths, extracted from symmetric fits of the Hanle signals, as functions of gate voltage. The measurements were performed for* $I = 150\,\mu$A*.* **(d)** *Top panel: Local voltage measured when passing a* $1\,\mu$A *current through the pristine graphene channel as a function of gate voltage. Three bottom panels: The peak-to-peak amplitude of the measured Hanle signals as well as spin lifetimes and spin diffusion lengths, extracted from symmetric fits of the Hanle signals, as functions of gate voltage. The measurements were performed for* $I = -100\,\mu$A*.*

The gate voltage dependence of the signal amplitude, as well as of the spin lifetime and the spin diffusion length, is presented in Figure 4.2c for heterostructure graphene and in Figure 4.2d for pristine graphene. The values of the spin transport parameters were extracted from fits of the measured Hanle spin precession signals using Equation (3.6a). Both the heterostructure and the pristine graphene have a gate dependence where the Hanle signal amplitude decreases closer to the graphene Dirac point. The spin valve amplitudes have a similar gate dependence, as shown in Appendix C. This is most likely because of a conductivity mismatch between the graphene channel and

the FM electrode. Since the increased resistivity of the graphene around the Dirac point is significantly higher than that of the metallic contact, injected spins are more likely to diffuse back into the injector electrode, rather than propagating along the graphene channel [88, 97, 107]. A lower injection rate leads to a smaller spin current and, subsequently, a lower spin signal amplitude.

Farther away from the graphene Dirac point, there is some difference between the heterostructure graphene and the pristine graphene. The former has a linear gate dependence while the latter seems to saturate around $V_g = -50\,\mathrm{V}$. This could be because of a difference in conductivity mismatch between different contacts that are being used for the measurements. It has been predicted by calculations and confirmed experimentally that transparent contacts give rise to a V-shaped gate dependence of the spin signal amplitudes, while tunnel barriers with pinholes cause the amplitudes to saturate for larger gate voltages [88]. However, all FM contacts in this thesis work were fabricated with an insulating layer of TiO_2, so none of them should be completely transparent. Still, it is possible that the amount of pinholes is larger for some contacts, which would give them a more transparent behaviour. Either way, further investigations with more devices would be necessary in order to draw any solid conclusions on the matter.

The spin lifetime and the spin diffusion length mainly follow the behaviour of the Hanle signal amplitude, for both types of graphene. The decrease of the spin parameters near the Dirac point can hence be explained as a consequence of the lack of spin signal, considering that the values of the parameters come from fits of the Hanle curves. This also explains the appearance of noticeably larger error bars around $V_g = 40\,\mathrm{V}$ (where small signal amplitudes causes a low signal-to-noise ratio) for the heterostructure graphene.

Finally, it should be mentioned that, since the distance between the injector and the detector electrodes is relatively short, the obtained values of spin lifetime and spin diffusion length can be seen as a lower bound of their actual values [7]. This is especially true for the pristine graphene, since its channel length is less than half as short as the heterostructure graphene channel length.

4.3 Spin lifetime anisotropy

The last set of graphene transport measurements of this work were performed with different out-of-plane angles, β, between the graphene and the oblique external magnetic field B_β. In addition to this, the sign of the magnetic field was restricted so that the magnetisation of the FM contacts did not switch during the B_β sweeps. With this setup, the spin transport across the vdW heterostructure was measured like previously, giving the results in Figure 4.3a. Because of the oblique external magnetic field (for $0° < \beta < 90°$), the injected spins precess partly out-of-plane as they propagate across the graphene channel in the heterostructure. This makes the spin polarisation sensitive to both the in-plane spin lifetime $\tau_s^{\parallel}$ and the out-of-plane spin lifetime $\tau_s^{\perp}$ [108], as opposed to the spin valve and Hanle spin precession mea-

surements, where the spin polarisation is only sensitive to $\tau_s^{\parallel}$. For larger magnetic fields (the yellow area in Figure 4.3a), the polarised spins will dephase, and only the spin component that is parallel to B_β will survive [109]. By comparing the non-local voltage that is detected for this case, ΔV_{NL}^{β}, to the non-local voltage that is detected for zero applied field, $\Delta V_{NL}(B = 0)$, the spin lifetime anisotropy $\zeta = \tau_s^{\perp}/\tau_s^{\parallel}$ can be calculated using the Bloch-diffusion model [108].

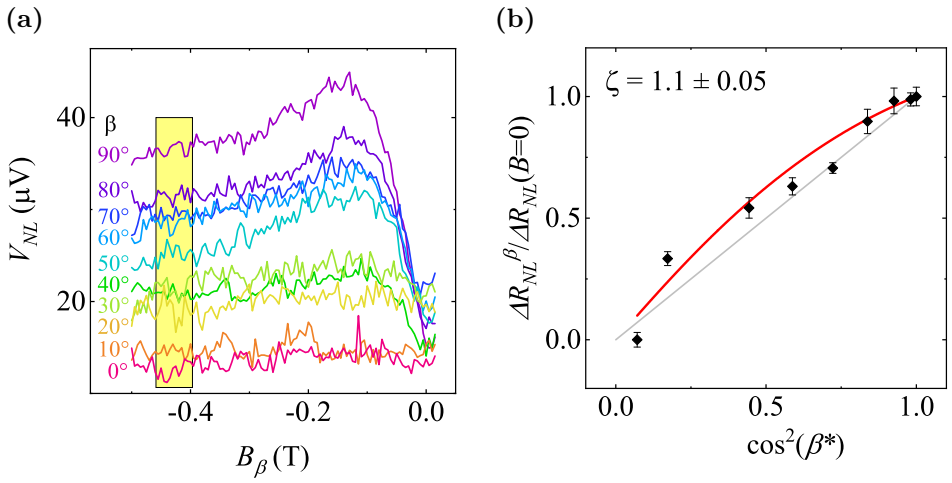

Figure 4.3: *Spin lifetime anisotropy measurements.* **(a)** *Spin precession measurements across the graphene channel in the vdW heterostructure with an oblique external magnetic field applied at an angle β against the graphene plane. The measurements were performed for $I = -200\,\mu$A and $V_g = -70\,$V.* **(b)** *Visualisation of the spin lifetime anisotropy with black dots extracted from* (a)*. The red curve is a fit of the extracted data and the grey line represents an isotropic spin lifetime.*

In Figure 4.3b, the ratio between ΔV_{NL}^{β} and $\Delta V_{NL}(B = 0)$ is plotted against $\cos^2(\beta^*)$, where β^* is the angle β with a small correction γ to account for the small tilting of the FM contact magnetisation that is caused by the applied magnetic field [89]. This is a way to visualise the spin lifetime anisotropy results that were extracted from Figure 4.3a. For completely isotropic spin lifetimes (*i.e.* $\tau_s^{\parallel} = \tau_s^{\perp}$), the data points will follow the grey $y = x$ line [89]. For cases with $\zeta > 1$ and $\zeta < 1$, the data points will be above and below this line, respectively [89].

The fit of the data points in Figure 4.3b (red curve) indicates that the spin lifetime is slightly anisotropic with spin lifetime anisotropy of $\zeta = 1.1 \pm 0.05$, but there are three sources of error that cause some uncertainty. The first uncertainty comes from the graphene channel being shorter than what is usual for this type of experiment. A longer graphene channel makes the Hanle curves thinner with saturation of the spin dephasing at a weaker external magnetic field. Because of this, ΔV_{NL}^{β} is normally extracted in the range of $B_\beta = 0.1 - 0.2\,$T [89, 108, 109], which is to be compared to $|B_\beta| \gtrsim 0.4\,$T in this work. The application of a significantly stronger magnetic field may have caused some impact on the obtained results.

The second possible source of error is the noise of the measured signals in Figure 4.3a. While the curves are not extremely noisy, there is undeniably some noise that could influence on the extracted values of ΔV_{NL}^{β}. Better tunnel barriers between the graphene and the FM contacts with less pinholes and higher interface resistance would probably have helped decreasing the noise, but that is beyond the scope of this thesis work. Finally, the third cause of uncertainty is that the external magnetic field was aligned manually for each of the measurements, and the values of β are therefore likely to be somewhat inexact due to human error.

Considering the uncertainty due to these three possible sources of error and that the obtained value of the spin lifetime anisotropy is already close to 1, the conclusion is that the spin lifetime anisotropy is in the range of unity. There might be some anisotropy, but the spin lifetime might also be completely isotropic. This means that proximity effects from the BSTS flake have a negligible impact on the spin lifetime in the graphene channel, since the proximity effects would otherwise have caused the spin lifetime to be clearly anisotropic [109]. This stands in agreement with the results in Figure 4.1f, where the spin signal amplitude is very similar for heterostructure graphene and pristine graphene. The lack of spin absorption of the BSTS flake (which would have caused a lowered signal amplitude) indicates that there is not much interaction between the graphene and the TI. It should be noted, however, that the spin lifetime anisotropy measurements were not performed on the same device as the charge-spin interconversion experiments in Chapter 5, and ζ has been known to have large device-to-device variations. Nevertheless, the results in Figures 4.3 and 4.1f give some indication that the proximity effects from the BSTS on the graphene channel are weak for these devices.

5

Non-Local Electronic Detection of Charge-Spin Interconversion in a Topological Insulator at Room Temperature

Topological insulators are promising candidates for spin generation and detection in all-electrical spintronics applications, thanks to their strong spin-orbit coupling and non-trivial spin-momentum locking of their topological surface states. Charge-spin interconversion has previously been reported using spin potentiometric measurement methods. However, reliable non-local measurements have so far been limited to cryogenic temperatures. Here, we report non-local detection of charge-spin interconversion in the topological insulator $Bi_{1.5}Sb_{0.5}Te_{1.7}Se_{1.3}$ at room temperature using a van der Waals heterostructure with graphene in a spin valve device. The observation of both spin switch and Hanle spin precession signals in the non-local device and detailed bias and gate dependent measurements prove the robustness of the charge-spin interconversion effects in topological insulators at room temperature. These findings demonstrate the possibility of using topological insulators to make all-electrical room-temperature spintronics devices for energy-efficient next-generation computing components.

5.1 Charge-to-spin conversion

The unique electronic band structure of topological insulators (TIs) has attracted much attention in recent years [17, 27, 110]. Their strong spin-orbit coupling (SOC) and the spin-momentum locking (SML) of their topological surface states enable charge-to-spin and spin-to-charge conversion (CSC and SCC, respectively) for fast and energy-efficient computing through spintronics applications. However, a weak SOC is necessary for efficient spin transport. By stacking TIs and graphene in van der Waals (vdW) heterostructures, the SML of the TI can be combined with the excellent spin transport properties of graphene. This is done in this work with chemical vapour deposition (CVD) graphene and mechanically exfoliated $Bi_{1.5}Sb_{0.5}Te_{1.7}Se_{1.3}$ (BSTS). The finished device, with non-magnetic and ferromagnetic (FM) contacts,

is shown in the scanning electron microscope (SEM) image in Figure 5.1c.

The CSC experiments were performed for measurement geometries such as the one in Figure 5.1a. A non-polarised DC charge current was injected from one of the nonmagnetic contacts on top of the BSTS flake, and the non-local voltage was measured between a FM electrode across the graphene channel and a nonmagnetic reference contact. Due to the strong SOC of BSTS, the charge current is partially converted into a polarised spin current. This can happen through three different CSC mechanisms, as explained in Section 2.2. In the spin Hall effect (SHE), the SOC causes electrons to be scattered in opposite directions depending on their spin polarisation, which is visualised in the left of Figure 5.1b, and this gives rise to a transverse spin current [16]. CSC can also originate either from the Rashba-Edelstein effect (REE) of the bulk states or from the topological spin-momentum locking (TSML) of the surface states [64]. The right of Figure 5.1b shows the band structure of a TI, with spin-split conduction and valence bulk bands due to Rashba SOC and metallic topological surface states. Depending on the position of the Fermi level, the Fermi surface has either one or two helical windings in its spin texture, which will be offset from the equilibrium position by the additional electron momentum that is caused by an applied electric field [47, 63, 74]. Furthermore, both the SHE and the REE can appear not only in the bulk states of the TI, but also in the graphene through proximity effects [25, 47]. All five of these CSC origins can lead to a spin accumulation, and while the charge current flows through the closed loop between source and drain, a pure spin current diffuses in both directions along the graphene channel and can thus be detected as a non-local voltage drop.

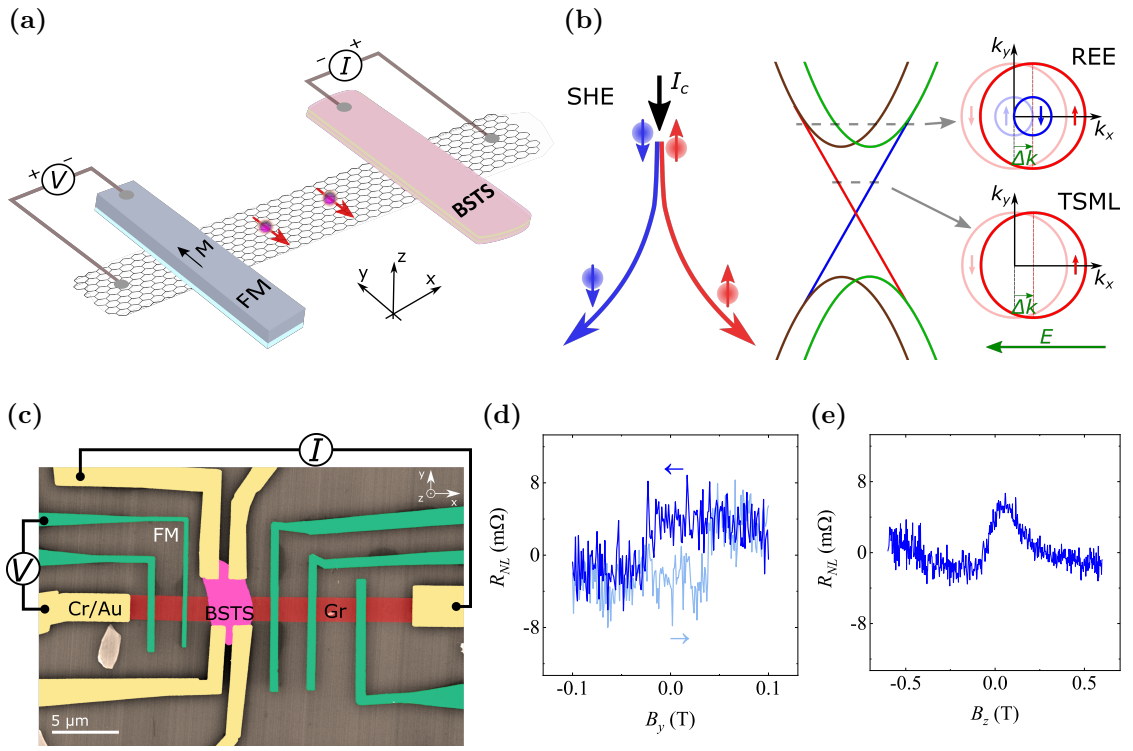

Figure 5.1: *Graphene/TI heterostructure device for non-local detection of CSC in the TI.* **(a)** *Schematic of the device and the measurement geometry for an experiment with spin injection from the TI flake. The charge current in the TI flake is expected to be converted into a polarised spin current, which is then injected into the graphene channel and subsequently detected non-locally using a FM electrode.* **(b)** *Schematics of the possible CSC mechanisms in the TI. In the SHE (left), spins are deflected in different directions based on their spins and a transverse spin current is formed. In the REE and the TSML (right), the SML of the electronic spin texture at the Fermi surface gives rise to a spin accumulation when an electric field is applied.* **(c)** *Coloured SEM image of the device with drawn schematics showing the same measurement setup as in* (a)*. The major component of the device is the graphene/BSTS heterostructure, and nonmagnetic and FM contacts are used for injection and detection of charge and spin currents.* **(d)** *Spin switch non-local signal for in-plane B_y magnetic field sweeps. The measurement was performed for a bias current of $I = 150\,\mu$A and a gate voltage of $V_g = -70$ V.* **(e)** *Hanle spin precession non-local signal for out-of-plane B_z magnetic field sweeps. The measurements were performed for a bias current of $I = 150\,\mu$A and a gate voltage of $V_g = -70$ V. A linear background has been subtracted from the measured data.*

First, spin switch measurements were performed by measuring the non-local voltage while sweeping an external magnetic field along the y axis (which is the easy axis of the FM electrodes). Since the polarisation of the spin current is already aligned with the magnetic field, no spin precession takes place, but when the magnetic field is strong enough, the magnetisation direction of the FM contact will switch between the $+y$ and $-y$ directions [85]. The polarised electrons in the graphene channel will be significantly less prone to be absorbed by the FM contact when their spin direction and the contact magnetisation direction are antiparallel to each other than when

they are parallel, which results in a sharp jump in non-local resistance ($R_{nl} = V_{nl}/I$) when the FM contact magnetisation direction is switched by the external magnetic field [6]. One such signal with a pronounced hysteresis for the forward and backward sweep is shown in Figure 5.1d. This kind of signal will only appear for a polarised spin current and this is therefore a clear indication of CSC in the BSTS flake.

Second, Hanle spin precession measurements were conducted with the external magnetic field being swept along the out-of-plane z axis. This causes the spins to precess in-plane and they therefore arrive to the FM detector electrode with a finite angle to the contact magnetisation direction. Since the non-local resistance depends on the projection of the spin current polarisation onto the contact magnetisation direction, this misalignment results in a decreased magnitude of the detected non-local resistance for increased out-of-plane magnetisation [28], as seen in the Hanle signal in Figure 5.1e. The dependence of the non-local resistance on the out-of-plane magnetic field is an additional confirmation of a polarised spin current being injected into the graphene channel from the TI due to CSC.

Using the spin valve signal amplitude, spin transport parameters extracted from the Hanle signals and the contact polarisation from Chapter 4, the spin polarisation of the BSTS flake was calculated to 0.1% from Equation (3.2). This is an order of magnitude lower than REE conversion efficiencies in literature, but comparable to previously reported spin Hall angles (see Sections 2.2.2 and 2.2.1, respectively). The charge-spin interconversion efficiency of this device is, in other words, at least decent, compared to the state of the art. Furthermore, this work is a proof-of-concept rather than an attempt to optimise the device performance. It is therefore likely that a fine-tuned fabrication process will increase the charge-spin interconversion further.

The Hanle signals are studied further in Figure 5.2a. Prior to sweeping the magnetic field out-of-plane, the magnetisation direction of the FM detector electrode was set by temporarily applying an in-plane magnetic field in the $+y$ or $-y$ direction. Depending on the contact magnetisation direction, the Hanle signal has either a minimum or a maximum around $B_z = 0$, similarly to the spin switch signal, which further supports the existence of a spin current. The two curves for opposite contact magnetisation were first averaged using Equation (3.3) and the symmetric and the antisymmetric components of the average signal were then deconvoluted using Equations (3.4). The average signal and its two components were then fitted by Equations (3.6). The relative contribution of the symmetric and the antisymmetric components depends on the angle between the polarisation of the spin current that is injected from the BSTS flake to the graphene and the magnetisation direction of the FM detector contact [7, 90]. By extracting the amplitudes of the signal components, this angle could be determined to $\varphi = 67 \pm 1°$ from Equation (3.5). This result is not surprising, considering that the charge current is likely to pass diagonally through the BSTS flake and the graphene/TI interface (see *e.g.* Figure 5.2b), and will thereby give rise to a diagonal spin polarisation (since the spins are polarised perpendicularly to the charge current path).

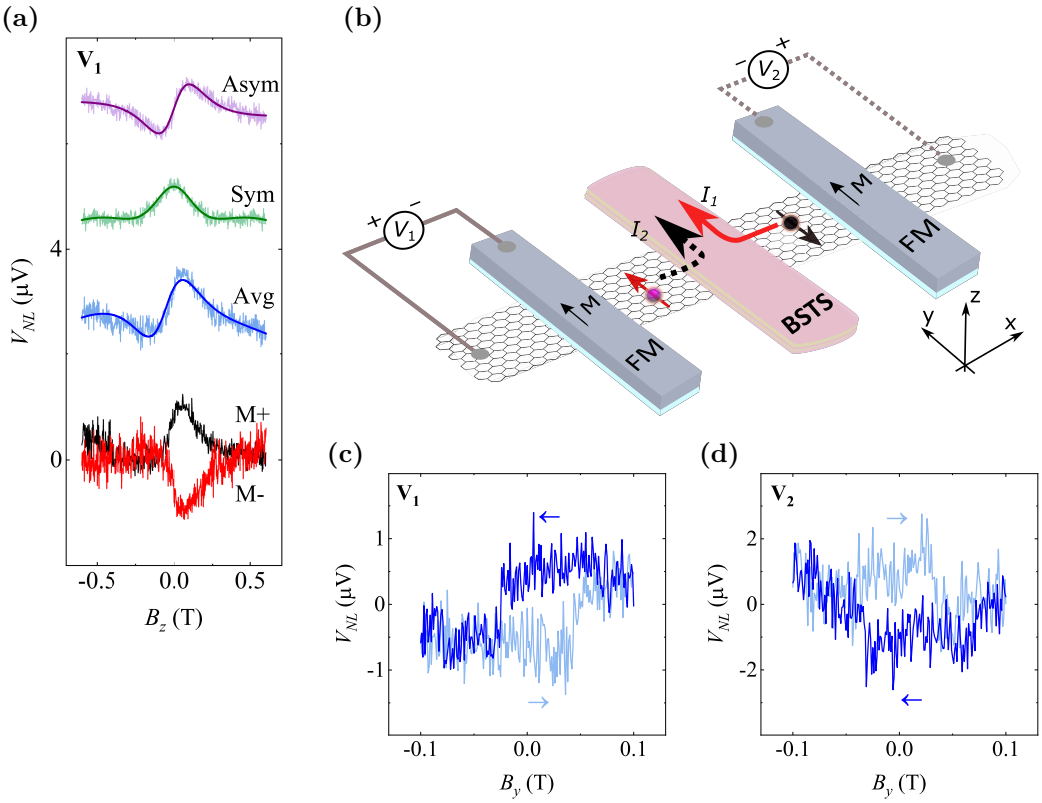

Figure 5.2: *Measurement geometry dependence of the CSC signal.* **(a)** *Hanle spin precession non-local signals for measurement geometry 1 in* (b) *with FM contact magnetisation along the $+y$ (black curve) and the $-y$ direction (red curve), respectively, as well as the averaged signal (light blue curve) and the symmetric (light green curve) and the anti-symmetric (violet curve) components of the averaged signal. The dark blue, dark green and purple curves are fits of the respective signals. The measurements were performed for a bias current of $I = 150\,\mu$A and a gate voltage of $V_g = -70\,$V. A linear background has been subtracted and the data are shifted vertically for clarity.* **(b)** *Schematic of the device and the two different measurement geometries that were used for the CSC experiments, applying charge currents along positive and negative x components, respectively.* **(c-d)** *Spin switch non-local signals for each of the two measurement setups in* (b). *The measurements were performed for $I = 120\,\mu$A and $V_g = -60\,$V and for $I = 300\,\mu$A and $V_g = -75\,$V, respectively.*

In order to investigate the origin of the CSC, spin experiments were performed for the different measurement geometries in Figure 5.2b. In the first geometry, the bias current I_1 is passed on the $+x$ side of the BSTS flake and the non-local voltage V_1 is detected on the $-x$ side of the flake. In the second setup, an opposite geometry is used with I_2 and V_2. As shown in Figures 5.2c and 5.2d, there is a sign change for the spin switch signal between the two measurement geometries: setup 1 gives a high non-local voltage when the contact magnetisation of the detector is in the $-y$ direction and a low non-local voltage for $+y$ contact magnetisation, while setup 2 gives the opposite. The origin of the CSC must therefore be odd with the

x component of the charge current. The geometry dependence was also measured through Hanle spin precession, but the device unfortunately broke before a full set of measurements could be obtained for geometry 2. Due to the incomplete data, it is hard to draw any conclusions about the dependence on the measurement geometry from the Hanle measurements, and therefore only the spin switch results are considered for this part of the discussion. The odd behaviour with the x component of the charge current does not help to distinguish between the SHE, the REE and the TSML, since all of there effects depend on the in-plane charge current direction [16, 28, 74]. However, there have been reports of unconventional CSC which is independent of the x component of the charge current [91], and this unconventional CSC origin can, at least, be ruled out.

The bias current dependence of the spin signal was examined through both spin switch and Hanle measurements. A schematic of the experimental setup is shown in Figure 5.3a. Both the spin switch (Figure 5.3b) and the Hanle (Figure 5.3c) signals show a sign change with reversed bias current. Furthermore, Figure 5.3d shows a linear bias dependence of the peak-to-peak amplitude of the Hanle signals. This linear behaviour is also observed for the spin switch signals (see Appendix C). Considering that a reversed bias current includes changing the x component of the applied charge current, a sign change of the spin signal is anticipated. The linear bias dependence is also expected, since a larger charge current enables the polarisation of a larger spin current. Furthermore, the observation of a linear bias dependence also rules out any thermal effects in the measured bias range, since these would have given rise to a nonlinear bias dependence [21, 111].

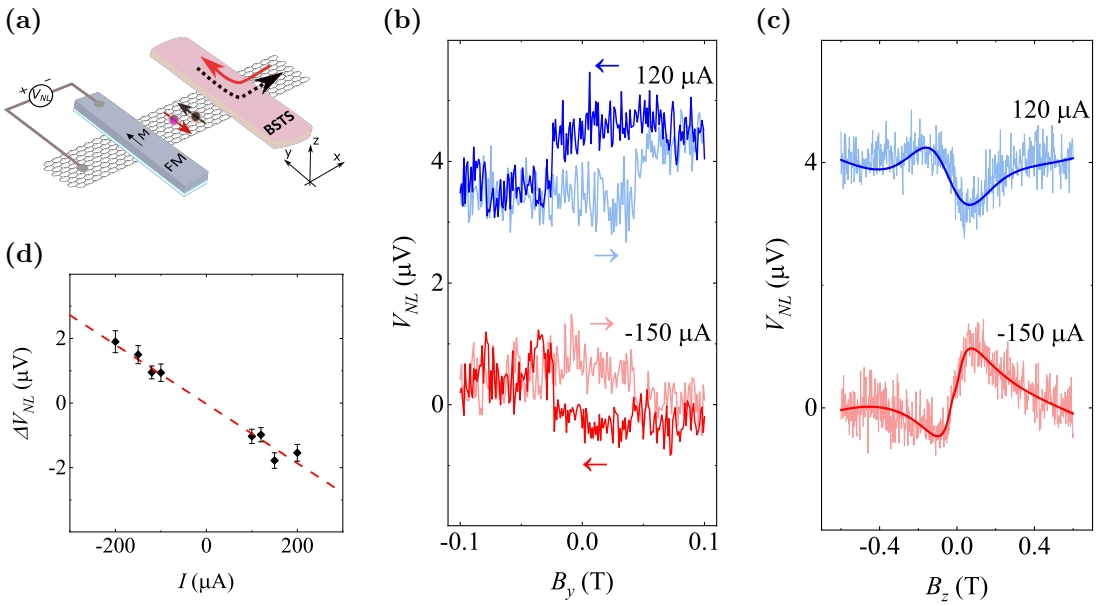

Figure 5.3: *Bias current dependence of the CSC signal.* **(a)** *Schematic of the device and the used measurement geometry with arrows indicating positive and negative bias charge currents.* **(b)** *Spin switch non-local signals for positive ($I = 120\,\mu$A) and negative ($I = -150\,\mu$A) bias currents. The measurements were performed for $V_g = -60$ V. The data are shifted vertically for clarity.* **(c)** *Hanle spin precession non-local signals for positive ($I = 120\,\mu$A) and negative ($I = -150\,\mu$A) bias currents and corresponding antisymmetric fits. The measurements were performed for $V_g = -70$ V. Linear backgrounds have been removed and the data are shifted vertically for clarity.* **(d)** *The peak-to-peak amplitude of the measured Hanle signals as a function of bias current and a linear fit.*

However, it is not possible to discern which mechanism is the origin of the CSC from the bias dependence of the spin signals. Linear bias dependencies have been reported for each of the SHE [55, 92], the REE [112] and the TSML [22, 40, 77], but these results come from different types of measurements and different measurement geometries, and can therefore not be compared directly to the obtained results of this thesis work. Hence, further investigations are required to find the origin of the obtained CSC signals.

The gate dependence of the spin signal was investigated in the same way as the bias dependence. However, no sign change of the signal was detected for reversed gate voltage, as shown in Figures 5.4a and 5.4b for spin switch and Hanle spin precession, respectively. The gate dependence of the peak-to-peak amplitude of the Hanle signals is shown in greater detail in the second panel of Figure 5.4c. The amplitude is mainly independent of gate voltage, but the signal vanishes around $V_g = 45$ V, which corresponds to the Dirac point of the graphene channel (detected as a voltage maximum from local transport measurements across the vdW heterostructure, shown in the top panel of Figure 5.4c). The two bottom panels of Figure 5.4c show the gate dependence of the spin lifetime and the spin diffusion length, where the parameters have been extracted from fittings of the measured Hanle signals using

Equations (3.6). The extracted values of the spin lifetime and the spin diffusion length are around 75 ps and 1.5 μm, respectively, but a weak linear dependence can be seen where both parameters decrease closer to the Dirac point of the graphene.

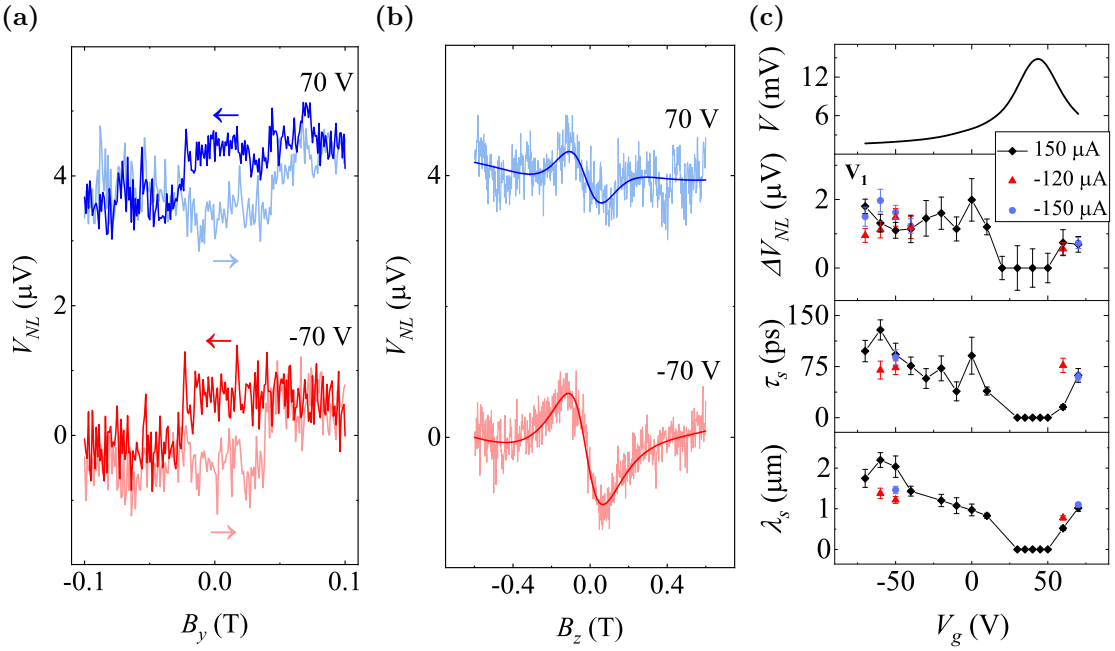

Figure 5.4: *Gate voltage dependence of the CSC signal.* **(a)** *Spin switch non-local signals for positive and negative gate voltages ($V_g = \pm 70$ V). The measurements were performed for $I = 150\,\mu$A. The data are shifted vertically for clarity.* **(b)** *Hanle spin precession non-local signals for positive and negative gate voltage ($V_g = \pm 70$ V) and corresponding antisymmetric fits. The measurements were performed for $I = 150\,\mu$A. Linear backgrounds have been removed and the data are shifted vertically for clarity.* **(c)** *Top panel: Local voltage measured when passing a 1 μA current through the graphene channel across the vdW heterostructure as a function of gate voltage. The voltage maximum at $V_g = 45$ V corresponds to the graphene Dirac point. Three bottom panels: The peak-to-peak amplitude of the measured Hanle signals as well as spin lifetimes and spin diffusion lengths, extracted from symmetric and antisymmetric fittings of the Hanle signals, as functions of gate voltage. The measurements were performed with $I = 150\,\mu$A for the main set of data and with $I = -120\,\mu$A and $I = -150\,\mu$A for the supporting data points.*

The absence of a sign change of the spin signal as the Fermi level is tuned across the graphene Dirac point indicates that the CSC comes from the TI and not from proximitised graphene. This is because both the proximity-induced SHE and the proximity-induced REE would have given rise to a sign change of the spin polarisation when the charge carrier type in graphene changes [28, 48, 63]. The bulk SHE and the bulk REE, however, do not normally cause a sign change, since this would necessitate the Fermi level to be tuned across the TI band gap and would therefore require a very large applied gate voltage [28, 67]. The TSML does not give a sign change either, even when the Fermi level is tuned across the TI Dirac point, due to the opposite chirality of the SML above and below the Dirac point, which

counteracts the effect of the changed charge carrier types [22, 28]. The ruling out of the proximity-induced CSC mechanisms is further supported by the results from the spin lifetime anisotropy experiment in Section 4.3, where the mostly isotropic spin lifetime indicates negligible proximity effects from the BSTS flake on the graphene channel.

The disappearance of the spin signal around the graphene Dirac point is likely due to a conductivity mismatch between the graphene channel and the TI flake. The resistance of the graphene is at a maximum at the Dirac point, which increases the likelihood of injected spins diffusing back into the TI instead of propagating along the graphene channel, leading to a decreased spin injection efficiency and, subsequently, a lower spin signal [88, 97, 107]. Additionally, the strong SOC of the TI can increase the relaxation rate of the reabsorbed spins, which reduces the spin injection further [73].

5.2 Spin-to-charge conversion

The SCC experiments were made in a similar fashion to the CSC ones. Instead of injecting a charge current into the TI flake and detecting the non-local voltage between a FM electrode and a nonmagnetic reference contact, a charge current was here injected into a FM contact and the non-local voltage was measured between the TI flake and a reference contact, as viewed in Figure 5.5a. The injected charge current is partially converted into a polarised spin current by the FM contact and the spins can then be detected as a non-local voltage due to SCC in the TI. The possible origins of the SCC are the Onsager reciprocals of the possible CSC origins: the inverse SHE (ISHE), the inverse REE (IREE) and SCC through TSML. In the ISHE, spins are deflected in the same way as in the SHE, but since opposite spins travel in opposite directions in a spin current, all spins are deflected in the same direction and a transverse charge current is generated. In the IREE and the TSML, the spin polarisation causes the Fermi surface spin textures to shift from the equilibrium position in the way showed in Figure 5.5b, which gives rise to a charge current.

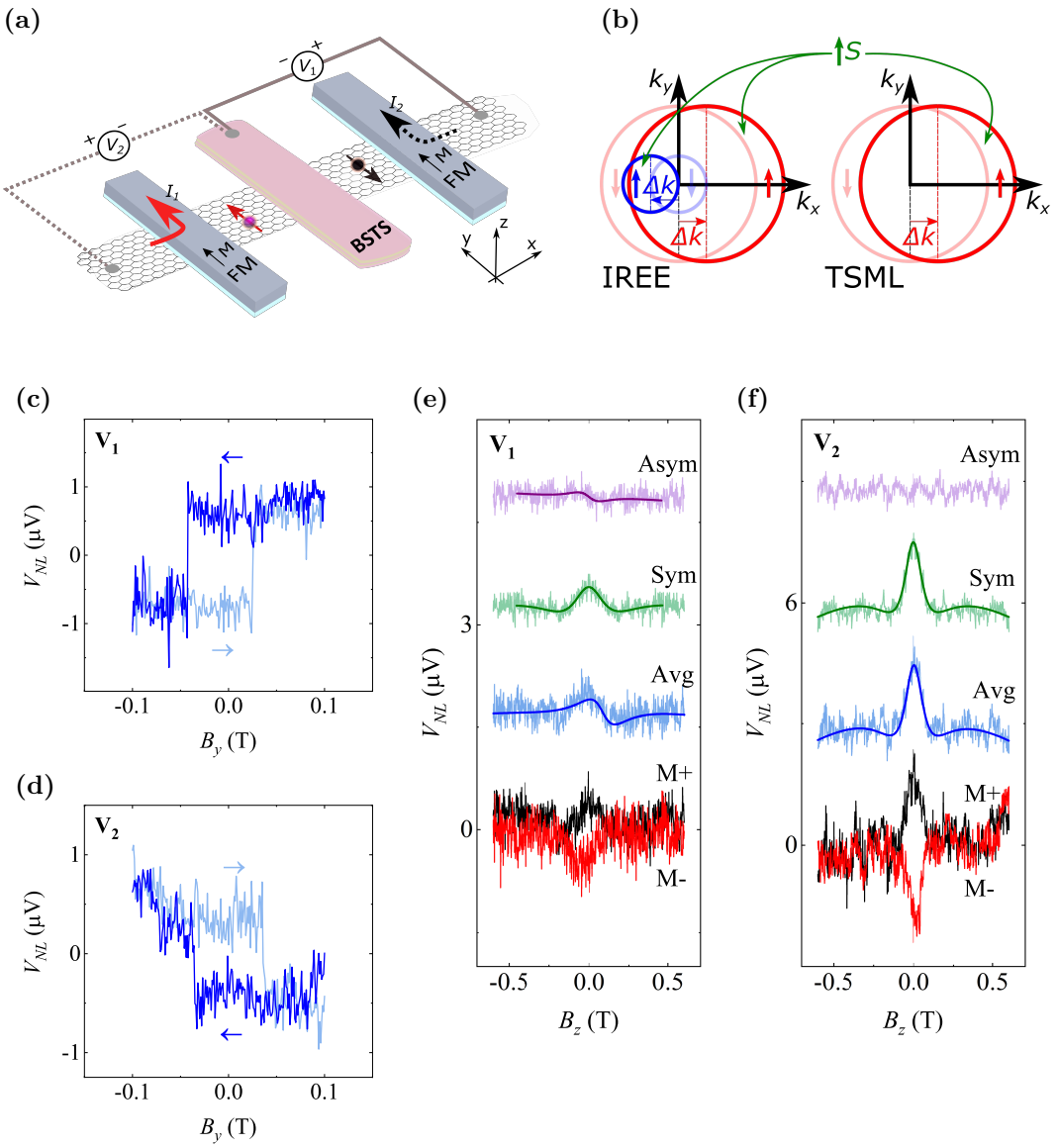

Figure 5.5: *Spin-to-charge conversion in the TI.* **(a)** *Schematic of the device and the two different measurement setups for measuring SCC by injecting a spin polarised current from FM electrodes and detecting it with the TI flake, applying the spin currents along positive and negative x components, respectively.* **(b)** *Schematic of the Fermi surface of a TI, in the spin-split conduction or valence bulk bands (left) and in the topological surface states (right). When a spin current is applied, the spin textures of the Fermi surface shift and can yield a charge current through the IREE or the TSML, respectively.* **(c-d)** *Spin switch non-local signals for each of the two measurement setups in* (a). *The measurements were performed for $I = -150\,\mu$A and $V_g = -70$ V and for $I = -100\,\mu$A and $V_g = -75$ V, respectively.* **(e-f)** *Hanle spin precession non-local signals for each of the two measurement setups in* (a) *with FM contact magnetisation along the $+y$ (black curve) and the $-y$ direction (red curve), respectively, as well as the averaged signal (light blue curve) and the symmetric (light green curve) and the antisymmetric (violet curve) components of the averaged signal. The dark blue, dark green and purple curves are fits of the respective signals. The measurements were performed for $I = 130\,\mu$A and $V_g = -75$ V. Linear backgrounds have been removed and the data are shifted vertically for clarity.*

Spin switch measurements in each of the two geometries in Figure 5.5a gave the results in Figures 5.5c and 5.5d, respectively. The jumps in non-local voltage show that there is indeed SCC since the detected non-local voltage changes sign when the polarisation of the injected spin current is reversed. Additionally, the sign change of the signal between the two measurement geometries means that the SCC has a dependence on the x component of the spin current, similarly to the CSC. This, combined with the fact that no sign change of the SCC signal was detected for reversal of the gate voltage (see Appendix C), agrees with the results from the CSC experiments and indicates that the SCC comes from the TI, in the form of bulk ISHE, bulk IREE or TSML.

It should be noted that no sign change of the SCC signal was observed for reversed bias current, which stands in contrast to the CSC results. This is, however, not a feature of the SCC but rather of the spin injection from the FM contacts. Spin valve measurements across pristine graphene in the same device (presented in Figure 4.1f of Chapter 4) show that the spin signal magnitude indeed changes sign when the bias current goes from negative to small positive values but then changes sign again for larger positive bias currents. This is thought to happen because of local hot-electron effects across the contact tunnel junctions at higher bias currents and/or because of the complex electronic structure of the FM-graphene hybrid interfaces at the injector electrode [103]. Since the SCC signal was detected only for large positive bias currents, the polarisation of the injected spins is similar to the spin polarisation for negative bias, and a similar SCC is subsequently measured at the TI. The unusual bias dependence of the SCC signal is thus no reason to doubt the results and conclusions above.

The results from the Hanle spin precession measurements are shown in Figures 5.5e and 5.5f for each of the measurement geometries, respectively. The signals for opposite contact magnetisation direction were averaged and subsequently deconvoluted into symmetric and antisymmetric components in the same way as described in Section 5.1. The angle between the polarisation of the injected spins from the FM contact and the SCC of the TI was calculated to $\varphi = 24 \pm 8°$ for the first geometry and to $\varphi = 7.2 \pm 0.2°$ for the second geometry. Since the signal-to-noise ratio is much larger in Figure 5.5f than in Figure 5.5e, it can be argued that $\varphi = 7.2 \pm 0.2°$ is the more reliable value. The measurements in the second geometry also give a spin lifetime of 75 ps and a spin diffusion length of 1.3 μm, which are very close to the obtained results from the CSC experiments.

The asymmetry of the Hanle signals and the values of φ are significantly different between the CSC case and the SCC case, especially if the SCC measurements are to be considered more reliable in the second geometry. This suggests that the polarised spins are behaving differently at the graphene/TI interface in the two cases. One possible reason for this is that the repeatedly applied currents and voltages have caused the graphene/TI interface to change slightly between the CSC and the SCC measurements. However, this disagrees with the chronology of the experiments, since the SCC experiments were performed before the second set of CSC measurements, and can thus be ruled out.

A more likely explanation is that the polarised spins travel along different paths through the interface and/or the BSTS flake. In the CSC case, the applied bias current is passed diagonally through the TI with nonzero x, y and z components. It is therefore reasonable that the spin polarisation will also be diagonal (perpendicular to the charge current), which corresponds to the obtained $67 \pm 1°$ angle. In the SCC case, on the other hand, the injected spins are initially parallel to the FM contact magnetisation. At the graphene/TI interface, a portion of the polarised spins will then be absorbed by the BSTS flake. However, it is not obvious where and how the spins will cross the vdW gap, nor is it obvious which path the charge current will take after the SCC.

It is probable that the vdW gap of the graphene/TI interface has some thinner areas and some wider areas, due to unevenness in the surface of the wafer and/or of the BSTS flake. While the polarised spins in the CSC case might be injected across a wider part of the vdW gap, where the interface resistance is higher and the conductivity mismatch problem is mitigated, the polarised spins in the SCC case might instead be absorbed across a thinner part of the vdW gap, where the interface resistance is at a minimum. This difference could potentially give rise to the difference in the Hanle signal asymmetry, since the system geometry, the effective channel length between the FM contact and the BSTS flake and, potentially, the interference from the graphene/TI interface would be different between the CSC case and the SCC case.

Furthermore, the path of the charge current after the SCC could also affect the Hanle signal asymmetry, since it is the converted charge current that gives rise to the non-local voltage. Depending on which SCC mechanism is dominating, the charge current direction can be dependent either on the spin polarisation or the spin current direction, but the geometry of the BSTS flake as well as the properties of the graphene/TI interface will most likely also have an impact. There are thus several layers of uncertainty regarding the true origin of the difference in Hanle signal asymmetry between the CSC and the SCC measurements. Hence, these explanations are mainly speculative, and more detailed studies are necessary for any firm conclusions to be made.

6

Summary and Conclusions

Spintronics is an innovative approach to combat the problems with increasing energy losses that conventional electronics encounter as the size of a transistor is reaching the nanometre scale. By utilising the electrons' spins instead of their charges, spintronics offers a new avenue for achieving fast and energy-efficient data storage and processing. In order to make these next-generation computing components feasible, there is a great need for efficient generation, transport and detection of polarised spin.

Topological insulators (TIs) and their unique electronic band structure have attracted a lot of attention among spintronics researchers in recent years. This new class of materials has a strong spin-orbit coupling (SOC) and showcases topological surface states with spin-momentum locking (SML), where the charge carriers' spins and momenta are locked perpendicular to each other. Thanks to these properties, TIs show promise to be very useful for electrical charge-spin interconversion without the need of ferromagnetic (FM) contacts. However, while charge-spin interconversion in TIs has previously been reported using spin potentiometric measurement methods, reliable non-local measurements have so far been limited to cryogenic temperatures.

In this master's thesis work, a spin valve device was fabricated with a van der Waals (vdW) heterostructure of $Bi_{1.5}Sb_{0.5}Te_{1.7}Se_{1.3}$ and graphene as the central component, where $Bi_{1.5}Sb_{0.5}Te_{1.7}Se_{1.3}$ (BSTS) is a TI. This type of heterostructure makes it possible to combine the strong SOC of the TI with the excellent transport properties of graphene. Both charge-to-spin conversion (CSC) and spin-to-charge conversion (SCC) could be detected non-locally at room temperature in this device through spin switch and Hanle spin precession measurements.

Further experiments were conducted in order to identify the origin of the observed charge-spin interconversion. There are generally three possible mechanisms that can give rise to CSC in a graphene/TI vdW heterostructure: the spin Hall effect (SHE), the Rashba-Edelstein effect (REE) and the topological SML (TSML). The SHE and the REE can appear either in the bulk of the TI or in the graphene due to proximity-effects, while the TSML appears only in the TI surface states.

First, CSC was detected in two different measurement geometries, in order to in-

vestigate the dependence on the x component of the applied charge current (here, the x direction is along the graphene channel of the device). The measurements showed that the spin signal changes sign, corresponding to an opposite spin polarisation, which is expected for all of the aforementioned CSC origins. The results do, however, allow the ruling out of any unconventional CSC mechanisms.

Second, the bias current and gate voltage modulations of the CSC signal were studied. The spin signal showed a linear bias dependence, which rules out any thermal effects that would have caused a nonlinear bias dependence if they were present.

The gate voltage modulation showed a mainly constant gate dependence of the spin signal, except from around the Dirac point of the graphene channel, where the signal could not be detected, most likely because of the conductivity mismatch problem. If the CSC had been caused by the proximity-induced SHE or the proximity-induced REE, the change in charge carrier type would have given rise to a sign change of the spin signal at the graphene Dirac point. The absence of such a sign change means that none of the proximity-induced mechanisms were the origin of the detected CSC. It could therefore be concluded that CSC must originate in the TI, from the SHE, the REE or the TSML.

Finally, similar investigations were performed for the SCC. Bias modulations showed a V-shaped bias dependence rather than a strictly linear one. However, this was confirmed to come from the spin injection across the graphene/FM contact interface, probably due to hot electron effects. Experiments with different measurement geometries and with gate voltage modulations showed the same type of behaviour as the CSC, and it could thus be concluded that the SCC did not originate from proximity-induced effects, but rather from the inverse SHE (ISHE), the inverse REE (IREE) or the TSML in the TI.

In summary, CSC and SCC were successfully detected in a graphene/BSTS vdW heterostructure, using spin potentiometric measurement methods non-locally at room temperature. Measurements probing the bias and gate dependencies in different measurement geometries prove the robustness of the charge-spin interconversion at room temperature, and show that the CSC and the SCC both originate in the TI itself, through the SHE, the REE or the TSML. These findings demonstrate the possibility to use TIs for all-electrical room-temperature spintronics devices for energy-efficient next-generation computing components.

Bibliography

[1] Gordon E Moore. "Cramming more components onto integrated circuits". In: *Electronics* 38.8 (1965), p. 114. ISSN: 1098-4232. URL: papers3://publication/uuid/8E5EB7C8-681C-447D-9361-E68D1932997D.

[2] André Dankert. "Spin Transport in Two-Dimensional Material Heterostructures". PhD thesis. Chalmers University of Technology, 2015.

[3] Nicola Jones. "How to stop data centres from gobbling up the world's electricity". In: *Nature* 561 (2018), pp. 163–166. ISSN: 14764687. DOI: 10.1038/d41586-018-06610-y.

[4] Hanan Dery et al. "Reconfigurable nanoelectronics using graphene based spintronic logic gates". In: *Spintronics IV*. Ed. by Henri-Jean M. Drouhin, Jean-Eric Wegrowe, and Manijeh Razeghi. Vol. 8100. SPIE, 2011, pp. 151–161. ISBN: 9780819487100. DOI: 10.1117/12.890318.

[5] Yingying Wu et al. "Large exchange splitting in monolayer graphene magnetized by an antiferromagnet". In: *Nature Electronics* 3.10 (2020), pp. 604–611. ISSN: 25201131. DOI: 10.1038/s41928-020-0458-0. URL: http://dx.doi.org/10.1038/s41928-020-0458-0.

[6] Wei Han et al. "Graphene spintronics". In: *Nature Nanotechnology* 9 (2014), pp. 794–807. ISSN: 17483395. DOI: 10.1038/nnano.2014.214.

[7] Dmitrii Khokhriakov et al. "Two-dimensional spintronic circuit architectures on large scale graphene". In: *Carbon* 161 (2020), pp. 892–899. ISSN: 00086223. DOI: 10.1016/j.carbon.2020.01.103. URL: https://doi.org/10.1016/j.carbon.2020.01.103.

[8] Behtash Behin-Aein et al. "Proposal for an all-spin logic device with built-in memory". In: *Nature Nanotechnology* 5.4 (2010), pp. 266–270. ISSN: 17483395. DOI: 10.1038/nnano.2010.31.

[9] Sasikanth Manipatruni et al. "Scalable energy-efficient magnetoelectric spin–orbit logic". In: *Nature* 565 (2019), pp. 35–42. ISSN: 14764687. DOI: 10.1038/s41586-018-0770-2. URL: http://dx.doi.org/10.1038/s41586-018-0770-2.

[10] Dmitrii Khokhriakov. "Graphene spin circuits and spin-orbit phenomena in van der Waals heterostructures with topological insulators". PhD thesis. Chalmers University of Technology, 2021.

[11] Björn Trauzettel et al. "Spin qubits in graphene quantum dots". In: *Nature Physics* 3 (2007), pp. 192–196. ISSN: 17452481. DOI: 10.1038/nphys544.

[12] J. Grollier et al. “Neuromorphic spintronics”. In: *Nature Electronics* 3 (2020), pp. 360–370. ISSN: 25201131. DOI: 10.1038/s41928-019-0360-9. URL: http://dx.doi.org/10.1038/s41928-019-0360-9.

[13] T. Kawahara et al. “Spin-transfer torque RAM technology: Review and prospect”. In: *Microelectronics Reliability* 52.4 (2012), pp. 613–627. ISSN: 00262714. DOI: 10.1016/j.microrel.2011.09.028. URL: http://dx.doi.org/10.1016/j.microrel.2011.09.028.

[14] Ioan Mihai Miron et al. “Perpendicular switching of a single ferromagnetic layer induced by in-plane current injection”. In: *Nature* 476 (2011), pp. 189–193. ISSN: 00280836. DOI: 10.1038/nature10309.

[15] Luqiao Liu et al. “Spin-torque switching with the giant spin Hall effect of tantalum”. In: *Science* 336.6081 (2012), pp. 555–558. ISSN: 10959203. DOI: 10.1126/science.1218197.

[16] Jairo Sinova et al. “Spin Hall effects”. In: *Reviews of Modern Physics* 87.4 (2015), pp. 1213–1260. ISSN: 15390756. DOI: 10.1103/RevModPhys.87.1213.

[17] Xiaoyang Lin et al. “Two-dimensional spintronics for low-power electronics”. In: *Nature Electronics* 2 (2019), pp. 274–283. ISSN: 25201131. DOI: 10.1038/s41928-019-0273-7.

[18] A. Avsar et al. “Colloquium: Spintronics in graphene and other two-dimensional materials”. In: *Reviews of Modern Physics* 92.2 (2020). ISSN: 15390756. DOI: 10.1103/REVMODPHYS.92.021003.

[19] Jayakumar Balakrishnan et al. “Colossal enhancement of spin-orbit coupling in weakly hydrogenated graphene”. In: *Nature Physics* 9.5 (2013), pp. 284–287. ISSN: 17452481. DOI: 10.1038/nphys2576.

[20] Yoichi Ando. “Topological Insulator Materials”. In: *Journal of the Physical Society of Japan* 82.10 (2013), p. 102001. DOI: 10.7566/JPSJ.82.102001.

[21] Kristina Vaklinova et al. “Current-Induced Spin Polarization in Topological Insulator-Graphene Heterostructures”. In: *Nano Letters* 16.4 (2016), pp. 2595–2602. ISSN: 15306992. DOI: 10.1021/acs.nanolett.6b00167.

[22] André Dankert et al. “Origin and evolution of surface spin current in topological insulators”. In: *Physical Review B* 97.12 (2018), p. 125414. DOI: 10.1103/PhysRevB.97.125414.

[23] Bogdan Karpiak et al. “Magnetic proximity in a van der Waals heterostructure of magnetic insulator and graphene”. In: *2D Materials* 7.1 (2020), p. 015026. ISSN: 23318422. DOI: 10.1088/2053-1583/ab5915.

[24] K. S. Novoselov et al. “2D materials and van der Waals heterostructures”. In: *Science* 353.6298 (2016), p. 461. ISSN: 10959203. DOI: 10.1126/science.aac9439.

[25] C. K. Safeer et al. “Room-Temperature Spin Hall Effect in Graphene/MoS2 van der Waals Heterostructures”. In: *Nano Letters* (2019). ISSN: 15306992. DOI: 10.1021/acs.nanolett.8b04368.

[26] C. L. Kane and E. J. Mele. “Z2 topological order and the quantum spin Hall effect”. In: *Physical Review Letters* 95.14 (Sept. 2005). ISSN: 00319007. DOI: 10.1103/PhysRevLett.95.146802.

[27] Nitesh Kumar et al. “Topological Quantum Materials from the Viewpoint of Chemistry”. In: *Chemical Reviews* 121.5 (2020), pp. 2780–2815. ISSN: 15206890. DOI: 10.1021/acs.chemrev.0c00732.

[28] Dmitrii Khokhriakov et al. “Gate-tunable spin-galvanic effect in graphene-topological insulator van der Waals heterostructures at room temperature”. In: *Nature Communications* 11.3657 (2020), pp. 1–7. ISSN: 20411723. DOI: 10.1038/s41467-020-17481-1.

[29] Y. Xia et al. “Observation of a large-gap topological-insulator class with a single Dirac cone on the surface”. In: *Nature Physics* 5.6 (2009), pp. 398–402. ISSN: 17452481. DOI: 10.1038/nphys1274.

[30] D. Hsieh et al. “A tunable topological insulator in the spin helical Dirac transport regime”. In: *Nature* 460.7259 (2009), pp. 1101–1105. ISSN: 00280836. DOI: 10.1038/nature08234.

[31] Bin Xia et al. “Indications of surface-dominated transport in single crystalline nanoflake devices of topological insulator Bi1.5Sb0.5Te1.8Se1.2”. In: *Physical Review B - Condensed Matter and Materials Physics* 87.8 (2013), pp. 1–8. ISSN: 10980121. DOI: 10.1103/PhysRevB.87.085442.

[32] C. L. Kane and E. J. Mele. “Quantum spin Hall effect in graphene”. In: *Physical Review Letters* 95.22 (2005), pp. 1–4. ISSN: 00319007. DOI: 10.1103/PhysRevLett.95.226801.

[33] Markus König et al. “Quantum spin Hall insulator state in HgTe quantum wells”. In: *Science* 318.5851 (Nov. 2007), pp. 766–770. ISSN: 00368075. DOI: 10.1126/science.1148047.

[34] Chaoxing Liu et al. “Quantum spin Hall effect in inverted type-II semiconductors”. In: *Physical Review Letters* 100.23 (June 2008). ISSN: 00319007. DOI: 10.1103/PhysRevLett.100.236601.

[35] Y. Xia et al. “Observation of a large-gap topological-insulator class with a single Dirac cone on the surface”. In: *Nature Physics* 5.6 (2009), pp. 398–402. ISSN: 17452481. DOI: 10.1038/nphys1274.

[36] D. Hsieh et al. “Observation of time-reversal-protected single-Dirac-cone topological-insulator states in Bi2Te3 and Sb2Te3”. In: *Physical Review Letters* 103.146401 (2009), pp. 1–4. ISSN: 00319007. DOI: 10.1103/PhysRevLett.103.146401.

[37] Zhi Ren et al. “Optimizing Bi2-xSbxTe3-ySey solid solutions to approach the intrinsic topological insulator regime”. In: *Physical Review B* 84.16 (2011), p. 165311. ISSN: 10980121. DOI: 10.1103/PhysRevB.84.165311.

[38] Shu Cai et al. “Independence of topological surface state and bulk conductance in three-dimensional topological insulators”. In: *npj Quantum Materials* 3.62 (Nov. 2018), pp. 1–6. ISSN: 23974648. DOI: 10.1038/s41535-018-0134-z. URL: www.nature.com/npjquantmats.

[39] Barry Bradlyn et al. “Topological quantum chemistry”. In: *Nature* 547 (July 2017), pp. 298–305. ISSN: 14764687. DOI: 10.1038/nature23268. URL: www.cryst.ehu.es/cgi-bin/cryst/programs/bandrep.pl.

[40] André Dankert et al. “Room temperature electrical detection of spin polarized currents in topological insulators”. In: *Nano Letters* 15.12 (2015), pp. 7976–7981. ISSN: 15306992. DOI: 10.1021/acs.nanolett.5b03080.

[41] Y. Pan et al. “Low carrier concentration crystals of the topological insulator Bi2-xSbxTe3-ySey: A magnetotransport study”. In: *New Journal of Physics* 16 (2014), p. 123035. ISSN: 13672630. DOI: 10.1088/1367-2630/16/12/123035.

[42] Gregory M. Stephen et al. “Weak Antilocalization and Anisotropic Magnetoresistance as a Probe of Surface States in Topological Bi2TexSe3-x Thin Films”. In: *Scientific Reports* 10.1 (2020), pp. 1–7. ISSN: 20452322. DOI: 10.1038/s41598-020-61672-1. URL: http://dx.doi.org/10.1038/s41598-020-61672-1.

[43] Stephane Yu Matsushita et al. “Large thermopower in topological surface state of Sn-BSTS topological insulators: Thermoelectrics and energy-dependent relaxation times”. In: *Physical Review Materials* 5.014205 (2021), pp. 1–8. ISSN: 24759953. DOI: 10.1103/physrevmaterials.5.014205.

[44] Supriyo Bandyopadhyay and Marc Cahay. *Introduction to Spintronics*. 2nd ed. Boca Raton, Florida: CRC Press, 2016. ISBN: 978-1-4822-5557-7.

[45] David J Griffiths and Darrell F Schroeter. *Introduction to Quantum Mechanics*. 3rd ed. Cambridge: Cambridge University Press, 2018. ISBN: 9781107189638.

[46] A. H. Castro Neto and F. Guinea. “Impurity-induced spin-orbit coupling in graphene”. In: *Physical Review Letters* 103.2 (2009), pp. 1–4. ISSN: 00319007. DOI: 10.1103/PhysRevLett.103.026804.

[47] L. Antonio Benítez et al. “Tunable room-temperature spin galvanic and spin Hall effects in van der Waals heterostructures”. In: *Nature Materials* 19.2 (Feb. 2020), pp. 170–175. ISSN: 14764660. DOI: 10.1038/s41563-019-0575-1.

[48] Franz Herling et al. “Gate tunability of highly efficient spin-to-charge conversion by spin Hall effect in graphene proximitized with WSe2”. In: *APL Materials* 8.7 (2020). ISSN: 2166532X. DOI: 10.1063/5.0006101.

[49] Kenan Song et al. “Spin Proximity Effects in Graphene/Topological Insulator Heterostructures”. In: *Nano Letters* 18.3 (2018), pp. 2033–2039. ISSN: 15306992. DOI: 10.1021/acs.nanolett.7b05482.

[50] Zhiyong Wang et al. “Proximity-induced ferromagnetism in graphene revealed by the anomalous Hall effect”. In: *Physical Review Letters* 114.1 (2015), pp. 1–5. ISSN: 10797114. DOI: 10.1103/PhysRevLett.114.016603.

[51] Rai Moriya, Naoto Yabuki, and Tomoki Machida. “Superconducting proximity effect in a NbSe2/graphene van der Waals junction”. In: *Physical Review B* 101.5 (2020), pp. 4–6. ISSN: 24699969. DOI: 10.1103/PhysRevB.101.054503.

[52] Jayakumar Balakrishnan et al. “Giant spin Hall effect in graphene grown by chemical vapour deposition”. In: *Nature Communications* 5 (2014). ISSN: 20411723. DOI: 10.1038/ncomms5748.

[53] M. I. D’yakonov and V. I. Perel’. “Possibility of Orienting Electron Spins with Current”. In: *Soviet Physics JETP Letters* 13.11 (1971), pp. 467–469. URL: http://www.jetpletters.ac.ru/ps/1587/article_24366.shtml.

[54] N. F. Mott. “The Scattering of Fast Electrons by Atomic Nuclei”. In: *Proceedings of the Royal Society A* 124.794 (1929), pp. 425–442. DOI: https://doi.org/10.1098/rspa.1929.0127.

[55] Y. K. Kato et al. “Observation of the spin Hall effect in semiconductors”. In: *Science* 306.5703 (2004), pp. 1910–1913. ISSN: 00368075. DOI: 10.1126/science.1105514.

[56] Jairo Sinova et al. “Universal intrinsic spin Hall effect”. In: *Physical Review Letters* 92.12 (2004), pp. 1–4. ISSN: 00319007. DOI: 10.1103/PhysRevLett.92.126603.

[57] Shuichi Murakami, Naoto Nagaosa, and Shou-cheng Zhang. “Dissipationless Quantum Spin Current at Room Temperature”. In: *Science* 301.5638 (2003), pp. 1348–1351. DOI: 10.1126/science.1087128.

[58] J. Wunderlich et al. “Experimental observation of the spin-Hall effect in a two-dimensional spin-orbit coupled semiconductor system”. In: *Physical Review Letters* 94.4 (2005), p. 047204. ISSN: 00319007. DOI: 10.1103/PhysRevLett.94.047204.

[59] Nguyen Huynh Duy Khang, Yugo Ueda, and Pham Nam Hai. “A conductive topological insulator with large spin Hall effect for ultralow power spin-orbit torque switching”. In: *Nature Materials* 17.9 (2018), pp. 808–813. ISSN: 14764660. DOI: 10.1038/s41563-018-0137-y.

[60] Zhendong Chi et al. “The spin Hall effect of Bi-Sb alloys driven by thermally excited Dirac-like electrons”. In: *Science Advances* 6.10 (2020), pp. 1–9. ISSN: 23752548. DOI: 10.1126/sciadv.aay2324.

[61] A. Manchon et al. “New perspectives for Rashba spin-orbit coupling”. In: *Nature Materials* 14.9 (2015), pp. 871–882. ISSN: 14764660. DOI: 10.1038/nmat4360.

[62] S D Ganichev et al. “Spin-galvanic effect”. In: *Nature* 417 (2002), pp. 153–156. DOI: 10.1038/nature747.1..

[63] Lijun Li et al. “Gate-Tunable Reversible Rashba-Edelstein Effect in a Few-Layer Graphene/2H-TaS2 Heterostructure at Room Temperature”. In: *ACS Nano* 14.5 (2020), pp. 5251–5259. ISSN: 1936086X. DOI: 10.1021/acsnano.0c01037.

[64] Talieh S. Ghiasi et al. “Charge-to-Spin Conversion by the Rashba-Edelstein Effect in Two-Dimensional van der Waals Heterostructures up to Room Temperature”. In: *Nano Letters* 19.9 (2019), pp. 5959–5966. ISSN: 15306992. DOI: 10.1021/acs.nanolett.9b01611.

[65] F Bottegoni et al. “Spin-charge interconversion in heterostructures based on group-IV semiconductors”. In: *La Rivista del Nuovo Cimento* 43 (2020), pp. 45–96. DOI: https://doi.org/10.1007/s40766-020-0002-0.

[66] Matthias B. Jungfleisch et al. “Control of Terahertz Emission by Ultrafast Spin-Charge Current Conversion at Rashba Interfaces”. In: *Physical Review Letters* 120.20 (2018), p. 207207. ISSN: 10797114. DOI: 10.1103/PhysRevLett.120.207207. URL: https://doi.org/10.1103/PhysRevLett.120.207207.

[67] Anamul Md Hoque et al. “All-electrical creation and control of giant spin-galvanic effect in 1T’-MoTe2/graphene heterostructures at room temperature”. In: *arXiv* (2019), pp. 1–11. ISSN: 23318422. DOI: https://arxiv.org/abs/1908.09367.

[68] Yu. A. Bychkov and É. I. Rashba. "Properties of a 2D electron gas with lifted spectral degeneracy". In: *JETP Letters* 39.2 (1984), pp. 66–69. URL: http://jetpletters.ru/ps/1264/article_19121.shtml.

[69] H. L. Stormer et al. "Energy structure and quantized hall effect of two-dimensional holes". In: *Physical Review Letters* 51.2 (1983), pp. 126–129. ISSN: 00319007. DOI: 10.1103/PhysRevLett.51.126.

[70] D Stein, K Klitzing, and G Weimann. "Electron Spin Resonance on GaAs-AlxGa1-xAs Heterostructures". In: *Physical Review Letters* 51.2 (1983), pp. 130–133. DOI: https://doi.org/10.1103/PhysRevLett.51.130.

[71] V. M. Edelstein. "Spin polarization of conduction electrons induced by electric current in two-dimensional asymmetric electron systems". In: *Solid State Communications* 73.3 (1990), pp. 233–235. ISSN: 00381098. DOI: 10.1016/0038-1098(90)90963-C.

[72] J. C. Rojas Sánchez et al. "Spin-to-charge conversion using Rashba coupling at the interface between non-magnetic materials". In: *Nature Communications* 4 (2013), pp. 1–7. ISSN: 20411723. DOI: 10.1038/ncomms3944.

[73] Dmitrii Khokhriakov et al. "Tailoring emergent spin phenomena in Dirac material heterostructures". In: *Science Advances* 4.9 (2018), p. 9349. ISSN: 23752548. DOI: 10.1126/sciadv.aat9349. URL: http://advances.sciencemag.org/.

[74] Rui Sun et al. "Large Tunable Spin-to-Charge Conversion Induced by Hybrid Rashba and Dirac Surface States in Topological Insulator Heterostructures". In: *Nano Letters* 19.7 (2019), pp. 4420–4426. ISSN: 15306992. DOI: 10.1021/acs.nanolett.9b01151.

[75] Masataka Mogi et al. "Current-induced switching of proximity-induced ferromagnetic surface states in a topological insulator". In: *Nature Communications* 12.1404 (2021), pp. 1–6. ISSN: 2041-1723. DOI: 10.1038/s41467-021-21672-9.

[76] J. Borge et al. "Spin Hall and Edelstein effects in metallic films: From two to three dimensions". In: *Physical Review B - Condensed Matter and Materials Physics* 89.24 (2014), pp. 1–11. ISSN: 1550235X. DOI: 10.1103/PhysRevB.89.245443.

[77] C. H. Li et al. "Electrical detection of charge-current-induced spin polarization due to spin-momentum locking in Bi2Se3". In: *Nature Nanotechnology* 9 (2014), pp. 218–224. ISSN: 17483395. DOI: 10.1038/nnano.2014.16.

[78] Hailong Wang et al. "Surface-State-Dominated Spin-Charge Current Conversion in Topological-Insulator-Ferromagnetic-Insulator Heterostructures". In: *Physical Review Letters* 117.7 (2016), p. 076601. ISSN: 10797114. DOI: 10.1103/PhysRevLett.117.076601.

[79] A. R. Mellnik et al. "Spin-transfer torque generated by a topological insulator". In: *Nature* 511 (2014), pp. 449–451. ISSN: 14764687. DOI: 10.1038/nature13534.

[80] J. B.S. Mendes et al. "Dirac-surface-state-dominated spin to charge current conversion in the topological insulator (Bi0.22Sb0.78)2Te3 films at room temperature". In: *Physical Review B* 96.18 (2017), p. 180415. ISSN: 24699969. DOI: 10.1103/PhysRevB.96.180415.

[81] Yuichiro Ando et al. “Electrical Detection of the Spin Polarization Due to Charge Flow in the Surface State of the Topological Insulator Bi1.5Sb0.5Te1.7Se1.3”. In: *Nano Letters* 14.11 (2014), pp. 6226–6230. DOI: dx.doi.org/10.1021/nl502546c.

[82] Jianshi Tang et al. “Electrical Detection of Spin-Polarized Conduction in (Bi0.53Sb0.47)2Te3 Topological Insulator”. In: *Nano Letters* 14.9 (2014), pp. 5423–5429. DOI: dx.doi.org/10.1021/nl5026198.

[83] Annika Johansson, Jürgen Henk, and Ingrid Mertig. “Edelstein effect in Weyl semimetals”. In: *Physical Review B* 97.085417 (2018), pp. 1–8. ISSN: 24699969. DOI: 10.1103/PhysRevB.97.085417.

[84] S. A. Crooker and D. L. Smith. “Imaging spin flows in semiconductors subject to electric, magnetic, and strain fields”. In: *Physical Review Letters* 94.23 (2005), pp. 1–4. ISSN: 00319007. DOI: 10.1103/PhysRevLett.94.236601.

[85] Philip Hofmann. *Solid State Physics*. 2nd ed. Weinheim: Wiley-VCH, 2015. ISBN: 978-3-527-41282-2.

[86] Nikolaos Tombros et al. “Electronic spin transport and spin precession in single graphene layers at room temperature”. In: *Nature* 448.7153 (2007), pp. 571–574. ISSN: 14764687. DOI: 10.1038/nature06037.

[87] C. K. Safeer et al. “Large Multidirectional Spin-to-Charge Conversion in Low-Symmetry Semimetal MoTe2 at Room Temperature”. In: *Nano Letters* 19.12 (2019), pp. 8758–8766. ISSN: 15306992. DOI: 10.1021/acs.nanolett.9b03485.

[88] Wei Han et al. “Tunneling spin injection into single layer graphene”. In: *Physical Review Letters* 105.16 (2010), pp. 3–6. ISSN: 00319007. DOI: 10.1103/PhysRevLett.105.167202.

[89] Dmitrii Khokhriakov et al. “Robust spin interconnect with isotropic spin dynamics in chemical vapor deposited graphene layers and boundaries”. In: *ACS Nano* 14.11 (2020), pp. 15864–15873. ISSN: 1936086X. DOI: 10.1021/acsnano.0c07163.

[90] Bing Zhao et al. “Charge-spin conversion signal in WTe2 van der Waals hybrid devices with a geometrical design”. In: *Applied Physics Letters* 117.24 (2020), p. 242401. DOI: 10.1063/5.0029071.

[91] Bing Zhao et al. “Unconventional Charge–Spin Conversion in Weyl-Semimetal WTe2”. In: *Advanced Materials* 32.38 (2020). ISSN: 15214095. DOI: 10.1002/adma.202000818.

[92] Anamul Md. Hoque et al. “Charge-spin conversion in layered semimetal TaTe2 and spin injection in van der Waals heterostructures”. In: *Physical Review Research* 2.3 (2020), p. 033204. ISSN: 0031-899X. DOI: 10.1103/physrevresearch.2.033204.

[93] Takehiro Yamaguchi et al. “Spin relaxation in weak localization regime in multilayer graphene spin valves”. In: *Japanese Journal of Applied Physics* 52.040205 (2013), pp. 1–3. ISSN: 00214922. DOI: 10.7567/JJAP.52.040205.

[94] K. S. Novoselov et al. “Electric Field Effect in Atomically Thin Carbon Films”. In: *Science* 306.5696 (2004), pp. 666–669. DOI: 10.1126/science.1102896.

[95] K. S. Novoselov et al. “Two-dimensional atomic crystals”. In: *Proceedings of the National Academy of Sciences of the United States of America* 102.30 (2005), pp. 10451–10453. ISSN: 00278424. DOI: 10.1073/pnas.0502848102.

[96] Nobel Prize Outreach AB. *Pressmeddelande: Nobelpriset i fysik 2010*. 2010. URL: https://www.nobelprize.org/prizes/physics/2010/9434-pressmeddelande-nobelpriset-i-fysik-2010/.

[97] M. Venkata Kamalakar et al. “Long distance spin communication in chemical vapour deposited graphene”. In: *Nature Communications* 6.6766 (2015), pp. 1–8. ISSN: 20411723. DOI: 10.1038/ncomms7766.

[98] Jose H. Garcia et al. “Spin transport in graphene/transition metal dichalcogenide heterostructures”. In: *Chemical Society Reviews* 47.9 (2018), pp. 3359–3379. ISSN: 14604744. DOI: 10.1039/c7cs00864c.

[99] Juan F Sierra et al. “Van der Waals heterostructures for spintronics and opto-spintronics”. In: *Nature Nanotechnology* (2021). ISSN: 1748-3395. DOI: 10.1038/s41565-021-00936-x.

[100] Donald A Neamen. *Semiconductor Physics and Devices*. 4th ed. New York, NY: McGraw-Hill, 2012. ISBN: 978-0-07-352958-5.

[101] George W. Flynn. “Perspective: The dawning of the age of graphene”. In: *Journal of Chemical Physics* 135.050901 (2011), pp. 1–8. ISSN: 00219606. DOI: 10.1063/1.3615063.

[102] Chang Ju Lee et al. “Extraction of intrinsic field-effect mobility of graphene considering effects of gate-bias-induced contact modulation”. In: *Journal of Applied Physics* 127.18 (2020). ISSN: 10897550. DOI: 10.1063/1.5128050.

[103] Bing Zhao et al. “Electrically controlled spin-switch and evolution of Hanle spin precession in graphene”. In: *2D Materials* 6.035042 (2019), pp. 1–7. ISSN: 20531583. DOI: 10.1088/2053-1583/ab1d83.

[104] C. Józsa et al. “Controlling the efficiency of spin injection into graphene by carrier drift”. In: *Physical Review B - Condensed Matter and Materials Physics* 79.8 (2009), p. 081402. ISSN: 10980121. DOI: 10.1103/PhysRevB.79.081402.

[105] M. Popinciuc et al. “Electronic spin transport in graphene field-effect transistors”. In: *Physical Review B - Condensed Matter and Materials Physics* 80.21 (2009), p. 214427. ISSN: 10980121. DOI: 10.1103/PhysRevB.80.214427.

[106] Wei Han et al. “Electrical detection of spin precession in single layer graphene spin valves with transparent contacts”. In: *Applied Physics Letters* 94.222109 (2009), pp. 1–3. ISSN: 00036951. DOI: 10.1063/1.3147203.

[107] M. Venkata Kamalakar et al. “Enhanced tunnel spin injection into graphene using chemical vapor deposited hexagonal boron nitride”. In: *Scientific Reports* 4 (2014), pp. 1–8. ISSN: 20452322. DOI: 10.1038/srep06146.

[108] Bart Raes et al. “Determination of the spin-lifetime anisotropy in graphene using oblique spin precession”. In: *Nature Communications* 7.11444 (2016), pp. 1–7. ISSN: 20411723. DOI: 10.1038/ncomms11444.

[109] L. Antonio Benítez et al. “Strongly anisotropic spin relaxation in graphene-transition metal dichalcogenide heterostructures at room temperature”. In: *Nature Physics* 14.3 (2018), pp. 303–308. ISSN: 17452481. DOI: 10.1038/

s41567-017-0019-2. URL: http://dx.doi.org/10.1038/s41567-017-0019-2.

[110] Nitin Samarth. "Quantum materials discovery from a synthesis perspective". In: *Nature Materials* 16.11 (2017), pp. 1068–1076. ISSN: 14764660. DOI: 10.1038/NMAT5010.

[111] Jifa Tian et al. "Electrical injection and detection of spin-polarized currents in topological insulator Bi2Te2Se". In: *Scientific Reports* 5.14293 (2015), pp. 1–8. ISSN: 20452322. DOI: 10.1038/srep14293.

[112] Zoltán Kovács-Krausz et al. "Electrically Controlled Spin Injection from Giant Rashba Spin-Orbit Conductor BiTeBr". In: *Nano Letters* 20.7 (2020), pp. 4782–4791. ISSN: 15306992. DOI: 10.1021/acs.nanolett.0c00458.

[113] Stephane Yu Matsushita et al. "Thermoelectric properties of 3D topological insulator: Direct observation of topological surface and its gap opened states". In: *Physical Review Materials* 1.054202 (2017), pp. 1–9. ISSN: 24759953. DOI: 10.1103/PhysRevMaterials.1.054202.

[114] Peter Atkins, Loretta Jones, and Leroy Laverman. *Chemical Principles*. 6th ed. London: W.H.Freeman & Co Ltd, 2012. ISBN: 9781464120671.

[115] M. Venkata Kamalakar et al. "Inversion of Spin Signal and Spin Filtering in Ferromagnet|Hexagonal Boron Nitride-Graphene van der Waals Heterostructures". In: *Scientific Reports* 6.October 2015 (2016), pp. 1–9. ISSN: 20452322. DOI: 10.1038/srep21168. URL: http://dx.doi.org/10.1038/srep21168.

[116] Jingang Wang, Fengcai Ma, and Mengtao Sun. "Graphene, hexagonal boron nitride, and their heterostructures: properties and applications". In: *RSC Advances* 7.27 (2017), pp. 16801–16822. ISSN: 20462069. DOI: 10.1039/c7ra00260b.

[117] James R. Welty, Gregory L. Rorrer, and David G. Foster. *Fundamentals of Momentum, Heat and Mass Transfer*. 6th ed. Hoboken, NJ: John Wiley & Sons, Inc., 2015. ISBN: 978-1-118-80887-0.

A

Fabrication

The fabrication that was done as a part of this master's thesis project is described in this appendix. All fabrication was done in cleanroom facilities at Myfab Chalmers.

A.1 Fabrication process for the van der Waals heterostructure devices

One chip containing seven van der Waals heterostructure devices of BSTS and CVD graphene with nonmagnetic gold contacts and magnetic cobolt contacts was fabricated in this master's thesis project. The fabrication recipe of the chip is presented here.

A.1.1 Chip preparation

A 7 mm × 7 mm chip was cut out from a premade 4″ Si/SiO_2 wafer with chemical vapour deposition (CVD) graphene from Grolltex Inc. The chip was then cleaned in acetone at 65 °C for 5 min, followed by isopropyl alcohol (IPA) at room temperature for 2 min and nitrogen gas (N_2) blow drying.

A.1.2 Electron beam lithography for graphene stripes

The next fabrication step was spin coating the positive resist MMA EL8 onto the chip for 60 s with a rotation speed of 6000 rpm and an acceleration of 50 rpm/s. The resist was then soft baked at 135 °C for 10 min. The MMA EL8 resist functioned as an undercut resist. This was followed by a second spin coating with the positive resist ARP 6200 13 1:2 for 60 s with a rotation speed of 6000 rpm and an acceleration of 50 rpm/s. The second soft baking was also done at 135 °C for 10 min. The resists were then exposed with an electron beam current of 35 nA to make a pattern of 50 μm long stripes with widths of 1, 2 and 3 μm, respectively. The development was done in n-amyl acetate for 45 s followed by MIBK:IPA 1:1 for 1 min 15 s.

The chip was then etched by oxygen plasma with a power of 25 W for 30 s, which was used to remove the unwanted graphene that was no longer protected by the resist. Finally, the remaining resist was removed through cleaning in acetone at

65 °C for 5 min and in IPA at room temperature for 3 min. An example of the resulting graphene stripes is shown in Figure A.1a.

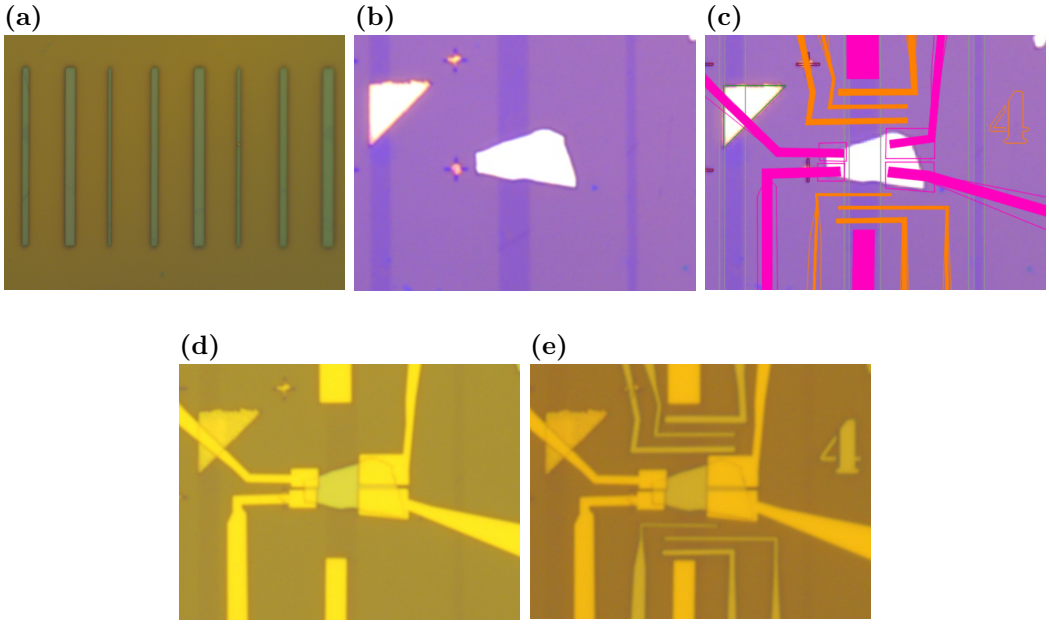

Figure A.1: *The device fabrication process.* **(a)** *Graphene stripes of length* 50 μm *and of widths* 1, 2 *and* 3 μm*, respectively, patterned by electron beam lithography and oxygen plasma etching. This picture was taken before rinsing in acetone and IPA, so the graphene stripes are still covered with resist.* **(b)** *An exfoliated BSTS flake lying across one of the graphene stripes. Not to be confused with the triangular alignment mark in the left of the picture.* **(c)** *Contact mask drawn in AutoCAD with nonmagnetic contacts in pink and magnetic contacts in orange.* **(d)** *Nonmagnetic gold contacts made through evaporation deposition and lift-off.* **(e)** *Nonmagnetic gold contacts and magnetic cobolt contacts made through evaporation deposition and lift-off.*

A.1.3 Exfoliation of BSTS

Nitto tape was used for mechanical exfoliation of $Bi_{1.5}Sb_{0.5}Te_{1.7}Se_{1.3}$ (BSTS) from a bulk crystal (from Miracrys) and the flakes were transferred onto the chip. This was done in a glove box with a nitrogen atmosphere in order to prevent oxidation of the interfaces of the van der Waals heterostructures. The sizes of the exfoliated flakes were typically around 7 μm $\times$ 3 μm. The thickness of a typical BSTS flake was later determined to approximately 40 nm through atomic force microscopy (AFM) measurements, which confirms that it is few-layer (one quintuple layer is $\sim$ 1 nm [113]).

A.1.4 Mask design in AutoCAD

Since the exfoliated BSTS flakes were distributed randomly across the chip, the chip had to be manually scanned with light microscopy for flakes which lay across graphene stripes, in order to identify suitable starting points for fabricating the het-

erostructure devices (see example in Figure A.1b). Nonmagnetic and ferromagnetic contacts were designed in AutoCAD and added to the mask that had previously been used for patterning the graphene stripes. A part of the contact mask is shown in Figure A.1c. The nonmagnetic contacts (pink) were connected to the BSTS flakes and as reference contacts to the graphene stripes, while the magnetic contacts (orange) were connected to the graphene stripes. All contacts were designed with individual widths in the range of $0.7 - 3\,\mu$m for the nonmagnetic contacts and $0.2 - 0.7\,\mu$m for the magnetic ones. The reason for this was to give each FM electrode an individual coercivity (see Section 3.2.1). Farther away from the device, all contacts were made wider (around $12\,\mu$m) to increase robustness and make it easier to make connections between the devices and the measurement equipment.

A.1.5 Electron beam lithography, evaporation deposition and lift-off for nonmagnetic contacts

Two layers of resist were spin coated and soft baked in the same way as described in Section A.1.2, whereafter the resist was patterned by electron beam with the design for the nonmagnetic contacts. The exposure was done in two steps. The narrower parts of the contacts were patterned with an electron beam current of 2 nA due to their small size and in order to minimise proximity effects, while the wider contact regions were exposed with an electron beam current of 70 nA in order to speed up the process. Finally, the resist was developed as described in Section A.1.2.

After this, 20 nm of chromium and 90 nm of gold were deposited onto the chips through evaporation deposition with the help of electron beam heating of the target materials in high vacuum ($2-3\cdot10^{-7}$ Torr). The chromium here works as a glue layer in order to increase the adhesion between the silica of the chip and the deposited gold.

Following the deposition, lift-off was performed in order to obtain the desired contacts. First, the edges of the chip were scratched with a scalpel in order to open a path for the solvents to get in under the metal. The chip was then placed in acetone at 65 °C for 10 min followed by IPA at room temperature for 2 min. An example of the nonmagnetic contacts after lift-off is presented in Figure A.1d.

A.1.6 Electron beam lithography, evaporation deposition and lift-off for magnetic contacts

Two layers of resist were spin coated and soft baked in the same way as described in Section A.1.2. After this, the resist was patterned by electron beam with the design for the magnetic contacts in the same way as for the nonmagnetic contacts described in Section A.1.5. Finally, the resist was developed as described in Section A.1.2.

Similarly to in Section A.1.5, electron beam heating of the target material at high vacuum was used for metal evaporation deposition. A layer of 0.1 nm of titanium

was deposited onto the chip and was then oxidised *in situ* for 10 min, after which another 0.1 nm of titanium was deposited and oxidised. The function of the titanium oxide (TiO_2) layer was to work as a tunnel barrier for the electrons, which has the intended effect of increasing the spin injection efficiency by avoiding the conductivity mismatch problem [88]. The deposition chamber was then vacuum pumped overnight after the oxidation process in order to minimise the risk of residual oxygen, since that could easily have oxidised the following cobolt layer. The next morning, 90 nm of cobolt was deposited onto the chip.

It should be noted that the atomic radius of titanium is 145 pm [114], so the deposited titanium layers and the subsequent TiO_2 layer cannot be expected to be homogeneous and there are most likely pinholes through the oxide layer which connect the cobolt directly to the graphene. A single sheet of hexagonal boron nitride (hBN) would have made a better tunnel barrier without any pinholes [64, 107, 115, 116]. However, the aim of this project is not to maximise the signal amplitudes but rather to investigate the material properties of BSTS. Furthermore, using hBN would have necessitated additional fabrication steps. Because of this, the simpler TiO_2 barrier can be considered good enough, and this is why it was chosen.

The lift-off was performed as described in Section A.1.5. An example of a finished device with both nonmagnetic and magnetic contacts is shown in Figures A.1e.

B

MATLAB simulations

In order to better understand the impact of different parameters on the signals from Hanle spin precession measurements, a few simulations of these signals were performed in MATLAB by plotting Equations (3.6) for different parameter values. The obtained results are shown and explained here.

The first set of simulations investigated the effect of varying angles between the polarisation of the injected spin and the magnetisation direction of the detector electrode. By using Equations (3.5) and (3.6), the results in Figure B.1a were obtained. As explained in Section 3.2.3, a parallel alignment gives rise to a symmetric Hanle signal, a perpendicular alignment gives rise to an antisymmetric one and an arbitrary alignment gives rise to a signal with both symmetric and antisymmetric components.

The impacts of the spin lifetime and the spin diffusion coefficient on Equations (3.6) were investigated in the second and third sets of simulations. As seen in Figure B.1b, the signal amplitude increases with the spin lifetime τ_s. This is because a very short spin lifetime will cause most polarised spins to relax before they reach the detector. A longer spin lifetime, however, means that more spins will stay polarised and the spin signal gets a larger amplitude.

Figure B.1c shows that the spin diffusion coefficient D_s greatly affects the shape of the spin signal. This is because the spin diffusion coefficient to some extent can be understood as the speed of the spin diffusion [117]. If D_s is very low, the spins cannot diffuse very far before they relax, and the measured spin signal has a low amplitude (blue curve). A faster diffusion speed allows more polarised spins to reach the detector and the amplitude increases (green and yellow curves). However, if the spins diffuse very quickly, only a short time will pass before they reach the detector, and, even if a strong magnetic field is applied, the spins will not precess much because they are only exposed to the magnetic field for a short time before they are detected. In this way, a larger spin diffusion coefficient decreases the impact of spin precession and the wavy shape of the Hanle spin signal is therefore diminished (orange and red curves). Nevertheless, scattering still causes different spins to have different transit times, which in turn gives rise to dephasing of the polarised spins and a decay of the spin signal for stronger magnetic fields.

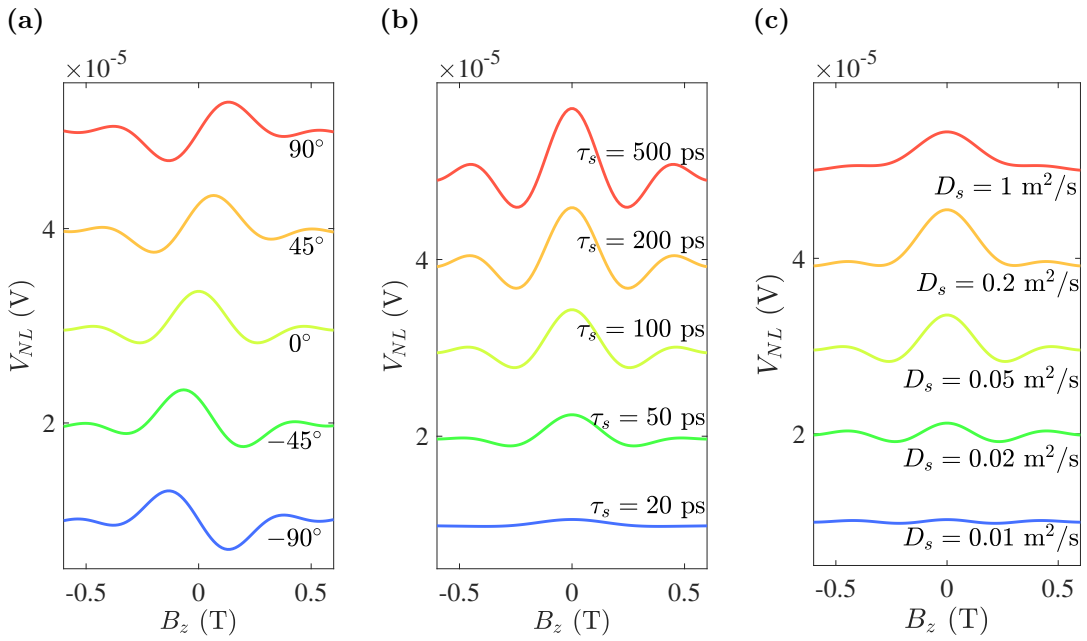

Figure B.1: *Simulated Hanle spin precession signals plotted in MATLAB, based on Equations* (3.6). **(a)** *Hanle signals for different injector-to-detector angles, based on Equations* (3.5) *and* (3.6). **(b)** *Signals for different spin lifetimes and constant spin diffusion coefficient, showing changing signal amplitudes as a result. For simplicity, only the symmetric component (Equation* (3.6a)*) is plotted, but the antisymmetric component (Equation* (3.6b)*) behaves identically.* **(c)** *Signals for different spin diffusion coefficients and constant spin lifetime, resulting in varying ratios between the central peak amplitude and the amplitudes of the non-central peaks. For simplicity, only the symmetric component is plotted, but the antisymmetric component behaves identically.*

C

Supplementary results

Supplementary results to the main part of the thesis are presented in this appendix. The first section contains supplementary results to Chapter 4 and the results from similar experiments in different devices. The second section includes supplementary results to Chapter 5, such as the bias and gate dependencies of the SCC. At the end of the second section, there are also results from investigations of the BSTS flake itself and the graphene/TI interface.

C.1 Supplementary graphene results

The gate dependence of the spin valve measurements across pristine graphene is shown in Figure C.1. These results support the similar behaviour for the Hanle measurements in Figures 4.2c and 4.2d.

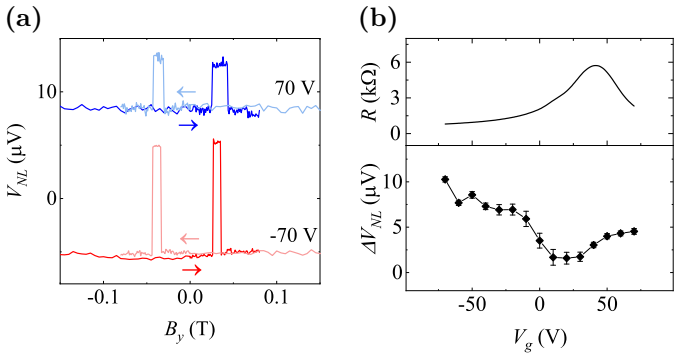

Figure C.1: *Gate voltage dependence of spin valve signals in pristine graphene.* **(a)** *Spin valve non-local signals across pristine graphene for positive and negative gate voltage ($I = \pm 70\,\mathrm{V}$). The measurements were performed for $I = -100\,\mu\mathrm{A}$. The data are shifted vertically for clarity.* **(b)** *Top panel: Local resistance measured when passing a $1\,\mu\mathrm{A}$ current through the pristine graphene channel as a function of gate voltage. Bottom panel: The spin valve signal amplitude for the pristine graphene as a function of gate voltage.*

Figure C.2 shows the results for bias dependent spin transport measurements in a

second device (shown in the optical image in Figure C.2e). This shows reproducibility of the results in Figure 4.1, as the main trends are similar. Two differences are that no sign change is seen neither for the heterostructure nor for the pristine graphene, and that the spin signal is barely observable for the heterostructure graphene at positive bias currents. However, this could be because of the relatively few data points; a sign change might have been visible for the pristine graphene at small positive bias currents, and larger positive bias currents might have resulted in a larger signal amplitude for the heterostructure graphene.

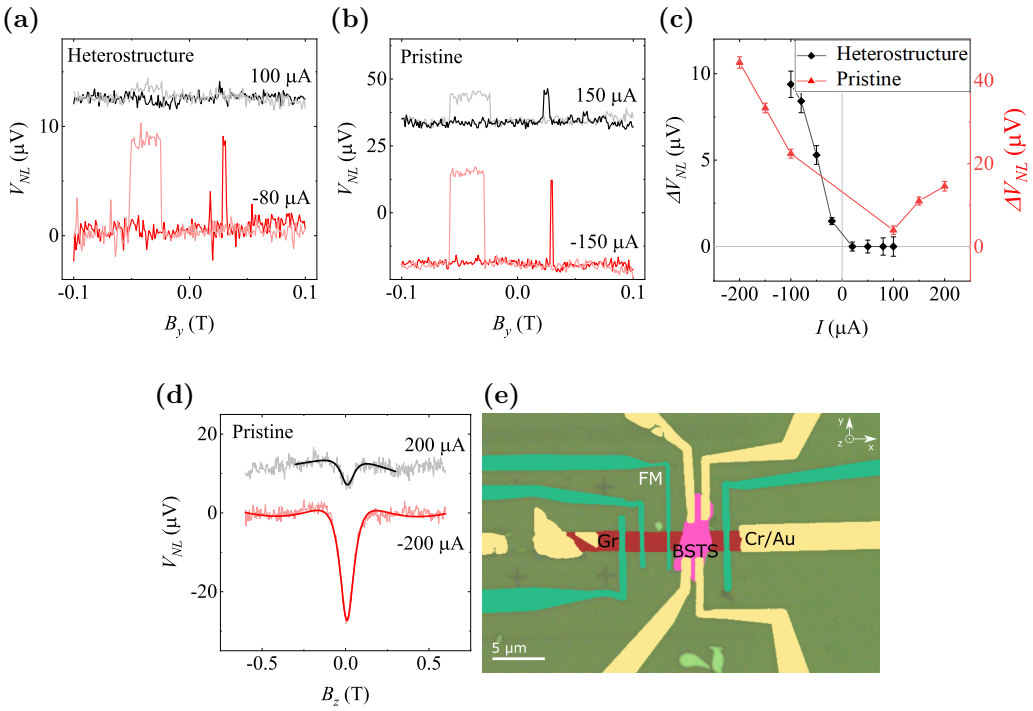

Figure C.2: *Bias current dependence of the spin transport in a second device.* **(a)** *Spin valve non-local signals across the heterostructure for positive ($I = 100\,\mu$A) and negative ($I = -80\,\mu$A) bias currents. The measurements were performed for $V_g = -70$ V. The data are shifted vertically for clarity.* **(b)** *Spin valve non-local signals across pristine graphene for positive and negative bias currents ($I = \pm 150\,\mu$A). The measurements were performed for $V_g = -70$ V. The data are shifted vertically for clarity.* **(c)** *The spin valve signal amplitude for the heterostructure (left y axis) and pristine (right y axis) graphene, respectively, as a function of bias current.* **(d)** *Hanle non-local signals across pristine graphene for positive and negative bias currents ($I = \pm 200\,\mu$A) and corresponding symmetric fits. The measurements were performed for $V_g = -70$ V. Linear backgrounds have been removed and the data are shifted vertically for clarity.* **(e)** *Coloured optical microscope image of the device that was used for the measurements in* (a-d) *and in Figure C.3.*

The gate dependence of the spin transport in the second device is shown in Figure C.3. The obtained results agree very well with those in Figures 4.2 and C.1, and thus show reproducibility. No sign change is observed, and the signal amplitude decreases dramatically around the graphene Dirac point. The spin lifetime and the

spin diffusion length follow this behaviour with smaller parameter values and/or larger error bars when the Hanle signal amplitude is at a minimum.

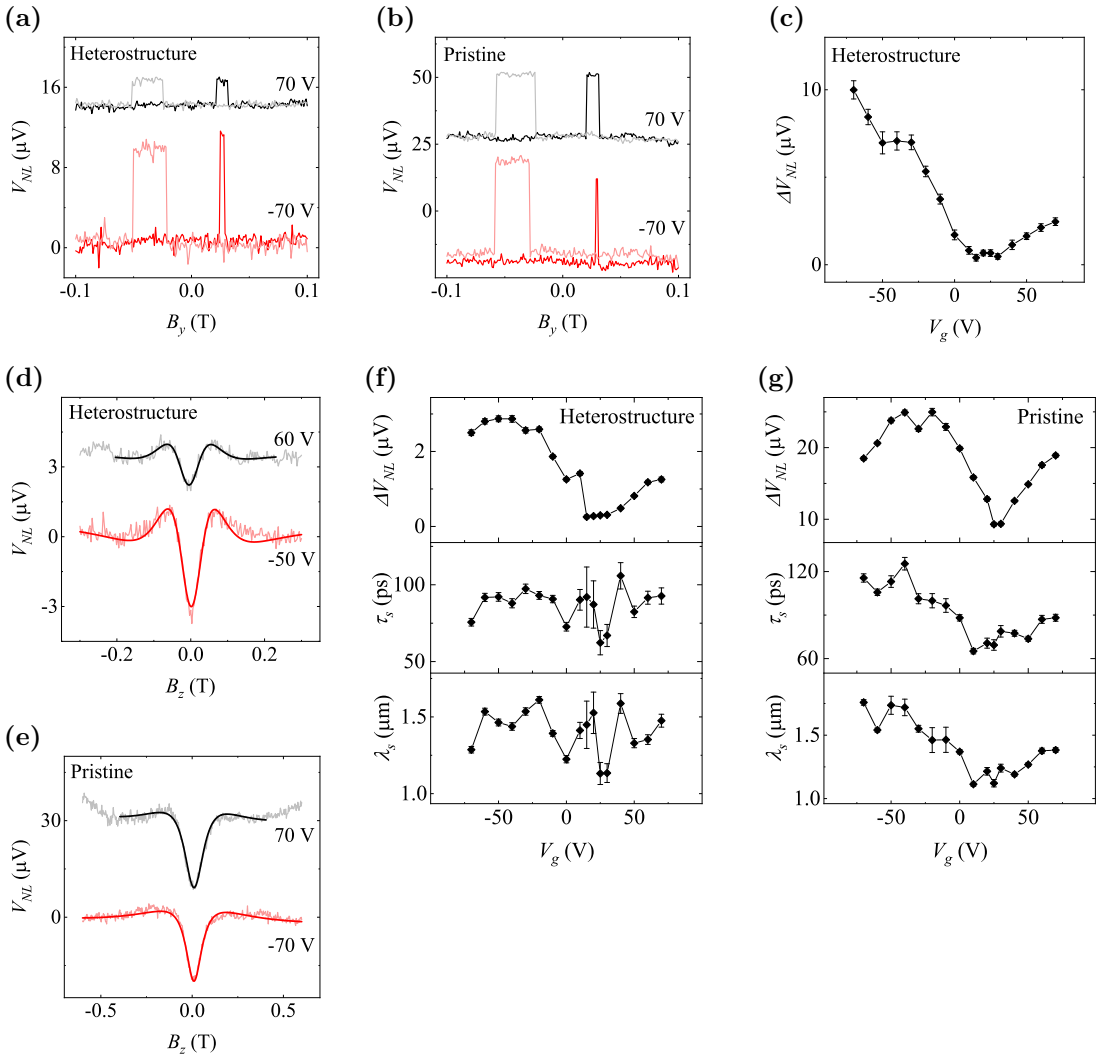

Figure C.3: *Gate voltage dependence of the spin transport in a second device.* **(a)** *Spin valve non-local signals across the heterostructure for positive and negative gate voltages ($V_g = \pm 70\,\mathrm{V}$). The measurements were performed for $I = -100\,\mu\mathrm{A}$. The data are shifted vertically for clarity.* **(b)** *Spin valve non-local signals across pristine graphene for positive and negative gate voltages ($V_g = \pm 70\,\mathrm{V}$). The measurements were performed for $I = -150\,\mu\mathrm{A}$. The data are shifted vertically for clarity.* **(c)** *The spin valve signal amplitude for the heterostructure graphene as a function of gate voltage.* **(d)** *Hanle non-local signals across the heterostructure for positive ($V_g = 60\,\mathrm{V}$) and negative ($V_g = -50\,\mathrm{V}$) gate voltages and corresponding symmetric fits. The measurements were performed for $I = -100\,\mu\mathrm{A}$. Linear backgrounds have been removed and the data are shifted vertically for clarity.* **(e)** *Hanle non-local signals across pristine graphene for positive and negative gate voltages ($V_g = \pm 70\,\mathrm{V}$) and corresponding symmetric fits. The measurements were performed for $I = -200\,\mu\mathrm{A}$. Linear backgrounds have been removed and the data are shifted vertically for clarity.* **(f-g)** *The Hanle signal amplitude as well as spin lifetimes and spin diffusion lengths, extracted from symmetric fits of the Hanle signals, as functions of gate voltage, for the heterostructure and pristine graphene, respectively.*

Figure C.4 shows the results for bias dependent spin transport measurements in a third device (shown in the optical image in Figure C.4a), further showing reproducibility of the results in Figure 4.1. The results in Figures C.4d and C.4e should be especially emphasised, since they have the same bias dependent sign change as the pristine graphene measurements in Figures 4.1e and 4.1f. Since the results in Figure C.4 are for heterostructure graphene, this confirms that there can be a sign change both for heterostructure and for pristine graphene.

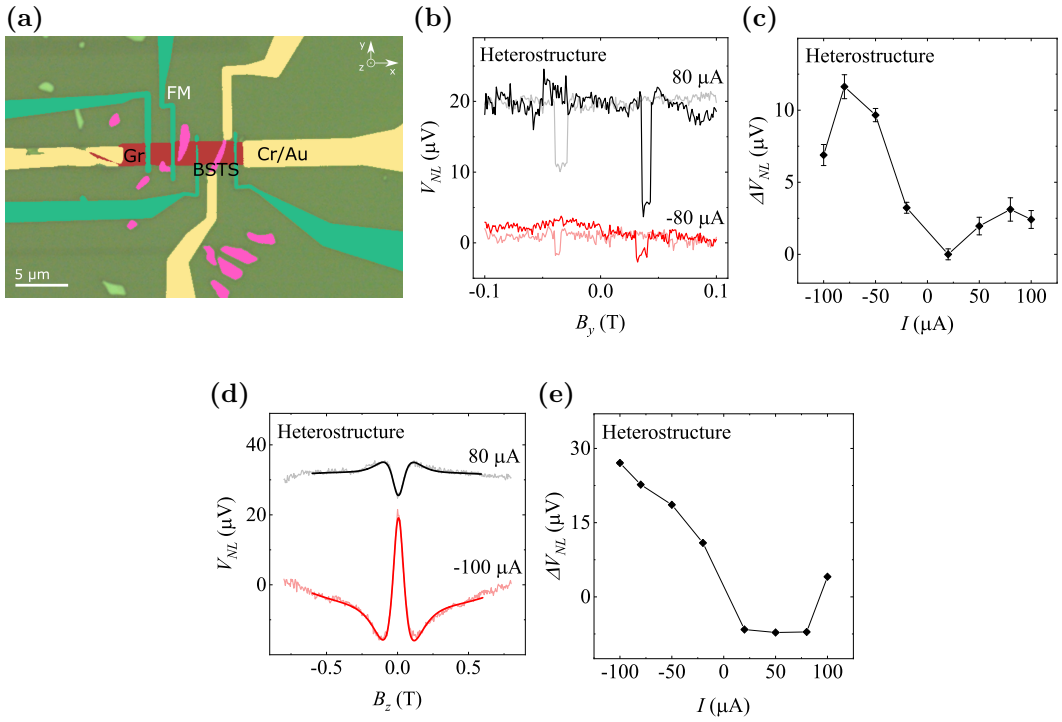

Figure C.4: *Bias current dependence of the spin transport in a third device.* **(a)** *Coloured optical microscope image of the device that was used for the measurements in* (b-e) *and in Figure C.5.* **(b)** *Spin valve non-local signals across the heterostructure for positive and negative bias currents ($I = \pm 80\,\mu$A). The measurements were performed for $V_g = -70$ V. The data are shifted vertically for clarity.* **(c)** *The spin valve signal amplitude for the heterostructure graphene as a function of bias current.* **(d)** *Hanle non-local signals across the heterostructure for positive ($I = 80\,\mu$A) and negative ($I = -100\,\mu$A) bias currents and corresponding symmetric fits. The measurements were performed for $V_g = -70$ V. Linear backgrounds have been removed and the data are shifted vertically for clarity.* **(e)** *The Hanle signal amplitude for the heterostructure graphene as a function of bias current.*

The gate dependence of the spin transport in the third device is shown in Figure C.5, and show further reproducibility of the results in Figures 4.2 and C.1.

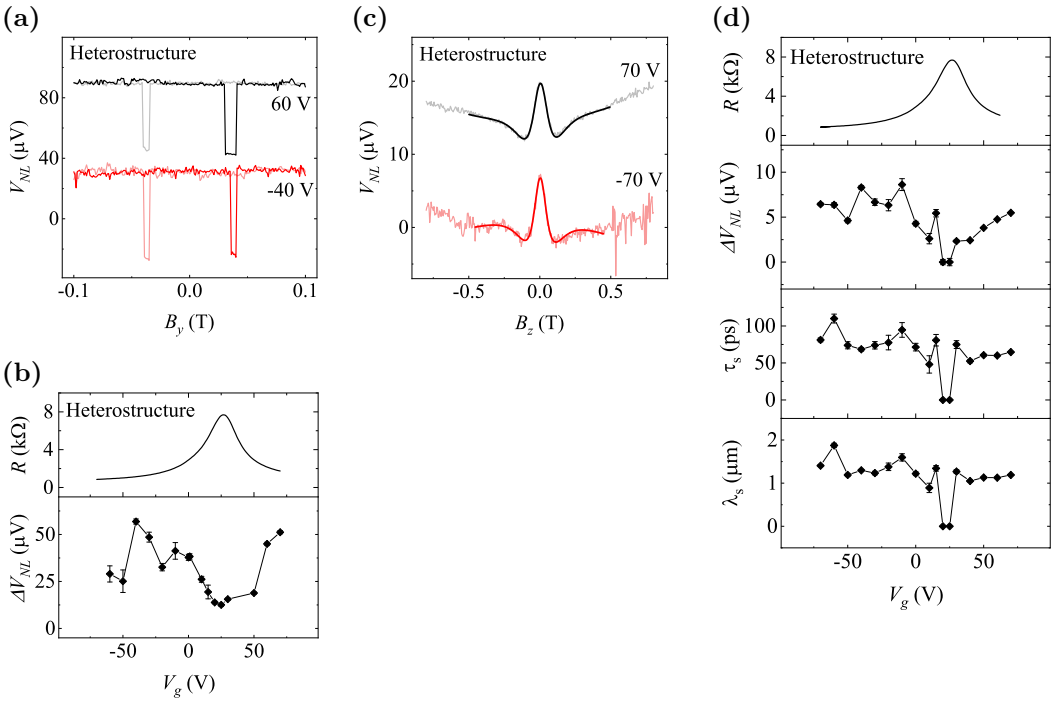

Figure C.5: *Gate voltage dependence of the spin transport in a third device.* **(a)** *Spin valve non-local signals across the heterostructure for positive ($V_g = 60\,\mathrm{V}$) and negative ($V_g = -40\,\mathrm{V}$) gate voltages. The measurements were performed for $I = -100\,\mu\mathrm{A}$. The data are shifted vertically for clarity.* **(b)** *Top panel: Local voltage measured when passing a $1\,\mu\mathrm{A}$ current through the heterostructure as a function of gate voltage. Bottom panel: The spin valve signal amplitude for the heterostructure graphene as a function of gate voltage.* **(c)** *Hanle non-local signals across the heterostructure for positive and negative gate voltages ($V_g = \pm 70\,\mathrm{V}$) and corresponding symmetric fits. The measurements were performed for $I = -100\,\mu\mathrm{A}$. Linear backgrounds have been removed and the data are shifted vertically for clarity.* **(d)** *The Hanle signal amplitude as well as spin lifetimes and spin diffusion lengths, extracted from symmetric fits of the Hanle signals, as functions of gate voltage, for the heterostructure graphene.*

C.2 Supplementary topological insulator results

Figure C.6b shows the symmetric and antisymmetric components of a Hanle signal from measurement geometry 2 in Figure C.6a, which corresponds to Figure 5.2a for measurement geometry 1. Since the device broke before a full set of measurements could be performed, Figure C.6b is based on a single Hanle measurement. Calculations with Equation (3.5) gave an angle of $\varphi = 48 \pm 3°$ between the spin polarisation and the magnetisation direction of the detector contact, which is at least somewhat close to the results for geometry 1.

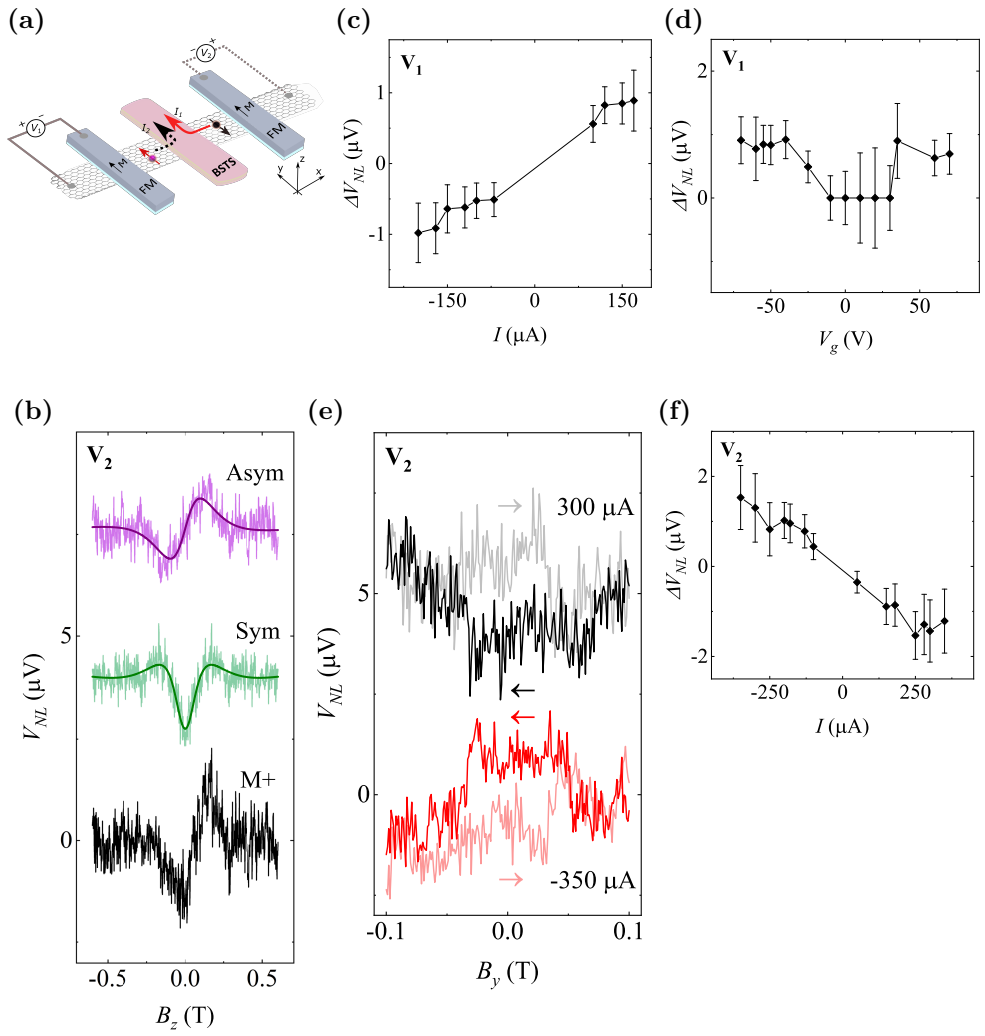

Figure C.6: *Supplementary results from the CSC experiments.* **(a)** *Schematic of the device and the two different measurement geometries that were used for the CSC experiments, applying charge currents along positive and negative x components, respectively.* **(b)** *Hanle spin precession non-local signals for measurement geometry 2 in* (a) *with FM contact magnetisation along the $+y$ direction (black curve) as well as the symmetric (light green curve) and the antisymmetric (violet curve) components of the measured signal. The dark green and purple curves are fits of the respective signals. The measurements were performed for $I = -350\,\mu$A and $V_g = -70\,$V. A linear background has been subtracted and the data are shifted vertically for clarity.* **(c)** *The amplitude of measured spin switch signals for measurement geometry 1 as a function of bias current. The measurements were performed for $V_g = -60\,$V.* **(d)** *The amplitude of measured spin switch signals for measurement geometry 1 as a function of gate voltage. The measurements were performed for $I = 150\,\mu$A.* **(e)** *Spin switch non-local signals for measurement geometry 2, for positive ($I = 300\,\mu$A) and negative ($I = -350\,\mu$A) bias currents. The measurements were performed for $V_g = -75\,$V. The data are shifted vertically for clarity.* **(f)** *The amplitude of the measured spin switch signals for measurement geometry 2 as a function of bias current.*

Figures C.6c and C.6d show the bias and gate dependencies, respectively, of the obtained spin switch signals for geometry 1. This supports the results in Figures 5.3d and 5.4c. The similar bias dependence (although with a sign change) for geometry 2 in Figures C.6e and C.6f further supports Figure 5.3d.

The bias dependence of the SCC spin signals is shown in Figure C.7. Contrary to the CSC case (see Figure 5.3), there is no sign change of the signals for opposite bias current, and the bias dependence is V-shaped rather than linear. However, this behaviour does not come from the SCC, but rather from the graphene/FM contact interface at the spin injection, as explained in Section 5.2.

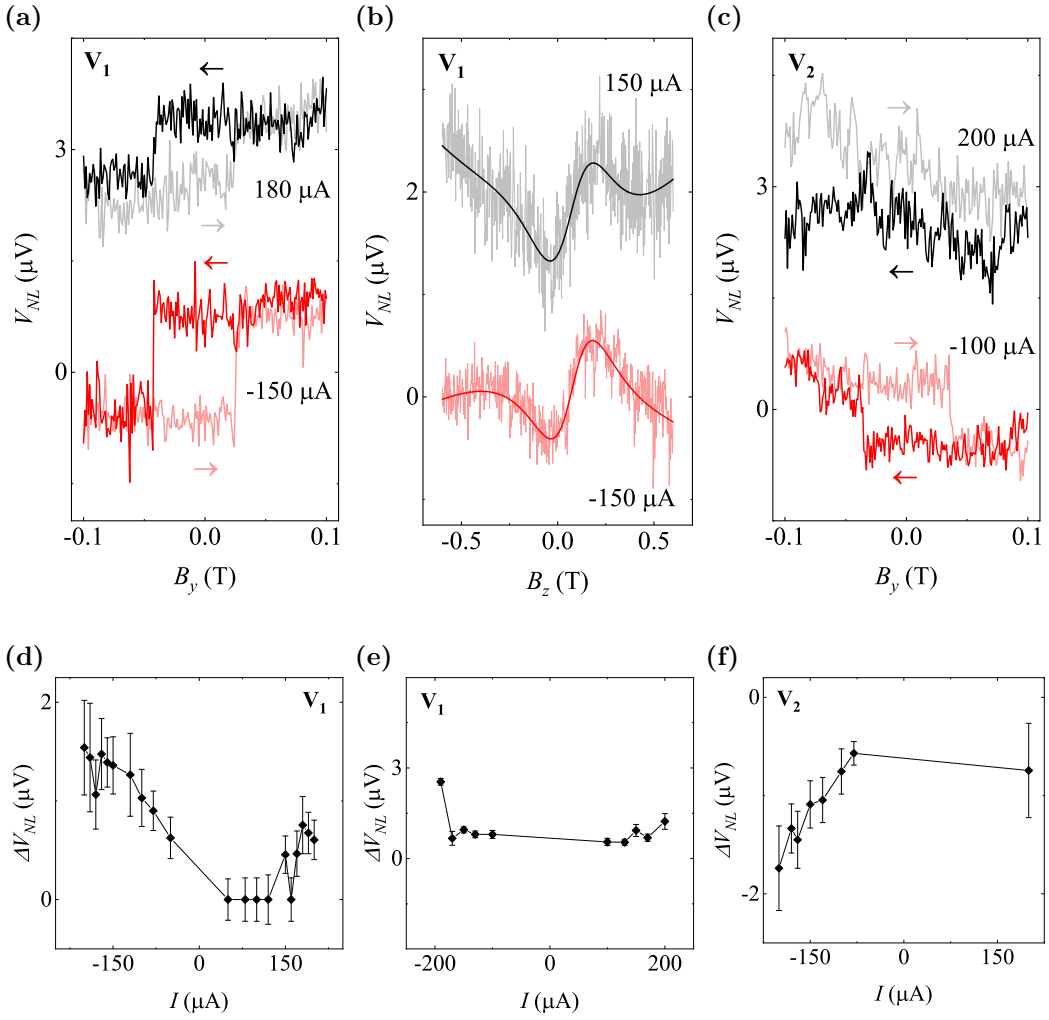

Figure C.7: *Bias current dependence of the SCC signal.* **(a)** *Spin switch non-local signals for positive ($I = 180\,\mu$A) and negative ($I = -150\,\mu$A) bias currents in measurement geometry 1. The measurements were performed for $V_g = -70$ V. The data are shifted vertically for clarity.* **(b)** *Hanle non-local signals for positive and negative bias currents ($I = \pm 150\,\mu$A) in measurement geometry 1 and corresponding antisymmetric fits. The measurements were performed for $V_g = -75$ V. Linear backgrounds have been removed and the data are shifted vertically for clarity.* **(c)** *Spin switch non-local signals for positive ($I = 200\,\mu$A) and negative ($I = -100\,\mu$A) bias currents in measurement geometry 2. The measurements were performed for $V_g = -75$ V. The data are shifted vertically for clarity.* **(d-f)** *The amplitudes of the measured signals in* (a-c) *as functions of bias current.*

A comparison of Figures C.7a and C.7d *versus* Figures C.7c and C.7f shows a signal sign change between the two measurement geometries in Figure 5.5a. This supports the results in Figures 5.5c and 5.5d, and confirms that the SCC is odd with the x component of the injected spin current, analogously to what is shown for the CSC in Figure 5.2.

Figure C.8 presents the gate voltage modulation of the SCC. Similarly to the case

for CSC (see Figure 5.4), there is no sign change of the spin signal when the Fermi level is tuned across the graphene Dirac point. The signal also disappears around the Dirac point of the graphene channel, which is in agreement with the CSC results.

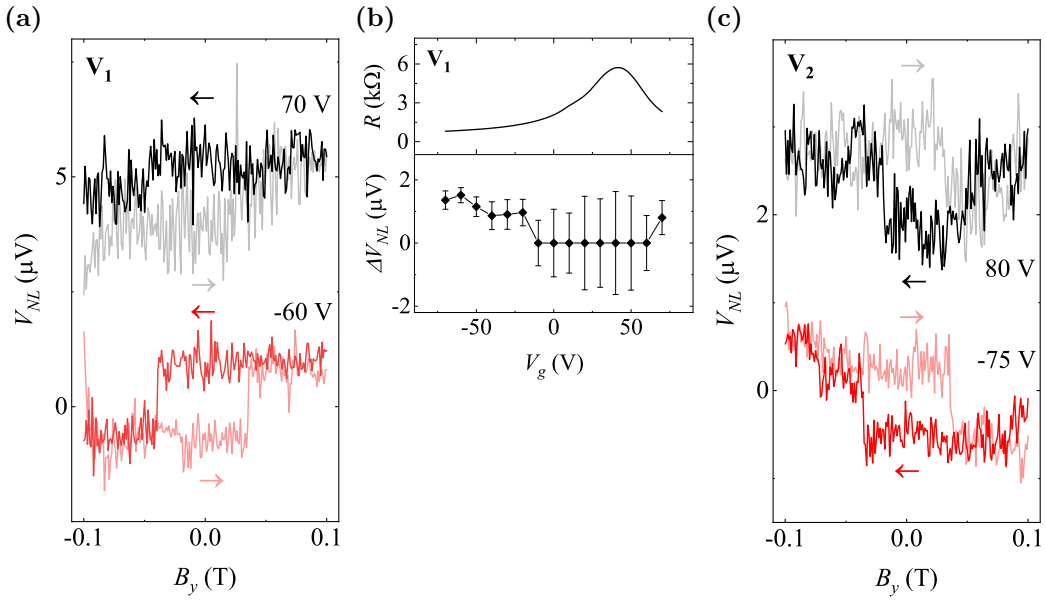

Figure C.8: *Gate voltage dependence of the SCC signal.* **(a)** *Spin switch non-local signals for positive ($V_g = 70\,\mathrm{V}$) and negative ($V_g = -60\,\mathrm{V}$) gate voltages in measurement geometry 1. The measurements were performed for $I = -150\,\mu\mathrm{A}$. The data are shifted vertically for clarity.* **(b)** *Top panel: Local voltage measured when passing a $1\,\mu\mathrm{A}$ current through the graphene channel across the vdW heterostructure as a function of gate voltage. The voltage maximum at $V_g = 45\,\mathrm{V}$ corresponds to the graphene Dirac point. Bottom panel: The amplitude of the measured spin switch signals as a function of gate voltage.* **(c)** *Spin switch non-local signals for positive ($V_g = 80\,\mathrm{V}$) and negative ($V_g = -75\,\mathrm{V}$) gate voltages in measurement geometry 2. The measurements were performed for $I = -100\,\mu\mathrm{A}$. The data are shifted vertically for clarity.*

The sign difference between Figures C.8a and C.8c gives further support to the claim that the SCC signal is odd with the x component of the injected spin current.

The TI and the graphene/TI interface were investigated further in a separate device, shown in Figure C.9a. The current-voltage characteristics of the interface and the interface resistance were measured, using the measurement setup in Figure C.9a. The results are shown in Figures C.9b and C.9c, respectively. The obtained interface resistance is $R \approx 33\,\mathrm{k}\Omega$ with only a small deviance for bias and gate modulations.

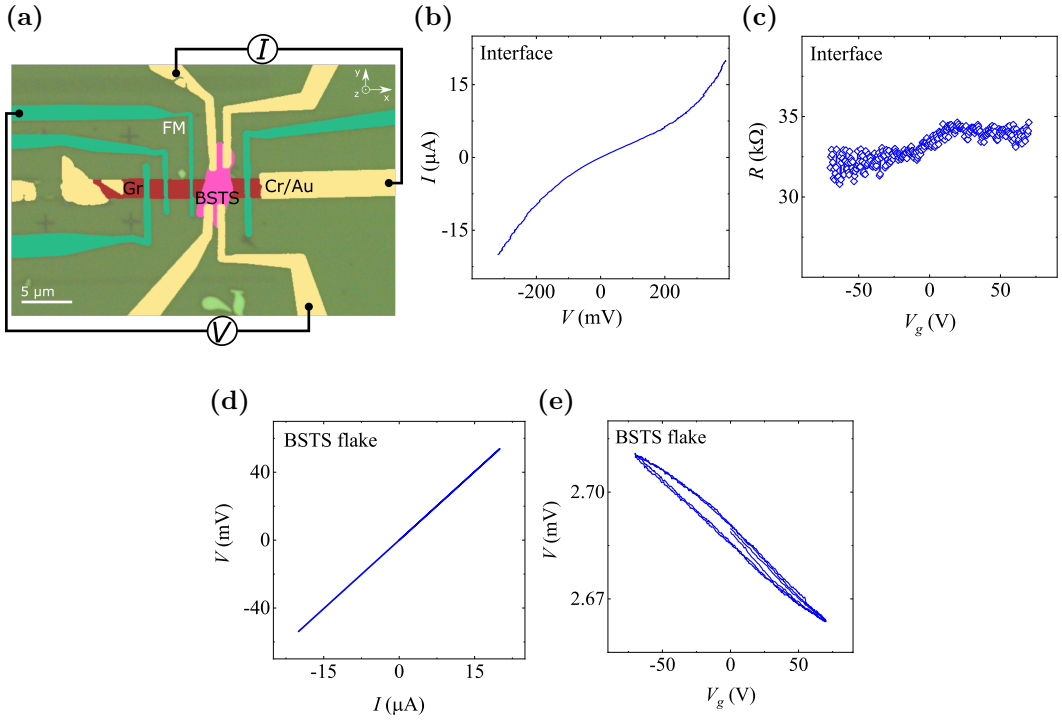

Figure C.9: *Local measurements of a TI flake.* **(a)** *Coloured optical microscope image of the device that was used for the measurements in* (b-e) *with drawn schematics showing the measurement setup of* (b-c). **(b)** *Current-voltage characteristics for passing a current across the graphene/TI interface for zero applied gate voltage.* **(c)** *Interface resistance measured when passing a* $1\,\mu$A *current across the graphene/TI interface and detecting the voltage across said interface, as a function of gate voltage.* **(d)** *Local voltage measured when passing a current through a TI flake for zero applied gate voltage as a function of bias current.* **(e)** *Local voltage measured when passing a* $1\,\mu$A *current through a TI flake as a function of gate voltage. Note that these measurements were performed for a different device than the CSC and SCC experiments.*

Local voltage measurements with an applied current across the TI flake give the result in Figure C.9d. The linear behaviour means that the local resistance of $R = 2.7\,\text{k}\Omega$ is constant with bias current, which is anticipated.

Figure C.9e shows the gate voltage modulation of the local voltage. The increasing local voltage (corresponding to an increasing local resistance) for negative gate voltages indicate that the measurements were performed to the right of the TI Dirac point, meaning that the TI flake is electron doped. Similar measurements in literature with a larger range of gate voltages have successfully shown this [31].

Finally, it should be mentioned that both the bias and the gate modulation experiments with the BSTS flake were performed also with applied out-of-plane magnetic fields ($B_z = \pm 800\,\text{mT}$). However, no change in either of the modulations were observed, indicating that the charge transport in the TI is independent of out-of-plane external magnetic fields.

DEPARTMENT OF MICROTECHNOLOGY AND NANOSCIENCE
CHALMERS UNIVERSITY OF TECHNOLOGY
Gothenburg, Sweden
www.chalmers.se

CHALMERS
UNIVERSITY OF TECHNOLOGY